REPORT NO.
UCB/SEMM-88/02

STRUCTURAL ENGINEERING
MECHANICS AND MATERIALS

A PERTURBATION METHOD FOR DYNAMIC ANALYSIS OF UNDER-INTEGRATED SHELL ELEMENTS

BY

LOC VU-QUOC

(Submitted to *Computer Methods in Applied Mechanics and Engineering*.)

APRIL 1988

DEPARTMENT OF CIVIL ENGINEERING
UNIVERSITY OF CALIFORNIA
BERKELEY, CALIFORNIA

A Perturbation Method for Dynamic Analysis of Under-Integrated Shell Elements

By

L. Vu-Quoc†

Abstract

An efficient perturbation method that allows reliable and accurate dynamic analyses of general shell structures using under-integrated elements is proposed. Both the perturbation of the stiffness matrix and the projection of the mass matrix are performed directly in the global coordinate system (thus avoiding local-global transformations of element matrices), and only once for each element instead of at each integration point. The method does not require any factor to be fully integrated over the element. Due to the consistency of the perturbed stiffness, the 9-node element passes several patch tests, including higher order ones. Further, algebraic expression for the projection operator of the mass matrix is derived, and contributes significantly to the efficiency of the methodology. Several examples are presented to assess the effectiveness of the proposed method in filtering all spurious modes from the eigen-spectrum, and the accuracy of the resulting eigen-frequencies of the genuine mode shapes.

Table of Contents

† Mailing address: c/o Prof. R.L. Taylor, Structural Engineering, Mechanics, and Materials, University of California, Berkeley, CA 94720.

A Perturbation Method for Dynamic Analysis of Under-Integrated Shell Elements

By

L. Vu-Quoc

1. Introduction

We present a methodology based on a perturbation approach to extend the capability of under-integrated shell elements, which are plagued by the existence of undesirable spurious modes polluting the response, to allow efficient, reliable, and accurate dynamic analyses of general shell structures.

The advantages of evaluating the stiffness matrix of shell elements using selective/reduced-integration (Pawsey & Clough [1971], and Zienkiewicz, Taylor & Too [1971]) versus full-integration are manyfold: Not only that the membrane/shear locking problem as the element thickness decreases is resolved, the computational effort is on the other hand considerably reduced by the same factor. This reduction becomes even more significant in nonlinear analysis as well noted by Flanagan & Belytschko [1981]. A mathematical framework for the selective/reduced-integration approach is provided in the classical paper by Malkus & Hughes [1978]. For 9-node shell elements, an analysis of the above welcomed effects of reduced-integration is given by Parisch [1979]. The disadvantage of using reduced-integration is, however, rooted in the existence of spurious zero-energy modes, which is due to the rank deficiency of under-integrated stiffness matrices. In static analyses, Kosloff & Frazier [1978] pioneered a perturbation method by adding an artificially small energy to these spurious modes, which are therefore filtered from the response. This method has been applied to shell elements by many authors. In the dynamic case, Belytschko, Tsay & Liu [1982] proposed to increase the artificial energy that is injected into the spurious modes to push them into the higher frequency range.

The main goal of the present paper is to present a methodology that allows a complete filtering of the undesirable spurious dynamics for a class of under-integrated shell elements formulated in Vu-Quoc & Mora [1987]. Emphasis will be focused on the more difficult case of the 9-node bi-quadratic shell element, as compared with the more straightforward case of the 4-node bilinear shell element (which needs not be flat). A careful analysis of spurious zero-energy modes of a large class of under-integrated 9-node shell elements is performed. We give exact expressions of spurious modes as functions of the Jacobian of element isoparametric mapping in these cases. Understanding how these modes change with element shapes and distortion is essential for constructing a simple, efficient, and reliable filtering method.

The proposed perturbation method for dynamic analysis is a two-stage strategy that consists of (i) a perturbation of the under-integrated stiffness to fully compensate its rank, and (ii) a projection of the mass matrix either to nullify the generalized mass of some spurious modes, or to render impossible for other spurious modes to become eigenvectors of the perturbed eigenvalue problem. That both stages (i) and (ii) are carried out directly in the global coordinate system, thus avoiding the costly local-global transformation of element matrices, is an important feature of the proposed approach, for therein lies the efficiency of the method.

The perturbation of the stiffness in stage (i) is constructed to be orthogonal to a displacement field that is linear in the coordinates for a 4-node shell element, or for a general curved 9-node shell element, and quadratic in the coordinates for a flat 9-node element. In Vu-Quoc & Mora [1987], we have established the better performance of a consistent perturbed stiffness over an inconsistent one. Due to this consistency, the present 9-node shell element passes several patch tests, including the higher order tests where displacement field involves quadratic polynomials in the coordinates. These patch tests, proposed in Huang & hinton [1986], include several states of stress imposed on a square patch of elements: stretching, (in and out-of-plane) shearing, pure bending,

(Reissner-Mindlin and Kirchhoff-Love) twisting.

As mentioned earlier, one approach to remove spurious modes from the low frequency range is to increase the perturbation factor of the stiffness matrix, thus pushing the spurious modes to higher frequencies as proposed by Belytschko, Tsay & Liu [1982].† However, only increasing the generalized stiffness (or the perturbation energy) of the spurious modes is not a reliable method, since these spurious modes are merely shifted out of the bandwidth of the low frequencies into the higher ones. Moreover, there is a limit to how far one can increase the perturbation factor and yet still maintain the structure flexibility acquired through reduced integration for small thickness. The consequent persisting presence of spurious modes must therefore be accounted for when using step-by-step integration of the equations of motion.

We examine the dynamic analysis using the proposed perturbed system by considering the equivalence between step-by-step integration of the complete system of equations of motion and integration of the scalar modal equations, which then leads to methods for constructing the desired damping matrix and mass matrix to filter all spurious dynamics from the response. We propose an efficient and reliable projection operator for the mass matrix, where similar to the perturbation of the stiffness matrix the projection is performed directly in the global coordinate system, thus avoiding all local-global transformation. Furthermore, the proposed projection method conserves the total element mass under rigid body motions.

Several examples of shell structures are presented to demonstrate the appearance of spurious modes in the low-frequency range when using the unperturbed system, and the effects of mesh refinement on the eigen-frequencies of spurious modes. Also to be demonstrated through these examples are the effectiveness, efficiency, and accuracy of the proposed perturbation approach in filtering undesirable spurious modes from the eigen-

† A spurious mode may, or may not, appear depending on the finite element mesh and boundary conditions.

spectrum. The results obtained also point to the superior performance of the perturbed system with the present projected mass matrix in yielding better eigen-frequencies than systems with various types of mass matrix.

2. Formulation of shell element

In this section, we summarize briefly the formulation of a class of degenerated shell elements discussed in Vu-Quoc & Mora [1987]. In particular, the expressions of the strain-displacement relations are recalled here for later work on spurious zero-energy modes. Emphasis is, however, to set the stage for introducing the inertia operator, and for developing the methodology for transient dynamic analysis using under-integrated shell elements.

2.1. Geometry and stiffness operator. Let $(\theta^{\{i\}}) \equiv (\theta^1, \theta^2, \theta^3)$ denote the convected curvilinear coordinates inscribed on the shell body $\Omega \subset \mathbb{R}^3$, such that $(\theta^{\{\alpha\}}) \equiv (\theta^1, \theta^2)$ coordinatize the shell mid-surface, and θ^3 the transverse fiber.† The tangent vectors to these coordinate lines are denoted by $\{\mathbf{A}_1, \mathbf{A}_2, \mathbf{A}_3\}$, whose components with respect to the orthonormal basis $\{\mathbf{E}_1, \mathbf{E}_2, \mathbf{E}_3\}$ of the ambient space $\mathbb{R}^3$ are written as A_i^I; that is, $\mathbf{A}_i = A_i^I \mathbf{E}_I$.‡ The deformed configuration in the ambient space is defined by the basis $\{\mathbf{e}_1, \mathbf{e}_2, \mathbf{e}_3\}$, chosen such that $\mathbf{e}_i \equiv \mathbf{E}_i$, $i = 1,2,3$, for convenience. A continuous field of orthonormal vectors $\{\mathbf{T}_1, \mathbf{T}_2, \mathbf{T}_3\}$, with $\mathbf{T}_i = T_i^j \mathbf{e}_j$ and with $\mathbf{T}_3$ lying along the transverse fiber, is assumed to cover the shell mid-surface.

The displacement vector $\mathbf{u}^*$ of a point $(\theta^{\{i\}})$ is given by

$$\mathbf{u}^*(\theta^{\{i\}}) := \mathbf{u} + \frac{\theta^3 h}{2} \boldsymbol{\chi} \times \mathbf{T}_3 = \left[u^i + \frac{\theta^3 h}{2} (\chi^2 T_1^i - \chi^1 T_2^i) \right] \mathbf{e}_i \,, \tag{2.1}$$

where $\mathbf{u}(\theta^{\{\alpha\}}) = u^i(\theta^{\{\alpha\}}) \mathbf{e}_i$ is the displacement of the point $(\theta^{\{\alpha\}},0)$ in the mid-surface,

† Roman indices take values in {1,2,3}, whereas Greek indices take values in {1,2}.
‡ Summation convention is implied on repeated indices.

$h(\theta^{\{\alpha\}})$ the thickness, and $\boldsymbol{\chi}(\theta^{\{\alpha\}}) = \chi^{\beta}(\theta^{\{\alpha\}})\mathbf{T}_{\beta}(\theta^{\{\alpha\}})$ the (infinitesimal) rotation vector of the transverse fiber $\mathbf{T}_3(\theta^{\{\alpha\}})$.

Let $\{P_{\mathrm{I}}(\theta^{\{\alpha\}});\, \mathrm{I} = 1,...,N^e\}$ be a family of interpolatory functions on a shell element with N^e nodes and whose domain is denoted by Ω^e. For each element, the values of $(\theta^{\{i\}})$ are restricted to the bi-unit cube $([-1, 1])^3$. The element stiffness matrix $\mathbf{K}^e$ is evaluated by

$$\mathbf{K}^e = \int_{\Omega^e} \mathbf{B}^{\mathrm{T}}\, [C^{ijkl}]\, \mathbf{B}\, \mathrm{d}\Omega \in \mathbb{R}^{n^e \times n^e}\,, \tag{2.2}$$

with $n^e := 5N^e$ being the number of dof's per element, $\mathbf{B} \in \mathbb{R}^{5\times n^e}$ the strain-displacement matrix, and $[C^{ijkl}] \in \mathbb{R}^{5\times 5}$ the matrix of plane-stress elastic moduli. The basic ordering of the n^e dof's of an element throughout the paper is assumed to be $\{u_1^{\{i\}}, \chi_1^{\{\alpha\}} \mid \cdots \mid u_{N^e}^{\{i\}}, \chi_{N^e}^{\{\alpha\}}\}$.† The strain tensor within the element is denoted by $\boldsymbol{\Gamma} = \Gamma_{pq}\mathbf{A}^p \otimes \mathbf{A}^q$, where $\{\mathbf{A}^1, \mathbf{A}^2, \mathbf{A}^3\}$ are cotangent vectors conjugate with $\{\mathbf{A}_1, \mathbf{A}_2, \mathbf{A}_3\}$ — see Vu-Quoc & Mora [1987] for the details. It proved convenient to split the strain-displacement matrix $\mathbf{B}$ into sub-matrices which correspond to the translational dof's u^i denoted by $\mathbf{B}^i_{dis}$, and those sub-matrices corresponding to the rotation dof's χ^α, denoted by $\mathbf{B}^\alpha_{rot}$. Detailed expressions of these sub-matrices, corresponding to the five strain components $\{\Gamma_{11}, \Gamma_{22}, 2\Gamma_{23}, 2\Gamma_{31}, 2\Gamma_{12}\}$, are given below

† Throughout this paper, a matrix is defined by its representative coefficient (enclosed in brackets), whose dummy indices are to be expanded, with Roman indices taking values in {1,2,3} and Greek indices in {1,2}. This expansion does not apply to those indices enclosed in parentheses.

$$\mathbf{B}^{1}_{dis} = \begin{bmatrix} A^{1}_{1}\left\{P_{1,1}\,,\,\cdots\,,\,P_{N,1}\right\} \\ A^{1}_{2}\left\{P_{1,2}\,,\,\cdots\,,\,P_{N,2}\right\} \\ A^{1}_{3}\left\{P_{1,2}\,,\,\cdots\,,\,P_{N,2}\right\} \\ A^{1}_{3}\left\{P_{1,1}\,,\,\cdots\,,\,P_{N,1}\right\} \\ \left(A^{1}_{1}P_{1,2}+\;A^{1}_{2}P_{1,1}\right),\,\cdots\,,\,\left(A^{1}_{1}P_{N,2}+\;A^{1}_{2}P_{N,1}\right) \end{bmatrix} \in \mathbb{R}^{5\times N^e}\,, \tag{2.3a}$$

$$\mathbf{B}^{\alpha}_{rot} = \frac{1}{2}\,e_{\alpha\beta}\begin{bmatrix} \theta^3\mathbf{A}_1\bullet\left\{h_1P_{1,1}\mathbf{T}_{\beta 1}\,,\,\cdots\,,\,h_NP_{N,1}\mathbf{T}_{\beta N}\right\} \\ \theta^3\mathbf{A}_2\bullet\left\{h_1P_{1,2}\mathbf{T}_{\beta 1}\,,\,\cdots\,,\,h_NP_{N,2}\mathbf{T}_{\beta N}\right\} \\ h_1(P_{1,2}\theta^3\mathbf{A}_3+\;P_1\mathbf{A}_2)\bullet\mathbf{T}_{\beta 1}\,,\,\cdots\,,\,h_N(P_{N,2}\theta^3\mathbf{A}_3+\;P_N\mathbf{A}_2)\bullet\mathbf{T}_{\beta N} \\ h_1(P_{1,1}\theta^3\mathbf{A}_3+\;P_1\mathbf{A}_1)\bullet\mathbf{T}_{\beta 1}\,,\,\cdots\,,\,h_N(P_{N,1}\theta^3\mathbf{A}_3+\;P_N\mathbf{A}_1)\bullet\mathbf{T}_{\beta N} \\ h_1\theta^3(P_{1,1}\mathbf{A}_2+\;P_{1,2}\mathbf{A}_1)\bullet\mathbf{T}_{\beta 1}\,,\,\cdots\,,\,h_N\theta^3(P_{N,1}\mathbf{A}_2+\;P_{N,2}\mathbf{A}_1)\bullet\mathbf{T}_{\beta N} \end{bmatrix} \in \mathbb{R}^{5\times N^e}\,, \tag{2.3b}$$

where $P_{\mathrm{I},\alpha} \equiv \partial P_{\mathrm{I}}/\partial\theta^{\alpha}$, and $e_{\alpha\beta}$ is the permutation symbol defined such that $e_{11} = e_{22} = 0$ and $e_{12} = -e_{21} = 1$. The values of h and $\mathbf{T}_{\beta}$ at a node I with coordinates $(\theta^1_{\mathrm{I}},\,\theta^2_{\mathrm{I}})$ are denoted by h_{I} and $\mathbf{T}_{\beta\mathrm{I}}$, for $\mathrm{I} = 1,\ldots,N^e$. Coordinates of the nodal points and the corresponding interpolatory functions for a 4-node ($N^e = 4$) bi-linear element are given by

$$\begin{aligned} \{\,(\theta^1_{\mathrm{I}},\,\theta^2_{\mathrm{I}})\,\} &:= \{\,(\theta^1_1,\,\theta^2_1),\,\ldots\,,(\theta^1_4,\,\theta^2_4)\,\} = \{\,(-1,\,-1),\,(1,\,-1),\,(1,\,1),\,(-1,\,1)\,\}\,, \\ P_{\mathrm{I}}(\theta^{\{\alpha\}}) &:= \frac{1}{4}[1+\;\theta^1_{(\mathrm{I})}\theta^1][1+\;\theta^2_{(\mathrm{I})}\theta^2]\,,\quad \text{for I} = 1,2,3,4\,, \end{aligned} \tag{2.4a}$$

and for the 9-node ($N^e = 9$) Lagrangian element by:

$$\{\ (\theta_{\rm I}^1,\ \theta_{\rm I}^2)\ \} := \{\ (-1,\ -1),\ (1,\ -1),\ (1,\ 1),\ (-1,\ 1),\ (0,\ -1),\ (1,\ 0),\ (0,\ 1),\ (-1,\ 0),\ (0,\ 0)\ \}\ ,$$

$$P_{\rm I}(\theta^{\{\alpha\}}) := \frac{\theta^1(\theta^1-\theta_{\rm I}^1)}{2}\frac{\theta^2(\theta^2-\theta_{\rm I}^2)}{2}\ ,\quad \text{for I} = 1,2,3,4\ ,$$

$$P_{\rm I}(\theta^{\{\alpha\}}) := [1-(\theta^1)^2]\frac{\theta^2(\theta^2-\theta_{\rm I}^2)}{2}\ ,\quad \text{for I} = 5,7\ , \tag{2.4b}$$

$$P_{\rm I}(\theta^{\{\alpha\}}) := \frac{\theta^1(\theta^1-\theta_{\rm I}^1)}{2}[1-(\theta^2)^2]\ ,\quad \text{for I} = 6,8\ ,$$

$$P_9(\theta^{\{\alpha\}}) := [1-(\theta^1)^2][1-(\theta^2)^2]\ .$$

The tangent vectors $\{\mathbf{A}_i\}$ to the coordinate lines $\theta^{\{i\}}$ are computed from the nodal position vectors $\mathbf{X}_{\rm I} = X_{\rm I}^i\mathbf{E}_i$ as follows

$$\mathbf{A}_\alpha = \sum_{\rm I=1}^{N^e} P_{{\rm I},\alpha}\left[\mathbf{X}_{\rm I} + \frac{\theta^3 h_{\rm I}}{2}\mathbf{T}_{3{\rm I}}\right],\quad \mathbf{A}_3 = \frac{1}{2}\sum_{\rm I=1}^{N^e} P_{\rm I} h_{\rm I}\mathbf{T}_{3{\rm I}}\ . \tag{2.5}$$

It is useful to recall briefly the structure of the element stiffness matrix $\mathbf{K}^e$ in (2.2) in terms of the strain-displacement matrices $\mathbf{B}_{die}^i$ and $\mathbf{B}_{rot}^\alpha$, as an assemblage of submatrices of size $N^e \times N^e$:

$$\mathbf{K}^e = \int_{\Omega^e} \underset{\substack{i,j\ \in\ \{1,2,3\}\\ \alpha,\beta\ \in\ \{1,2\}}}{A} \Big[\ \Big(\mathbf{B}_{die}^i\Big)^{\rm T}[C^{pqrs}]\mathbf{B}_{die}^j \oplus \Big(\mathbf{B}_{rot}^\alpha\Big)^{\rm T}[C^{pqrs}]\mathbf{B}_{rot}^\beta$$

$$\oplus \Big(\mathbf{B}_{die}^i\Big)^{\rm T}[C^{pqrs}]\mathbf{B}_{rot}^\beta \oplus \Big(\mathbf{B}_{rot}^\alpha\Big)^{\rm T}[C^{pqrs}]\mathbf{B}_{die}^j\ \Big]\,{\rm d}\Omega\ , \tag{2.6}$$

where the symbols A and $\oplus$ are used to designate the assembling operation.

To remove shear and membrane locking in thin shells, the element stiffness in (2.6) is numerically evaluated using uniformly reduced integration. The coordinates of the reduced-integration points are $(\theta^1,\ \theta^2) = (0,\ 0)$ for the 4-node element, and $(\theta^1,\ \theta^2) = (\pm\frac{1}{\sqrt{3}},\ \pm\frac{1}{\sqrt{3}})$ for the 9-node element. It was observed through numerical experiments in Belytschko and co-workers [1984,1985], and shown analytically in Vu-Quoc & Mora [1987] that the displacement mode $\{u_{\rm I}^{\{i\}}\} := \{u_1^i,\ \ldots,\ u_{N^e}^i\}^{\rm T} = \mathbf{z}_1$, where

$$\mathbf{z}_1 = \{\ z_{1{\rm I}}\ \} := \{\ +1,\ -1,\ +1,\ -1\ \}^{\rm T}\ ,\quad \text{for } N^e = 4\ ,$$
$$\mathbf{z}_1 = \{\ z_{1{\rm I}}\ \} := \{\ -1,\ -1,\ -1,\ -1,\ +1,\ +1,\ +1,\ +1,\ 0\ \}^{\rm T}\ ,\quad \text{for } N^e = 9\ , \tag{2.7}$$

produces zero strain at the reduced integration point(s), i.e., $\mathbf{B}_{die}^i\mathbf{z}_1 = 0$, independently of

the element shape. Concerning the spurious rotation modes, provided the element has constant thickness and constant field of local triads, we have $\mathbf{B}^{\alpha}_{rot}\mathbf{z}_1 = 0$ for $N^e = 4$, and $\mathbf{B}^{\alpha}_{rot}(\mathbf{r} - 3\mathbf{z}_1) = 0$ for $N^e = 9$, independently of element shape, with $\mathbf{r} := \{1,...,1\}^{\mathrm{T}} \in \mathbb{R}^{N^e}$ being the rigid body mode.

Let $\widetilde{\mathbf{K}}^e$ denote the under-integrated element stiffness, and $\delta\mathbf{K}^e$ a perturbation matrix. We have proposed in Vu-Quoc & Mora [1987] an efficient construction of $\delta\mathbf{K}^e$, which is carried out directly in the global coordinates (thus avoiding unnecessary local-global transformations), and based on the spurious (hourglass) mode $\mathbf{z}_1$ such that this mode produces a small non-zero energy in the perturbed stiffness $\mathbf{K}^{e*} = \widetilde{\mathbf{K}}^e + \delta\mathbf{K}^e$. Further, this perturbation must be orthogonal to linear displacement field in general curved shell elements (4-node or 9-node), and to quadratic displacement field in flat 9-node shell elements. That is, the perturbation should not generate any additional energy for displacements that are linear (for general curved elements) or quadratic (for flat elements) functions in the coordinates. As a result, the element passes basic patch tests (including the pure bending test of a flat shell with quadratic displacement field), and is free of spurious modes in a large number of static problems. Further, the perturbed stiffness thus constructed is robust with respect to element distortion. We refer to Vu-Quoc & Mora [1987] for the details.

2.2. Inertia operator. Let $\boldsymbol{\eta}^*$ be the admissible variation of $\mathbf{u}^*$ in the 3-D case, and similarly let (η, ξ) be the variations of $(\mathbf{u}, \boldsymbol{\chi})$. The same relationship as in (2.1) holds for these variations. The variational form of the inertia operator of the shell then leads to

$$\int_{\Omega} \boldsymbol{\eta}^* \cdot \ddot{\mathbf{u}}^* \mathrm{d}\Omega = \int_{\Omega} \left\{ \eta \cdot \ddot{\mathbf{u}} + \frac{\theta^3 h}{2} \left[\xi \cdot \mathbf{T}_3 \times \ddot{\mathbf{u}} + \eta \cdot \ddot{\boldsymbol{\chi}} \times \mathbf{T}_3 \right] + \left(\frac{\theta^3 h}{2} \right)^2 \xi \cdot \ddot{\boldsymbol{\chi}} \right\} \mathrm{d}\Omega \,. \tag{2.8}$$

where a superposed "$\cdot$" denotes time differentiation, and $\mathbf{1}_p$ the $p \times p$ identity matrix. Introducing the spatial discretization

$$\eta^*(\theta^{\{i\}}) \approx \sum_{I=1}^{N} P_I(\theta^{\{\alpha\}}) \eta_I^*(\theta^3) \,, \quad \mathbf{u}^*(\theta^{\{i\}}) \approx \sum_{I=1}^{N} P_I(\theta^{\{\alpha\}}) \mathbf{u}_I^*(\theta^3) \,, \tag{2.9a}$$

$$\xi(\theta^{\{\alpha\}}) \approx \sum_{I=1}^{N} P_I(\theta^{\{\alpha\}})\xi_I\,, \quad \chi(\theta^{\{\alpha\}}) \approx \sum_{I=1}^{N} P_I(\theta^{\{\alpha\}})\chi_I\,, \tag{2.9b}$$

into (2.8), we obtain the mass matrix $\mathbf{M}$, whose submatrix $\mathbf{M}_{IJ}$ coupling the dof's at node I to those at node J is given below

$$\mathbf{M}_{IJ} := \begin{bmatrix} \mathbf{M}_{IJ}^{11} & \mathbf{M}_{IJ}^{12} \\ \mathbf{M}_{IJ}^{21} & \mathbf{M}_{IJ}^{22} \end{bmatrix} \in \mathbb{R}^{5\times 5}\,, \quad \Theta_I := \begin{bmatrix} -T_{2I}^1 & -T_{2I}^2 & -T_{2I}^3 \\ T_{1I}^1 & T_{1I}^2 & T_{1I}^3 \end{bmatrix}, \quad \mathbf{T}_{\alpha I} = T_{\alpha I}^i \mathbf{E}_i\,, \tag{2.10a}$$

$$\mathbf{M}_{IJ}^{11} := \left(\int_{\Omega^e} P_I P_J \mathrm{d}\Omega \right) \mathbf{1}_3 \in \mathbb{R}^{3\times 3}\,, \quad \mathbf{M}_{IJ}^{12} := \left(\frac{h_J}{2} \int_{\Omega^e} \theta^3 P_I P_J \mathrm{d}\Omega \right) \Theta_J^{\mathrm{T}} \in \mathbb{R}^{3\times 2}\,,\dagger \tag{2.10b}$$

$$\mathbf{M}_{IJ}^{21} := \left(\frac{h_I}{2} \int_{\Omega^e} \theta^3 P_I P_J \mathrm{d}\Omega \right) \Theta_I \in \mathbb{R}^{2\times 3}\,, \quad \mathbf{M}_{IJ}^{22} := \left(\frac{h_I h_J}{4} \int_{\Omega^e} (\theta^3)^2 P_I P_J \mathrm{d}\Omega \right) \Theta_I \Theta_J^{\mathrm{T}} \in \mathbb{R}^{2\times 2}\,,\dagger \tag{2.10c}$$

for I, J = 1,...,N^e. A modified mass matrix can be obtained to account for homogeneous rotation boundary conditions, prescribed along an arbitrary axis lying in the plane ($\mathbf{T}_1$, $\mathbf{T}_2$), but not collinear with either $\mathbf{T}_1$ or $\mathbf{T}_2$, following the same procedure applied for the stiffness matrix as proposed in Vu-Quoc & Mora [1987].

Remark 2.1. The integrals in (2.10), corresponding to a full mass matrix, are numerically evaluated using full (3×3) integration with the Gauss-Legendre quadrature rule. To obtain a diagonal (lumped) mass matrix, we use the Gauss-Lobatto (nodal) quadrature, and neglect the coupling terms in $\mathbf{M}_{(II)}^{12}$. The result is a diagonal mass matrix with

$$\mathbf{M}_{(II)}^{11} = \left(\int_{\Omega^e} (P_I)^2 \mathrm{d}\Omega \right) \mathbf{1}_3 \in \mathbb{R}^{3\times 3}\,, \quad \mathbf{M}_{(II)}^{22} = \left(\frac{(h_I)^2}{4} \int_{\Omega^e} (P_I)^2 \mathrm{d}\Omega \right) \mathbf{1}_2 \in \mathbb{R}^{2\times 2}\,, \tag{2.11}$$

where the equality $\Theta_{(I)}\Theta_{(I)}^{\mathrm{T}} = \mathbf{1}_2$ had been used. □

Remark 2.2. Parallel to the expression for the element stiffness in (2.6), we can write the element mass matrix as follows

$$\mathbf{M}^e = \int_{\Omega^e} \underset{\substack{i,j \in \{1,2,3\} \\ \alpha,\beta \in \{1,2\}}}{A} \left[\left(\mathbf{P}_{dis}^i\right)^{\mathrm{T}} \mathbf{P}_{dis}^j \oplus \left(\mathbf{P}_{rot}^\alpha\right)^{\mathrm{T}} \mathbf{P}_{rot}^\beta \oplus \left(\mathbf{P}_{dis}^i\right)^{\mathrm{T}} \mathbf{P}_{rot}^\beta \oplus \left(\mathbf{P}_{rot}^\alpha\right)^{\mathrm{T}} \mathbf{P}_{dis}^j \right] \mathrm{d}\Omega \in \mathbb{R}^{n^e \times n^e}\,,$$

† No sum on repeated indices in these formulae.

(2.12a)

where, with δ_{ij} being the Kronecker delta, the matrices $\mathbf{P}^i_{die}$ and $\mathbf{P}^\alpha_{rot}$ are defined by

$$\mathbf{P}^i_{die} := \begin{Bmatrix} \delta_{i1} \\ \delta_{i2} \\ \delta_{i3} \end{Bmatrix} \{ P_1 , \ldots , P_{N^e} \} \in \mathbb{R}^{3\times N^e} , \tag{2.12b}$$

$$\mathbf{P}^\alpha_{rot} := \frac{1}{2}\theta^3 e_{\alpha\beta} \begin{bmatrix} \{ h_1 P_1 T^1_{\beta 1} , \ldots , h_{N^e} P_{N^e} T^1_{\beta N^e} \} \\ \{ h_1 P_1 T^2_{\beta 1} , \ldots , h_{N^e} P_{N^e} T^2_{\beta N^e} \} \\ \{ h_1 P_1 T^3_{\beta 1} , \ldots , h_{N^e} P_{N^e} T^3_{\beta N^e} \} \end{bmatrix} \in \mathbb{R}^{3\times N^e} . \tag{2.12c}$$

Expression (2.12a) will be subsequently used in the construction of a projected mass matrix for a complete filtering of spurious dynamics. □

3. Spurious zero-energy modes. Perturbed stiffness matrix

In this section, we will focus our attention strictly to the 9-node shell element. The perturbation stiffness matrix for this element, constructed based on the hourglass mode $\mathbf{z}_1$ alone, does not completely filter all possible spurious zero-energy modes for certain element geometry, but those corresponding to mode $\mathbf{z}_1$. That is, the perturbed stiffness is still rank deficient. Here, we will characterize the additional spurious modes, as well as propose a perturbation matrix that completely compensates the rank of an under-integrated stiffness matrix, and includes the previously used perturbation matrix, which is based only on mode $\mathbf{z}_1$, as a particular case. Exact expressions of these additional spurious zero-energy modes, which depends on element shape, are given for some particular geometrical shapes. The present 9-node shell element passes several higher-order patch tests, in addition to the basic ones reported in Vu-Quoc & Mora [1987]. The new perturbation matrix not only duplicates the performance of the old one, but in fact constitutes the first stage of the proposed perturbation method for dynamic analyses.

3.1. Spurious zero-energy modes in a bi-unit square element. Consider a square 9-node element with length 2 on each side and nodal coordinates as given in (2.4b). The element has uniform thickness h. At the reduced-integration points, $\mathbf{A}_i \equiv \mathbf{T}_i \equiv \mathbf{E}_i$, for $i = 1,2,3$. Similarly, let the local triads at the nodes coincide with the global basis. Define the matrices $\mathbf{z}_2$, $\mathbf{z}_3$, and $\mathbf{z}_4$ as follows

$$\begin{aligned} \mathbf{z}_2 = \{\, z_{2I} \,\} &:= \{\, -1,\, 1,\, 1,\, -1,\, 0,\, -\tfrac{1}{2},\, 0,\, \tfrac{1}{2},\, 0 \,\}^{\mathrm{T}} \in \mathbb{R}^{9\times 1}\,, \\ \mathbf{z}_3 = \{\, z_{3I} \,\} &:= \{\, 1,\, 1,\, -1,\, -1,\, -\tfrac{1}{2},\, 0,\, \tfrac{1}{2},\, 0,\, 0 \,\}^{\mathrm{T}} \in \mathbb{R}^{9\times 1}\,, \\ \mathbf{z}_4 = \{\, z_{4I} \,\} &:= \mathbf{r} - 3\mathbf{z}_1 = \{\, 4,\, 4,\, 4,\, 4,\, -2,\, -2,\, -2,\, -2,\, 1 \,\}^{\mathrm{T}} \in \mathbb{R}^{9\times 1}\,. \end{aligned} \tag{3.1}$$

It has been shown that at the reduced-integration points $(\theta^1, \theta^2) = (\pm \frac{1}{\sqrt{3}}, \pm \frac{1}{\sqrt{3}})$,

$$\mathbf{B}^i_{die}\mathbf{z}_1 = 0\,, \text{ for } i = 1,2,3\,, \quad \text{and} \quad \mathbf{B}^\alpha_{rot}\mathbf{z}_4 = 0\,, \text{ for } \alpha = 1,2\,, \tag{3.2a}$$

independently of the transverse coordinate θ^3. On the other hand, we have

$$\mathbf{B}^1_{die}\mathbf{z}_2 + \mathbf{B}^2_{die}\mathbf{z}_3 = \left\{ -\frac{3(\theta^2)^2 - 1}{2},\ \frac{3(\theta^1)^2 - 1}{2},\ 0,\ 0,\ 0 \right\}^{\mathrm{T}}, \tag{3.2b}$$

$$\mathbf{B}^1_{rot}\mathbf{z}_3 - \mathbf{B}^2_{rot}\mathbf{z}_2 = \frac{1}{2}\left\{ -\theta^3\,\frac{3(\theta^2)^2 - 1}{2},\ \theta^3\,\frac{3(\theta^1)^2 - 1}{2},\ \theta^2\,\frac{3(\theta^1)^2 - 1}{2},\ -\theta^1\,\frac{3(\theta^2)^2 - 1}{2},\ 0 \right\}^{\mathrm{T}}. \tag{3.2c}$$

The equations in (3.2b) and (3.2c) vanish for $\theta^1 = \theta^2 = \pm \frac{1}{\sqrt{3}}$, i.e., at the reduced-integration points, and independently of the transverse coordinate θ^3 in both displacement mode as well as in rotation mode. The matrices $\mathbf{z}_1$, $\mathbf{z}_2$, $\mathbf{z}_3$, and $\mathbf{z}_4$ are therefore the matrix representation of spurious zero-energy modes of an under-integrated stiffness matrix of a bi-unit 9-node shell element. It should be noted that while $\{\hat{u}^{(i)}_I\} = \mathbf{z}_1$ is a spurious zero-energy mode for any $i = 1,2,3$, the column-matrices $\mathbf{z}_2$ and $\mathbf{z}_3$ always appear together in a related spurious mode: for instance, in a spurious displacement mode with components $\{\hat{u}^1_I\} = \mathbf{z}_2$ and $\{\hat{u}^2_I\} = \mathbf{z}_3$, and in a spurious rotation mode with components $\{\hat{\chi}^1_I\} = \mathbf{z}_3$ and $\{\hat{\chi}^2_I\} = -\mathbf{z}_2$.

We have thus identified all possible zero-energy modes of a square bi-unit shell element lying in the plane $\{\mathbf{e}_1, \mathbf{e}_2\}$. There are in total seven independent spurious modes:

$$\begin{bmatrix} \{\hat{u}_I^1\} \\ \{\hat{u}_I^2\} \\ \{\hat{u}_I^3\} \\ \{\hat{\chi}_I^1\} \\ \{\hat{\chi}_I^2\} \end{bmatrix} = \begin{bmatrix} \mathbf{z}_1 \\ 0 \\ 0 \\ 0 \\ 0 \end{bmatrix}, \begin{bmatrix} 0 \\ \mathbf{z}_1 \\ 0 \\ 0 \\ 0 \end{bmatrix}, \begin{bmatrix} 0 \\ 0 \\ \mathbf{z}_1 \\ 0 \\ 0 \end{bmatrix}, \begin{bmatrix} \mathbf{z}_2 \\ \mathbf{z}_3 \\ 0 \\ 0 \\ 0 \end{bmatrix}, \begin{bmatrix} 0 \\ 0 \\ 0 \\ \mathbf{z}_3 \\ -\mathbf{z}_2 \end{bmatrix}, \begin{bmatrix} 0 \\ 0 \\ 0 \\ \mathbf{z}_4 \\ 0 \end{bmatrix}, \begin{bmatrix} 0 \\ 0 \\ 0 \\ 0 \\ \mathbf{z}_4 \end{bmatrix} \in \mathbb{R}^{45\times 1} . \tag{3.3}$$

Remark 3.1. Note the difference between the left-hand sides of equations (3.2b) and (3.2c). The reason is that while $\mathbf{B}^i_{dis}$ depends only on the components of the tangent vectors $\mathbf{A}_i$, the matrix $\mathbf{B}^\alpha_{rot}$ depends on the relative orientation between the vectors $\{\mathbf{A}_i\}$ and $\{\mathbf{T}_i\}$. Thus the same left-hand side as in (3.2b) will be obtained for (3.2c), i.e., $\mathbf{B}^{1+}_{rot}\mathbf{z}_2 + \mathbf{B}^{2+}_{rot}\mathbf{z}_3 = \mathbf{0}$ at the reduced-integration points, if we choose the new local triads to be such that $\mathbf{T}_1^+ = \mathbf{T}_2$, $\mathbf{T}_2^+ = -\mathbf{T}_1$, and $\mathbf{T}_3^+ \equiv \mathbf{T}_3$. □

Remark 3.2. The following important *orthogonal property* holds among the modes $\mathbf{r}$, $\mathbf{z}_1$, $\mathbf{z}_2$, $\mathbf{z}_3$, and $\mathbf{z}_4$:

$$\mathbf{r} \bullet \mathbf{z}_i = 0 , \quad \text{for } i = 1,2,3 , \tag{3.4a}$$

$$\mathbf{z}_i \bullet \mathbf{z}_j = 0 , \quad \text{for } i \neq j , \quad \text{and} \quad i,j = 1,2,3 , \tag{3.4b}$$

$$\mathbf{z}_4 \bullet \mathbf{z}_2 = \mathbf{z}_4 \bullet \mathbf{z}_3 = 0 . \tag{3.4c}$$

That is, $\{\mathbf{r}, \mathbf{z}_1, \mathbf{z}_2, \mathbf{z}_3\}$ forms a set of orthogonal vectors in $\mathbb{R}^9$; similarly, $\{\mathbf{z}_2, \mathbf{z}_3, \mathbf{z}_4\}$ is yet another set of orthogonal vectors in $\mathbb{R}^9$. □

We will later make use of the above orthogonal property to achieve a complete filtering of spurious modes, specifically in the construction of the perturbed under-integrated stiffness matrix and of the projection operator for the mass matrix.

3.2. Spurious zero-energy modes in 9-node shell elements. We now examine how zero-energy spurious modes change under element distortion, and under arbitrary orientation of the element in space. From our previous investigation, we already know that the three displacement modes ($i = 1,2,3$) with component $\{\hat{u}_I^{(i)}\} = \mathbf{z}_1$ are spurious zero-energy modes regarless of element shape and orientation. For some particular field

of local triads, the two spurious rotation modes ($\alpha = 1,2$) with component $\{\hat{\chi}_I^{(\alpha)}\} = \mathbf{z}_4$ has the same invariant property with respect to element shape (see Vu-Quoc & Mora [1987]); this is, however, not the case for a general field of triads. On the other hand, the two spurious modes with components equal to $\{\mathbf{z}_2\}$ and to $\{\mathbf{z}_3\}$ do not share the above invariant property. That is, the matrix representation of these spurious modes has coefficients that vary with element distortion and orientation.

Consider an arbitrary distortion of a bi-unit 9-node square element. The distorted element (which could be non-flat) can be thought of as a result of a continuous deformation process started from the bi-unit square element. The dimension of the null space of the under-integrated stiffness $\widetilde{\mathbf{K}}$ of a distorted element can collapse down from seven (for the bi-unit element) to a smaller dimension. In general, as the distortion proceeds, the null space of the under-integrated stiffness changes with the degree of distortion, i.e., the null space depends on the Jacobian matrix. We recall that this null space contains an invariant subspace, spanned by the three ($i = 1,2,3$) displacement modes with non-zero component $\{\hat{u}_I^i\} = \mathbf{z}_1$.

For general shell elements, it is not easy to evaluate analytical expressions of the (variant) spurious modes, so that a corresponding filtering scheme could be devised. For some particular element geometry and field of local triads, however, analytical expressions of spurious modes can be explicitly given. This will shed some light into how spurious modes evolve with element distortion. Knowing such evolution is of fundamental importance for designing an efficient and reliable perturbation method.

3.2.1. Parallelogrammic element with normal director field. As portrayed in Figure 3.1, the 9-node element, contained in the plane $\{\mathbf{E}_1, \mathbf{E}_2\}$, has identical tangent vectors $\{\mathbf{A}_i\}$ at all 2×2 integration points, with $\mathbf{A}_1$ chosen to be collinear with $\mathbf{E}_1$. The element has a constant normal director field, $\mathbf{A}_3 \equiv \mathbf{E}_3$. Further, the local triads are chosen to be identical to the global base vectors, $\mathbf{T}_{iI} \equiv \mathbf{E}_i$, for $i = 1,2,3$ and $I = 1,\ldots,9$. We have

$$\mathbf{A}_1 \bullet \mathbf{T}_{1\mathrm{I}} = A_1^1 \ , \quad \mathbf{A}_1 \bullet \mathbf{T}_{2\mathrm{I}} = 0 \ , \quad \mathbf{A}_2 \bullet \mathbf{T}_{\alpha\mathrm{I}} = A_2^\alpha \ ,$$
$$\mathbf{A}_3 \bullet \mathbf{T}_{\alpha\mathrm{I}} = 0 \ , \quad \forall \quad \alpha = 1,2 \ . \tag{3.5}$$

This particular choice of position of the element facilitates the search for spurious modes; in the subsequent section, we will show how to obtain expressions of these spurious modes for arbitrary positioning of the element in space. Here, we study the evolution of spurious modes under the distortional mapping of a bi-unit square into a parallelogrammic element.

The mode with components $\{\hat{u}_\mathrm{I}^1\} = \mathbf{z}_2$ and $\{\hat{u}_\mathrm{I}^2\} = \mathbf{z}_3$ no longer produces zero strain at the reduced-integration points $(\theta^1, \theta^2) = (\pm \frac{1}{\sqrt{3}}, \pm \frac{1}{\sqrt{3}})$, because

$$\mathbf{B}_{dis}^1 \mathbf{z}_2 + \mathbf{B}_{dis}^2 \mathbf{z}_3 = \frac{1}{2} \begin{Bmatrix} -A_1^1 \dfrac{3(\theta^2)^2 - 1}{2} \\ -3A_2^1 \theta^1 \theta^2 \\ 0 \\ 0 \\ -\dfrac{1}{2}\left[A_2^1 [3(\theta^2)^2 - 1] + 6A_1^1 \theta^1 \theta^2\right] \end{Bmatrix} + \frac{1}{2} \begin{Bmatrix} 0 \\ A_2^2 \dfrac{3(\theta^1)^2 - 1}{2} \\ 0 \\ 0 \\ 3A_2^2 \theta^1 \theta^2 \end{Bmatrix} \tag{3.6}$$

has non-vanishing second coefficient (for $A_2^1 \neq 0$, since $A_2^1 = 0$ is a trivial case) and fifth coefficient ($A_1^1 \neq 0$). Noting, however, that

$$\mathbf{B}_{dis}^2 \mathbf{z}_2 = \frac{1}{2} \left\{ 0, -3A_2^2 \theta^1 \theta^2, 0, 0, -A_2^2 \frac{3(\theta^2)^2 - 1}{2} \right\}^\mathrm{T} , \tag{3.7}$$

then together with (3.6), one can see that a judicious choice of linear combination of $\mathbf{z}_2$ and $\mathbf{z}_3$ is possible to nullify the strains at the reduced-integration points. Indeed, a displacement mode with components $\{\hat{u}_\mathrm{I}^1\} = A_2^2 \mathbf{z}_2$ and $\{\hat{u}_\mathrm{I}^2\} = (A_1^1 \mathbf{z}_3 - A_2^1 \mathbf{z}_2)$ leads to the strain field

$$\mathbf{B}_{dis}^1 (A_2^2 \mathbf{z}_2) + \mathbf{B}_{dis}^2 (A_1^1 \mathbf{z}_3 - A_2^1 \mathbf{z}_2) = \frac{A_1^1 A_2^2}{4} \left\{ -[3(\theta^2)^2 - 1], [3(\theta^1)^2 - 1], 0, 0, 0 \right\}^\mathrm{T} , \tag{3.8}$$

which clearly vanishes at $\theta^1 = \theta^2 = \pm \frac{1}{\sqrt{3}}$.

Similarly, the rotation mode with components $\{\hat{\chi}_I^1\} = \mathbf{z}_3$ and $\{\hat{\chi}_I^2\} = -\mathbf{z}_2$ no longer yields zero strains at the reduced-integration points in the parallelogrammic element, as it did in the bi-unit square element:

$$\mathbf{B}^1_{rot}\mathbf{z}_3 - \mathbf{B}^2_{rot}\mathbf{z}_2 = \frac{1}{2}\begin{Bmatrix} 0 \\ A_2^2\dfrac{3(\theta^1)^2-1}{2} \\ A_2^2\theta^2\dfrac{3(\theta^1)^2-1}{2} \\ 0 \\ 3A_2^2\theta^1\theta^2\theta^3 \end{Bmatrix} - \frac{1}{2}\begin{Bmatrix} A_1^1\theta^3\dfrac{3(\theta^2)^2-1}{2} \\ 3A_2^1\theta^1\theta^2\theta^3 \\ A_2^1\theta^1\dfrac{3(\theta^2)^2-1}{2} \\ A_1^1\theta^1\dfrac{3(\theta^2)^2-1}{2} \\ \dfrac{\theta^3}{2}\left[A_2^1[3(\theta^2)^2-1] + 6A_1^1\theta^1\theta^2\right] \end{Bmatrix}. \tag{3.9}$$

But noticing that

$$\mathbf{B}^1_{rot}\mathbf{z}_2 = \left\{0,\ -3A_2^2\theta^1\theta^2\theta^3,\ -A_2^2\theta^1\frac{3(\theta^2)^2-1}{2},\ 0,\ -A_2^2\theta^3\frac{3(\theta^2)^2-1}{2}\right\}^{\mathrm{T}}, \tag{3.10}$$

similar to the displacement case, we consider the rotation mode with components $\{\hat{\chi}_I^1\} = (A_1^1\mathbf{z}_3 - A_2^1\mathbf{z}_2)$ and $\{\hat{\chi}_I^2\} = A_2^2\mathbf{z}_2$, which then yields vanishing strains at the reduced-integration points:

$$\mathbf{B}^1_{rot}(A_1^1\mathbf{z}_3 - A_2^1\mathbf{z}_2) - \mathbf{B}^2_{rot}(A_2^2\mathbf{z}_2) =$$

$$A_1^1A_2^2\left\{-\theta^3\,[3(\theta^2)^2-1],\ \theta^3\,[3(\theta^1)^2-1],\ \theta^2\,[3(\theta^1)^2-1],\ -\theta^1\,[3(\theta^2)^2-1]\right\}^{\mathrm{T}}. \tag{3.11}$$

Again, recall that Remark 3.1 applies to the present case as well. On the other hand, $\mathbf{z}_4$ remains a matrix representation of spurious rotation modes for this element, since

$$\mathbf{B}^1_{rot}\mathbf{z}_4 = \left\{0,\ 6A_2^2\theta^2\theta^3[3(\theta^1)^2-1],\ A_2^2[3(\theta^1)^2-1][3(\theta^2)^2-1],\ 0,\ 6A_2^2\theta^1\theta^3[3(\theta^2)^2-1]\right\}^{\mathrm{T}}, \tag{3.12a}$$

and

$$\mathbf{B}^2_{rot}\mathbf{z}_4 = -\begin{Bmatrix} 6A_1^1\theta^1\theta^3[3(\theta^2)^2-1] \\ 6A_2^1\theta^2\theta^3[3(\theta^1)^2-1] \\ A_2^1[3(\theta^1)^2-1][3(\theta^2)^2-1] \\ A_1^1[3(\theta^1)^2-1][3(\theta^2)^2-1] \\ 6\theta^3\left[A_2^1\theta^1[3(\theta^2)^2-1] + A_1^1\theta^2[3(\theta^1)^2-1]\right] \end{Bmatrix} \tag{3.12b}$$

vanish identically at the reduced-integration points. Thus, for the parallelogrammic element with constant normal director field, the seven independent spurious zero-energy modes, given in (3.3) for the bi-unit square element, now become

$$\begin{bmatrix} \{\hat{u}_I^1\} \\ \{\hat{u}_I^2\} \\ \{\hat{u}_I^3\} \\ \{\hat{\chi}_I^1\} \\ \{\hat{\chi}_I^2\} \end{bmatrix} = \begin{bmatrix} \mathbf{z}_1 \\ 0 \\ 0 \\ 0 \\ 0 \end{bmatrix}, \begin{bmatrix} 0 \\ \mathbf{z}_1 \\ 0 \\ 0 \\ 0 \end{bmatrix}, \begin{bmatrix} 0 \\ 0 \\ \mathbf{z}_1 \\ 0 \\ 0 \end{bmatrix}, \begin{bmatrix} A_2^2 \mathbf{z}_2 \\ A_1^1 \mathbf{z}_3 - A_2^1 \mathbf{z}_2 \\ 0 \\ 0 \\ 0 \end{bmatrix}, \begin{bmatrix} 0 \\ 0 \\ 0 \\ A_1^1 \mathbf{z}_3 - A_2^1 \mathbf{z}_2 \\ -A_2^2 \mathbf{z}_2 \end{bmatrix}, \begin{bmatrix} 0 \\ 0 \\ 0 \\ \mathbf{z}_4 \\ 0 \end{bmatrix}, \begin{bmatrix} 0 \\ 0 \\ 0 \\ 0 \\ \mathbf{z}_4 \end{bmatrix} \in \mathbb{R}^{45\times 1} . \quad (3.13)$$

3.2.1. Cylindrical element. The geometry of a cylindrical 9-node shell element, with uniform thickness, is depicted in Figure 3.2a. The nodal coordinates of the element has the plane $\{\mathbf{E}_2, \mathbf{E}_3\}$ as plane of symmetry. The orientation of the director field and the local triads has important influence on the spurious modes, as can be observed from expressions of the strain-displacement matrices $\mathbf{B}^i_{dis}$ and $\mathbf{B}^\alpha_{rot}$. Corresponding to the matrix representation $\{\mathbf{z}_2, \mathbf{z}_3\}$, instead of (3.2b), we obtain for the displacement field

$$\mathbf{B}^1_{dis}\mathbf{z}_2 + \mathbf{B}^2_{dis}\mathbf{z}_3 =$$

$$\left\{ -A_1^1 \ \frac{3(\theta^2)^2-1}{2}, A_2^2 \ \frac{3(\theta^1)^2-1}{2}, -3A_3^1\theta^1\theta^2, -A_3^1 \ \frac{3(\theta^2)^2-1}{2}, 3(-A_1^1 + A_2^2)\theta^1\theta^2 \right\}^T , \quad (3.14)$$

where we recall that $A_i^I = \mathbf{A}_i \bullet \mathbf{E}^I \equiv \mathbf{A}_i \bullet \mathbf{E}_I$. In (3.14), the fifth coefficient of $\mathbf{B}^1_{dis}\mathbf{z}_2$ is $(-3A_1^1\theta^1\theta^2)$, whereas the fifth coefficient of $\mathbf{B}^2_{dis}\mathbf{z}_3$ is $3A_2^2\theta^1\theta^2$. At the reduced-integration points $(\theta^1,\theta^2) = (\pm\frac{1}{\sqrt{3}},\pm\frac{1}{\sqrt{3}})$, the first, second, and fourth coefficients in (3.14) vanish. The third and the fifth coefficients do not vanish in general. We shall consider the following two cases of director field.

3.2.2a. Case with constant director field $\mathbf{A}_3 \equiv \mathbf{E}_3$. We consider first the simple case where $\mathbf{T}_{iI} \equiv \mathbf{E}_i$, for $i = 1,2,3$. Then by virtue of $(2.5)_2$, we have that $\mathbf{A}_3 \equiv \mathbf{T}_3 \equiv \mathbf{E}_3$ everywhere in the element, and thus $A_3^1 = 0$. This assumption therefore leads to the vanishing of the third coefficient. This situation is depicted in Figure 3.2b. From (3.14), one can see that the matrix representation of spurious mode with components $\{\hat{u}_I^1\} = \mathbf{z}_2$

and $\{\hat{u}_I^2\} = \mathbf{z}_3$ changes to $\{\hat{u}_I^1\} = \mathbf{z}_2/A_1^1$ and $\{\hat{u}_I^2\} = \mathbf{z}_3/A_2^2$ (or equivalently to $\{\hat{u}_I^1\} = A_2^2\mathbf{z}_2$ and $\{\hat{u}_I^2\} = A_1^1\mathbf{z}_3$), so that $\mathbf{B}_{die}^1\{\hat{u}_I^1\} + \mathbf{B}_{die}^2\{\hat{u}_I^2\} \equiv 0$ at the reduced-integration points. This identity holds at all 2×2 reduced-integration points because, for the current choice of geometry and orientation of the element, the components A_1^1 and A_2^2 are constant throughout the element. Note that the above matrix representation clearly holds also for the case where $A_1^1 = A_2^2$.

For the rotation field, a similar modified matrix representation of spurious mode is obtained. Again, since $\mathbf{A}_1 \bullet \mathbf{T}_{1I} = \mathbf{A}_1 \bullet \mathbf{E}_1 = A_1^1$ is the same at all reduced-integration points, for all I = 1,...,9, we obtain instead of (3.2c)

$$\mathbf{B}_{rot}^1\mathbf{z}_3 - \mathbf{B}_{rot}^2\mathbf{z}_2 = \frac{1}{2}\left\{-A_1^1\theta^3\,\frac{3(\theta^2)^2-1}{2},\ A_2^2\theta^3\,\frac{3(\theta^1)^2-1}{2},\right.$$

$$\left. A_2^2\theta^2\,\frac{3(\theta^1)^2-1}{2},\ -A_1^1\theta^1\,\frac{3(\theta^2)^2-1}{2},\ 3(A_2^2-A_1^1)\theta^1\theta^2\theta^3\right\}^{\mathrm{T}}. \tag{3.15}$$

The first four coefficients vanish identically at the reduced-integration points. Unless $A_1^1 = A_2^2$, the last coefficient will vanish for the spurious rotation mode with components $\{\hat{\chi}_I^1\} = \mathbf{z}_3/A_2^2$ and $\{\hat{\chi}_I^2\} = -\mathbf{z}_2/A_1^1$ (or with components $\{\hat{\chi}_I^1\} = A_1^1\mathbf{z}_3$ and $\{\hat{\chi}_I^2\} = -A_2^2\mathbf{z}_2$). Also, we recall Remark 3.1 for the present situation.

On the other hand, $\mathbf{z}_4$ remains the matrix representation of spurious rotation modes, since

$$\mathbf{B}_{rot}^1\mathbf{z}_4 = \frac{A_2^2}{2}\left\{0,\ 6\theta^2\theta^3[3(\theta^1)^2-1],\ [3(\theta^1)^2-1][3(\theta^2)^2-1],\ 0,\ 6\theta^1\theta^3[3(\theta^2)^2-1]\right\}, \tag{3.16a}$$

$$\mathbf{B}_{rot}^2\mathbf{z}_4 = -\frac{A_1^1}{2}\left\{6\theta^1\theta^3[3(\theta^2)^2-1],\ 0,\ 0,\ [3(\theta^1)^2-1][3(\theta^2)^2-1],\ 6\theta^2\theta^3[3(\theta^1)^2-1]\right\} \tag{3.16b}$$

vanish at the reduced-integration points. Thus, for the cylindrical element with constant director field, there are seven independent spurious zero-energy modes with matrix representation

$$\begin{bmatrix} \{\hat{u}_I^1\} \\ \{\hat{u}_I^2\} \\ \{\hat{u}_I^3\} \\ \{\hat{\chi}_I^1\} \\ \{\hat{\chi}_I^2\} \end{bmatrix} = \begin{bmatrix} \mathbf{z}_1 \\ 0 \\ 0 \\ 0 \\ 0 \end{bmatrix}, \begin{bmatrix} 0 \\ \mathbf{z}_1 \\ 0 \\ 0 \\ 0 \end{bmatrix}, \begin{bmatrix} 0 \\ 0 \\ \mathbf{z}_1 \\ 0 \\ 0 \end{bmatrix}, \begin{bmatrix} A_2^2 \mathbf{z}_2 \\ A_1^1 \mathbf{z}_3 \\ 0 \\ 0 \\ 0 \end{bmatrix}, \begin{bmatrix} 0 \\ 0 \\ 0 \\ A_1^1 \mathbf{z}_3 \\ -A_2^2 \mathbf{z}_2 \end{bmatrix}, \begin{bmatrix} 0 \\ 0 \\ 0 \\ \mathbf{z}_4 \\ 0 \end{bmatrix}, \begin{bmatrix} 0 \\ 0 \\ 0 \\ 0 \\ \mathbf{z}_4 \end{bmatrix} \in \mathbb{R}^{45\times 1} , \tag{3.17}$$

which differs only slightly from (3.3).

3.2.2b. Case with radial director field. In the more general situation where the local triads $\{\mathbf{T}_{1I}, \mathbf{T}_{2I}, \mathbf{T}_{3I}\}$ are not identical to the global $\{\mathbf{E}_1, \mathbf{E}_2, \mathbf{E}_3\}$, i.e., when $A_3^1 \neq 0$, then the third coefficient in (3.14) corresponding to the strain Γ_{23} vanishes only for $\theta^1 = \theta^2 = 0$. To make this coefficient vanish, we have to bring in the contribution of the rotation field to the strain components, especially to Γ_{23}. Recall that the fifth coefficient in (3.14) corresponding to the strain Γ_{12} can be nullified by choosing $\{\hat{u}_I^1\} = A_2^2 \mathbf{z}_2$ and $\{\hat{u}_I^2\} = A_1^1 \mathbf{z}_3$ as done in the previous sub-section.

Consider the case where the director field is symmetric with respect to the plane $\{\mathbf{E}_2, \mathbf{E}_3\}$, as depicted in Figure 3.2c. As a result, the following symmetry conditions in the scalar product $(\mathbf{A}_j \bullet \mathbf{T}_{1I})$ hold

$$\begin{aligned} \mathbf{A}_1(\theta^1)\bullet\{\mathbf{T}_{11}, \mathbf{T}_{14}, \mathbf{T}_{18}\} &= \mathbf{A}_1(-\theta^1)\bullet\{\mathbf{T}_{12}, \mathbf{T}_{13}, \mathbf{T}_{16}\} , \\ \mathbf{A}_1(\theta^1)\bullet\{\mathbf{T}_{15}, \mathbf{T}_{17}, \mathbf{T}_{19}\} &= \mathbf{A}_1(-\theta^1)\bullet\{\mathbf{T}_{15}, \mathbf{T}_{17}, \mathbf{T}_{19}\} , \end{aligned} \tag{3.18a}$$

$$\begin{aligned} \mathbf{A}_3(\theta^1)\bullet\{\mathbf{T}_{11}, \mathbf{T}_{14}, \mathbf{T}_{18}\} &= -\mathbf{A}_3(-\theta^1)\bullet\{\mathbf{T}_{12}, \mathbf{T}_{13}, \mathbf{T}_{16}\} , \\ \mathbf{A}_3(\theta^1)\bullet\{\mathbf{T}_{15}, \mathbf{T}_{17}, \mathbf{T}_{19}\} &= -\mathbf{A}_3(-\theta^1)\bullet\{\mathbf{T}_{15}, \mathbf{T}_{17}, \mathbf{T}_{19}\} , \end{aligned} \tag{3.18b}$$

where to alleviate the notation we write $\mathbf{A}_j(\theta^1)$ instead of $\mathbf{A}_j(\theta^{\{i\}})$, since the symmetry conditions apply only to θ^1. We are looking for a displacement or rotation mode that yields a strain Γ_{23} proportional to the product $(\theta^1\theta^2)$, which will be used to nullify the third coefficient in $\mathbf{B}_{dis}^1(A_2^2 \mathbf{z}_2) + \mathbf{B}_{dis}^2(A_1^1 \mathbf{z}_3)$. To this end, defining the matrix

$$\mathbf{z}_5 := \{\ 1, -1, 1, -1, 0, 0, 0, 0, 0\ \}^{\mathrm{T}} \in \mathbb{R}^{9\times 1} , \tag{3.19}$$

and considering the rotation mode with component $\{\hat{\chi}_I^1\} = \mathbf{z}_5$, we have

$$\mathbf{B}_{rot}^1 \mathbf{z}_5 = A_2^2 \left\{ 0,\ \theta^1\theta^3,\ \theta^1\theta^2,\ 0,\ \theta^2\theta^3 \right\}^{\mathrm{T}} . \tag{3.20}$$

The strain component $\Gamma_{23} = A_2^2 \theta^1 \theta^2$ in (3.20) is what we need, but the other strain components are, however, not zero at the reduced-integration points. To nullify these strains, we consider the displacement mode with component $\{\hat{u}_I^2\} = \mathbf{z}_5$ to produce the desired strain field

$$\mathbf{B}_{dis}^2 \mathbf{z}_5 = A_2^2 \{\, 0,\, \theta^1,\, 0,\, 0,\, \theta^2 \,\}^{\mathrm{T}} . \tag{3.21}$$

It should be noted that the strains components in (3.20) depends on the transverse coordinate θ^3. Hence, the final step to obtain the sought-after expression for spurious zero-energy mode is to integrate the stiffness matrix through the thickness, i.e., with respect to θ^3. The strain-displacement matrices, especially $\mathbf{B}_{rot}^{\alpha}$, will be then given in resultant form.

To do this, we further assume that the director field is *radial*, and that the element is geometrically a perfect cylindrical shell. That is, the position vector of a material point within the shell body is not interpolated from position vectors of nodal points, but known analytically. The coordinate line θ^1 in this case is not a parabola, but a circular arc. The tangent vectors $\{\mathbf{A}_i\}$ to the (cylindrical) coordinate lines $(\theta^1, \theta^2, \theta^3)$ are therefore orthogonal. Without loss of generality, we further assume that $\|\mathbf{A}_1\| = d_1(R + d_2\theta^3)$, where d_α are normalizing constants so that $\theta^1, \theta^3 \in [-1, 1]$, and R the radius of the cylinder; also, $\|\mathbf{A}_2\| = (A_2^2)^2$, and $\|\mathbf{A}_3\| = 1$. The metric tensor $\mathbf{G} = G_{ij}\mathbf{A}^i \otimes \mathbf{A}^j$, with $G_{ij} = (\mathbf{A}_i \bullet \mathbf{A}_j)$, then has a diagonal matrix representation $[G_{ij}] = Diag[d_1^2(R + d_2\theta^3)^2, (A_2^2)^2, 1]$. The plane-stress elastic moduli matrix $[C^{ijkl}]$ can be shown to take the form (cf. Vu-Quoc & Mora [1987])

$$[C^{ijkl}] = \begin{bmatrix} C^{1111} & C^{1122} & & & \\ C^{1122} & C^{2222} & & & \\ & & C^{2233} & & \\ & & & C^{3311} & \\ & & & & C^{1122} \end{bmatrix}, \quad \begin{aligned} C^{1111} &= \frac{4\mu(\lambda + \mu)}{[d_1(R + d_2\theta^3)]^4(\lambda + 2\mu)}, \\ C^{1122} &= \frac{2\mu}{[A_2^2 d_1(R + d_2\theta^3)]^2(\lambda + 2\mu)}, \\ C^{2222} &= \frac{4\mu(\lambda + \mu)}{(A_2^2)^4(\lambda + 2\mu)}, \end{aligned} \tag{3.22a}$$

$$C^{2233} = \frac{\mu}{(A_2^2)^2}, \quad C^{3311} = \frac{\mu}{[d_1(R + d_2\theta^3)]^2}, \quad C^{1122} = \frac{\mu}{[A_2^2 d_1(R + d_2\theta^3)]^2}, \tag{3.22b}$$

where λ and μ are the Lamé's constants. Notice the decoupling between the in-plane strains (Γ_{11}, Γ_{22}), the transverse shear strains (Γ_{23}, Γ_{31}), and the in-plane shear strain Γ_{12}.

It should be noted that the tangent vectors $\{\mathbf{A}_i\}$ appearing in the expressions for the strain-displacement matrices $\mathbf{B}^i_{dis}$ and $\mathbf{B}^\alpha_{rot}$ in (2.3) need not necessarily be obtained according to the approximation in (2.5), but could be chosen independently from the interpolation of the displacement and rotation fields. Hence, since $\mathbf{T}_{2I} \equiv \mathbf{E}_2$, we have that $\mathbf{A}_1 \bullet \mathbf{T}_{2I} = \mathbf{A}_3 \bullet \mathbf{T}_{2I} = 0$, and therefore

$$\mathbf{B}^1_{rot} = \theta^3 h A_2^2 \begin{Bmatrix} \{0, \ldots, 0\} \\ \{P_{1,2}, \ldots, P_{9,2}\} \\ \{P_1, \ldots, P_9\} \\ \{0, \ldots, 0\} \\ \{P_{1,1}, \ldots, P_{9,1}\} \end{Bmatrix} \in \mathbb{R}^{5\times 9} . \tag{3.23}$$

It follows from the decoupling in the elastic moduli matrix (3.22) and from the expression of $\mathbf{B}^1_{rot}$ in (3.23) that an a-priori integration with respect to θ^3 leads to a *resultant* strain-displacement matrix similar to $\mathbf{B}^1_{rot}$ in (3.23), with some multiplicative factors to the strain components. Let c_1 and c_2 be those multiplicative factors, (3.20) becomes

$$\mathbf{B}^1_{rot}\mathbf{z}_5 = A_2^2 \left\{ 0,\ c_1\theta^1,\ c_2\theta^1\theta^2,\ 0,\ c_1\theta^2 \right\}^{\mathrm{T}} . \tag{3.24}$$

Hence, using (3.14), (3.21), and (3.24), a linear combination of the matrices $\mathbf{z}_2$, $\mathbf{z}_3$, and $\mathbf{z}_5$ can be found for the matrix representation of a spurious mode.

Note that for this cylindrical element, we still have the rotation mode with component $\{\hat{\chi}^1_I\} = \mathbf{z}_4$ as spurious zero-energy mode, since $\mathbf{B}^1_{rot}\mathbf{z}_4 = 0$ at the reduced-integration points. In summary, the null space of the under-integrated stiffness matrix for the cylindrical 9-node element with radial director field contains the following five spurious modes

$$\begin{bmatrix} \{\hat{u}_I^1\} \\ \{\hat{u}_I^2\} \\ \{\hat{u}_I^3\} \\ \{\hat{\chi}_I^1\} \\ \{\hat{\chi}_I^2\} \end{bmatrix} = \begin{bmatrix} \mathbf{z}_1 \\ 0 \\ 0 \\ 0 \\ 0 \end{bmatrix}, \begin{bmatrix} 0 \\ \mathbf{z}_1 \\ 0 \\ 0 \\ 0 \end{bmatrix}, \begin{bmatrix} 0 \\ 0 \\ \mathbf{z}_1 \\ 0 \\ 0 \end{bmatrix}, \begin{bmatrix} A_2^2 \mathbf{z}_2 \\ A_1^1 \mathbf{z}_3 - \dfrac{3c_1 A_3^1 (A_2^2)^2}{c_2} \mathbf{z}_5 \\ 0 \\ \dfrac{3A_3^1 A_2^2}{c_2} \mathbf{z}_5 \\ 0 \end{bmatrix}, \begin{bmatrix} 0 \\ 0 \\ 0 \\ \mathbf{z}_4 \\ 0 \end{bmatrix} \in \mathbb{R}^{45\times 1} . \tag{3.25}$$

Except in the case of constant director field examined earlier, the null space (not counting rigid body modes) of the under-integrated stiffness of 9-node cylindrical elements with director field satisfying the symmetry conditions (3.18) has dimension five (down from seven for the bi-unit square element), based on numerical solution of the related eigenvalue problem. In the present case, this null space is therefore spanned by the five spurious modes in (3.25).

From the matrix representation of spurious modes of the above particular cases of distorted element, in particular positions relative to the (global) basis vectors $\{\mathbf{E}_1, \mathbf{E}_2, \mathbf{E}_3\}$, one can see that these spurious modes have at least a component that is not *simultaneously* orthogonal to the matrices $\mathbf{z}_1$, $\mathbf{z}_2$, $\mathbf{z}_3$, and $\mathbf{z}_4$. This property remains true for a large class of 9-node shell elements. It suffices therefore to construct a filtering scheme that, in addition to $\mathbf{z}_1$, is based on $\mathbf{z}_2$, $\mathbf{z}_3$, and $\mathbf{z}_4$ to eliminate all spurious zero-energy modes of under-integrated 9-node shell elements, in both static and dynamic analyses. Before reaching this stage, we still have to consider the case where an element is placed arbitrarily in the ambient space $\mathbb{R}^3$, since the filtering scheme — which will be constructed using the *fixed* matrices $\mathbf{z}_1$, $\mathbf{z}_2$, $\mathbf{z}_3$, and $\mathbf{z}_4$, and directly in the global coordinates — should remain valid in this general situation as well.

3.2.3. Matrix representation of spurious modes under rigid transformation of the element. Rigid transformation of an element can also be thought of as part of the process of distortion of a bi-unit square element mentioned above. Basically, the matrix representation of displacement spurious modes of the rigidly transformed element are made up of linear combinations of components from the matrix representation

of the original element — except for those modes whose matrix representation is invariant with respect to element shape and orientation.

Consider an arbitrary under-integrated shell element with zero-energy mode $\{\hat{u}_I^{\{i\}} \mid \hat{\chi}_I^{\{\alpha\}}\}$. It suffices to study only rigid rotation, since nothing changes under rigid translation. Let $\mathbf{R} = R_J^I \mathbf{E}_I \otimes \mathbf{E}^J \in SO(3)$ be a rotation tensor with an orthogonal matrix of components $[R_j^i]$. Under this rotation, the vectors $\mathbf{A}_i$ and $\mathbf{T}_i$ are transformed into

$$\mathbf{A}_i^+ = \mathbf{R}\mathbf{A}_i \ , \quad \mathbf{T}_i^+ = \mathbf{R}\mathbf{T}_i \ , \quad \text{and} \quad \mathbf{A}_i^+ \bullet \mathbf{T}_j^+ = \mathbf{A}_i \bullet \mathbf{T}_j \ . \tag{3.26}$$

It follows that the matrices $\mathbf{B}_{rot}^{\alpha}$, which depends only on $\mathbf{A}_i \bullet \mathbf{T}_j$, remain the same for the rotated element, and therefore the rotation components of spurious mode also remain the same: $\hat{\chi}_I^{\alpha+} \equiv \hat{\chi}_I^{\alpha}$. On the other hand, the matrices $\mathbf{B}_{dis}^{i}$ change with the vectors $\mathbf{A}_i$, and consequently their null space. Thus we can consider the strains Γ_{pq} as functions bilinear in the Jacobian $\{A_k^i\}$ and in the displacement $\{u_I^j\}$, and write $\Gamma_{pq}(\{A_k^i\}, \{u_I^j\})$. We have $\Gamma_{pq}(\{A_k^i\}, \{\hat{u}_I^j\}) \equiv 0$ at the reduced-integration points. Hence, for the rotated element, the strain $\mathbf{\Gamma}^+ = \Gamma_{ij}^+ \mathbf{A}^{i+} \otimes \mathbf{A}^{j+}$ has components computed by

$$\Gamma_{ij}^+ = R_i^p R_j^q \Gamma_{pq}(\{A_k^i\}, \{\hat{u}_I^j\}) = \Gamma_{pq}(\{R_i^p A_k^i\}, \{R_j^q \hat{u}_I^j\}) = \Gamma_{pq}(\{A_k^{i+}\}, \{\hat{u}_I^{j+}\}) \equiv 0 \ , \tag{3.27}$$

where we made use of the bilinearity of Γ_{pq}. For the rotated element, the matrix representation of spurious modes that are not invariant has their displacement components $\{\hat{u}_I^i\}$ changed to $\{R_j^i \hat{u}_I^j\}$, i.e., a linear combination of $\{\hat{u}_I^j\}$, $j = 1,2,3$.

Thus, the properties obtained for the un-rotated elements in the previous section still hold for the rotated element. In particular, the matrix representation of a spurious mode of a general 9-node shell element has at least a component that is not simultaneously orthogonal to the matrices $\mathbf{z}_1$, $\mathbf{z}_2$, $\mathbf{z}_3$ and $\mathbf{z}_4$. This is a crucial point that will be exploited next to construct a simple, efficient, and reliable perturbed stiffness matrix for the 9-node shell element.

3.3. Perturbed stiffness matrix for filtering of spurious modes. The perturbation matrix is required to produce no additional strains under displacements that are

linear (for curved elements) or quadratic (for flat elements) functions in the coordinates. Based on results obtained in the previous section, it suffices to use the *fixed* matrix representation of spurious modes $\mathbf{z}_1$, $\mathbf{z}_2$, $\mathbf{z}_3$, and $\mathbf{z}_4$ to construct a perturbation stiffness submatrix of size 9×9, which will be used for *each* of the five dof's u^i, $i = 1,2,3$, and χ^α, $\alpha = 1,2$. We emphasize that the *same* perturbation submatrix is used for all five dof's. The present perturbation matrix is a direct extension of the one given in Vu-Quoc & Mora [1987], which uses only the hourglass mode $\mathbf{z}_1$. The present perturbation matrix possesses the same advantages as the old one: (i) it is constructed directly in global coordinates, thus avoiding unnecessary local-global transformations, and (ii) the 9-node shell element can pass several higher-order (static) patch tests. But most importantly, the proposed perturbation is part of a methodology permitting a complete filtering of spurious modes in dynamic analyses.

We consider the type of *diagonal* perturbation where the stiffness sub-matrix corresponding to each of the five dof's are perturbed independently,

$$\mathbf{K}^{e*} = \widetilde{\mathbf{K}}^{\,e} + \delta\mathbf{K}^e\,, \quad \delta\mathbf{K}^e := \max_{i=1,\ldots,n^e} |\widetilde{K}^{\,e}_{(ii)}| \underset{\substack{i\in\{1,2,3\}\\ \alpha\in\{1,2\}}}{A} \left[\epsilon_{die}\delta\mathbf{K}^i_{die} \oplus \epsilon_{\mathrm{rot}}\delta\mathbf{K}^\alpha_{rot}\right], \ddagger \quad (3.28)$$

but in exactly the same manner in the sense that the normalized perturbation matrices $\delta\mathbf{K}^i_{die}$, $\delta\mathbf{K}^\alpha_{rot} \in \mathbb{R}^{9\times 9}$ are chosen to be identical. Therefore, we only need to construct a perturbation sub-matrix only once for all five dof's. In (3.28), the perturbation factors ϵ_{die} and ϵ_{rot} are in general chosen in the order of 10^{-6}.

Remark 3.3. If the element dof's are ordered with all displacement dof's first, followed by the rotation dof's, as in $\{u_1^{\{i\}}, \ldots, u_{N^e}^{\{i\}} \mid \chi_1^{\{\alpha\}}, \ldots, \chi_{N^e}^{\{\alpha\}}\}$, then the perturbation matrix is in block diagonal form, i.e.,

$$\delta\mathbf{K}^e = \max_{i=1,\ldots,n^e} |\widetilde{K}^{\,e}_{(ii)}|\ Diag\left[\epsilon_{die}\delta\mathbf{K}^1_{die}, \epsilon_{die}\delta\mathbf{K}^2_{die}, \epsilon_{die}\delta\mathbf{K}^3_{die}, \epsilon_{rot}\delta\mathbf{K}^1_{rot}, \epsilon_{rot}\delta\mathbf{K}^2_{rot}\right]. \quad (3.29)$$

‡ $\widetilde{K}_{(ii)}$ is the (i,i) coefficient of the under-integrated element stiffness matrix $\widetilde{\mathbf{K}}^{\,e}$.

□

Consider the following vectors

$$\bar{\mathbf{b}}_i = \{\, \bar{b}_{iI} \,\} := \alpha_{0i}\mathbf{z}_i + \sum_{j=1}^{m} \alpha_{ij}\mathbf{w}_j \in \mathbb{R}^{\vartheta}, \quad \text{for } i = 1,2,3, \tag{3.30a}$$

where the coefficients α_{ij} are to be computed such that

$$\bar{\mathbf{b}}_i \bullet \mathbf{z}_i = k_i \neq 0, \quad \text{and } \bar{\mathbf{b}}_i \bullet \mathbf{w}_j = 0, \quad \forall \quad j = 1,\ldots,m \;.\dagger \tag{3.30b}$$

The coefficients of vectors $\{\mathbf{w}_1, \ldots, \mathbf{w}_m\}$ are polynomials which are linear in the coordinates of element nodal points for curved elements, and quadratic for flat elements. Details of the set-up of vectors $\mathbf{w}_j$ as summarized in the Appendix and the computation of the coefficients α_{ij} follows identically the procedure discussed in Vu-Quoc & Mora [1987]. We consider here a perturbation matrix of the form

$$\delta\mathbf{K}^{i}_{dis} \equiv \delta\mathbf{K}^{\alpha}_{rot} = \frac{[\bar{\mathbf{b}}_1, \bar{\mathbf{b}}_2, \bar{\mathbf{b}}_3][\bar{\mathbf{b}}_1, \bar{\mathbf{b}}_2, \bar{\mathbf{b}}_3]^{\mathrm{T}}}{\max\limits_{I=1,\ldots,\vartheta}[(\bar{b}_{1I})^2 + (\bar{b}_{2I})^2 + (\bar{b}_{3I})^2]} \in \mathbb{R}^{\vartheta\times\vartheta}, \tag{3.31}$$

where, due to the normalizing factor, the coefficients on the diagonal of $\delta\mathbf{K}^{i}_{dis}$ or $\delta\mathbf{K}^{\alpha}_{rot}$ have maximum value equal to one. It can be seen that when only $\bar{\mathbf{b}}_1$ is used the perturbation matrix in (3.31) reduces exactly to the one employed in Vu-Quoc & Mora [1987].

Remark 3.4. The efficiency of the present perturbation matrix in (3.31) lies in its direct construction in *global* coordinate system, i.e., a direct perturbation of the stiffness matrix in global coordinates. This perturbation matrix is constructed, not at each integration point, but only once for each element. In addition, the same perturbation matrix is employed for all dof's. Belytschko and co-workers [1984,1985] employed a diagonal perturbation in local coordinate systems, which further required local-global transformations of the perturbed stiffness. □

† Note that since $\mathbf{z}_4 = \mathbf{r} - 3\mathbf{z}_1$ and $\bar{\mathbf{b}}_i \bullet \mathbf{z}_1 \neq 0$, and $\bar{\mathbf{b}}_i \bullet \mathbf{r} = 0$, it follows that $\bar{\mathbf{b}}_i \bullet \mathbf{z}_4 \neq 0$. We need to use only $\{\mathbf{z}_1, \mathbf{z}_2, \mathbf{z}_3\}$ in (3.30).

3.4. Patch tests. The proposed 9-node shell element, either with the old perturbation stiffness based on only on the mode $\mathbf{z}_1$, or with the present perturbation stiffness based on the modes $\{\mathbf{z}_1, \mathbf{z}_2, \mathbf{z}_3\}$, passes several patch tests that include higher-order ones, such as bending and twisting of a square patch of elements. The patch tests employed here are the same as those proposed in Huang & Hinton [1986] for their 9-node shell element formulated using the so-called assumed-strain method. Under these tests, a patch of elements is subjected to several states of stress: stretching, (in-plane and out-of-plane) shearing, pure bending, and (Mindlin-Reissner and Kirchhoff-Love) twisting. The two types of test containing displacement fields that are quadratic in the coordinates are the bending test and the twisting test. The reader is referred to Taylor *et al* [1986] for discussions on higher-order patch tests. We will comment only on the twisting tests — all other patch tests are passed exactly.‡

Following Huang & Hinton [1986], a five-element patch shown in Figure 3.3a§ is employed to discretize a square plate of side length $L = 10$, lying in the plane $\{\mathbf{E}_1, \mathbf{E}_2\}$. All local triads are assumed to coincide with the global basis vectors, i.e., $\mathbf{T}_i \equiv \mathbf{E}_i$, for $i = 1,2,3$. We consider the range of thickness varying between $h = 0.0001$ and $h = 1$. The material properties chosen are Young's modulus $E = 2.1\times 10^6$, and Poisson's ratio $\nu = 0.3$. In setting up the perturbation matrix, we use $k_1 = k_2 = k_3 = 1$ in (3.30b) and $\epsilon_{dis} = \epsilon_{rot} = 10^{-6}$ in (3.28). For both types of twisting test, the transverse displacement at three corners of the plate are restrained,

$$u^3(L\,,\,0) = u^3(0,\,0) = u^3(0,\,L\,) = 0\,. \tag{3.32}$$

Twisting of a Reissner-Mindlin plate. In addition to the above boundary conditions, the following rotation dof's are restrained: $\chi^2(X^1, 0) = 0$, and $\chi^1(0, X^2) = 0$ for $X^1, X^2 \in [0, L]$. A distributed couple is applied along the two remaining free edges:

‡ Up to seven significant digits are considered in all numerical results in the present paper.
§ The 9-node elements here are quadrilaterals with mid-side nodes exactly in the middle of each side, and with interior nodes on the intersection of lines passing through mid-side nodes.

$\mathbf{M}(L, X^2) = M/L\,\mathbf{E}_1$, and $\mathbf{M}(X^1, L) = -M/L\,\mathbf{E}_2$ (see Figure 3.3b).† The exact expression for the transverse displacement u^3 using Reissner-Mindlin theory is given by

$$u^3 = \frac{12(1+\nu)}{Eh^3}\,\frac{M}{L}\,X^1X^2\,. \tag{3.33}$$

The present 9-node element passes perfectly this test for a large range of thickness (see table 3.1). Clearly, the passing of this test is due to the orthogonality (3.30b) where the vectors $\mathbf{w}_j$ contain polynomials quadratic in the coordinates.

Twisting of a Kirchhoff-Love plate. A force $P\mathbf{E}_3$ is applied at the free corner — the other three corners are restrained according to (3.32), see Figure (3.3c). Similar to (3.33), the exact expression of the transverse displacement u^3 using Kirchhoff-Love theory,

$$u^3 = \frac{6(1+\nu)}{Eh^3}\,P\,X^1X^2\,, \tag{3.34}$$

contains the quadratic term X^1X^2. From Table 3.1, one observes a very small error in the results: The percentage error in the transverse deflection under the load with respect to the exact value decreases, however, with the thickness. Even though the formulation is not based on the Kirchhoff-Love theory and therefore numerical error is to be expected, yet the element performs well under this test.

Table 3.1. *Twisting of a square plate ($L = 10$). Percentage error of tip deflection versus thickness.*

Thickness h	Reissner-Mindlin Percentage error	Kirchhoff-Love Percentage error
1.0	0.	14.31
0.1	0.	1.21
0.01	0.	0.92
0.001	0.	0.40
0.0001	-0.0001	0.01

† The nodal values of these distributed moments as given in Figure 3.3b for a one-element patch are the same for the five-element patch in Figure 3.3a.

In summary, the present 9-node shell element, with a reduced-integrated stiffness and its consistent perturbation as given in (3.31), can reproduce every possible states of constant strain, as well as the state of pure bending and constant twisting of the (Reissner-Mindlin) plate, for a wide range of thickness. On the other hand, as the thickness decreases, this element reproduces results under twisting that approach those predicted by the Kirchhoff-Love theory for thin plates.

4. Dynamic analysis using under-integrated shell elements

While the filtering of spurious modes via a judicious perturbation of the stiffness matrix as proposed in the previous section provides good results in static analyses, it is insufficient to avoid spurious modes in dynamic analyses using under-integrated shell elements. The reason for this difficulty is immediate because spurious modes, having significant (generalized) masses, are associated with artificially low energy that is introduced in the perturbation procedure. Hence by virtue of the Rayleigh quotient corresponding to a (global) spurious mode $\mathbf{z}$,

$$\frac{\mathbf{z}^{\mathrm{T}}\,\mathbf{K}^{*}\,\mathbf{z}}{\mathbf{z}^{\mathrm{T}}\,\mathbf{M}\,\mathbf{z}} = \frac{\mathbf{z}^{\mathrm{T}}\,\delta\mathbf{K}\,\mathbf{z}}{\mathbf{z}^{\mathrm{T}}\,\mathbf{M}\,\mathbf{z}}\,, \tag{4.1}$$

where $\mathbf{K}^{*} = \widetilde{\mathbf{K}} + \delta\mathbf{K}$ is the perturbed under-integrated stiffness (recall that $\widetilde{\mathbf{K}}\,\mathbf{z} = 0$), and $\mathbf{M}$ the (positive definite) mass matrix, one can clearly see that spurious modes can appear as very low-frequency modes, and can effectively pollute the computed dynamic response. For a fixed mesh topology of a given structure, the eigen-frequencies of spurious modes increase as the element size decreases. This is because the pattern of spurious modes is repeated in each element of the mesh, and as the number of elements increases, so is the number of repeated patterns of element spurious modes. Exactly how spurious eigen-frequencies change with element size depends, however, on how the element stiffness was perturbed. Examples of spurious dynamics in shell structures will be given later in the examples section.

We propose in this section a projection method for the mass matrix, which effectively constitutes the second stage of the proposed perturbation approach for dynamic analysis using under-integrated shell elements — the first stage being the perturbation of the under-integrated stiffness matrix. Emphasis will be focused on the more difficult case of the 9-node shell elements, with some remarks on the much easier case of the 4-node shell elements. Related issues concerning transient dynamic analysis with the present perturbation method will also be discussed.

4.1. Equivalence with modal step-by-step integration. We recall here a well-known result, which constitutes a starting point for our proposed approach. Consider the semi-discrete equations of motion (for a linear problem)

$$\mathbf{M}\ddot{\mathbf{d}} + \mathbf{C}\dot{\mathbf{d}} + \mathbf{K}\mathbf{d} = \mathbf{F}(t) , \tag{4.2}$$

where $\mathbf{M} \in \mathbb{R}^{n\times n}$ is the positive definite (consistent or lumped) mass matrix of the structure, $\mathbf{C} \in \mathbb{R}^{n\times n}$ the damping matrix, $\mathbf{K} \in \mathbb{R}^{n\times n}$ the stiffness matrix, $\mathbf{d} \in \mathbb{R}^n$ the vector containing all system dof's, and $\mathbf{F} \in \mathbb{R}^n$ the forcing-function vector. Then assuming that the damping matrix is diagonalizable via modal decomposition — for instance, using the extended Caughey series $\mathbf{C} = \mathbf{M}\sum_{i=0}^{n-1} a_i(\mathbf{M}^{-1}\mathbf{K})^i$ as discussed in Wilson & Penzien [1972] — then the system (4.2) can be decomposed into an equivalent system of uncoupled scalar differential equations:

$$[\mathbf{K} - \omega_i^2\mathbf{M}]\boldsymbol{\phi}_i = 0 , \quad \boldsymbol{\phi}_i^{\mathrm{T}}\mathbf{M}\boldsymbol{\phi}_j = \delta_{ij} , \quad \mathbf{d}(t) = \sum_{i=1}^{n}\psi_i(t)\boldsymbol{\phi}_i , \tag{4.3a}$$

$$\ddot{\psi}_i + c_i\dot{\psi}_i + \omega_i^2\psi_i = \boldsymbol{\phi}_i^{\mathrm{T}}\mathbf{F}(t) , \quad \text{for } i = 1,\ldots,n , \tag{4.3b}$$

$$\text{where} \quad c_i = \boldsymbol{\phi}_i^{\mathrm{T}}\mathbf{C}\boldsymbol{\phi}_i , \quad \omega_i^2 = \boldsymbol{\phi}_i^{\mathrm{T}}\mathbf{K}\boldsymbol{\phi}_i . \tag{4.3c}$$

In addition, the time discretization of the coupled system (4.2) and of the un-coupled system (4.3) using the Newmark (implicit) method are entirely equivalent, leading to a commutative diagram as presented in Hughes [1983]. We refer to this reference for detailed discussions on the above equivalence.

Even though it is sufficient to require that the (fully-integrated) stiffness $\mathbf{K}$ in (4.2) and in (4.3) be positive semi-definite, to simplify the discussions that follow, we assume in addition that the stiffness $\mathbf{K}$ is positive definite, i.e., the structure does not admit rigid-body motions. Accordingly, the frequencies ω_i in (4.3) are strictly positive. Then, it can be clearly seen that problems will arise when one attempts to replace the fully-integrated $\mathbf{K}$ in (4.2) with the under-integrated $\widetilde{\mathbf{K}}$, which is positive semi-definite, to remove shear/membrane locking: The response, depending on initial conditions and the loading, could be polluted by zero-energy modes, which are not rigid-body modes, but spurious modes. Moreover, unlike in static problems, this undesirable effect does not disappear when we employ the perturbed stiffness $\mathbf{K}^*$ in the place of $\mathbf{K}$. The reason is that, as stated earlier, spurious modes can appear arbitrarily at low frequency depending on the finite-element mesh. Such problem would be solved if we could move these spurious modes to the high frequency end of the eigen-spectrum — or better yet, to completely filter spurious dynamics from the response — by considering an appropriate perturbation of system (4.2). Of course, this operation should not affect the accuracy of the genuine mode shapes.

4.2. Projection method for filtering of spurious dynamics. Consider a perturbed system (4.2), with $(\mathbf{M}^*, \mathbf{C}^*, \mathbf{K}^*)$, with zero generalized masses for the spurious modes. Eigen-frequencies of the spurious modes are thus pushed to infinity, so to speak. Let the eigenvectors $\boldsymbol{\phi}_i$ be reordered such that the first m modes, $\{\boldsymbol{\phi}_1, \ldots, \boldsymbol{\phi}_m\}$, are significant to participate in the dynamic response, while the remaining $(n-m)$ modes, $\{\boldsymbol{\phi}_{m+1}, \ldots, \boldsymbol{\phi}_n\}$, are spurious zero-energy modes.† That is, $\widetilde{\mathbf{K}}\,\boldsymbol{\phi}_i = 0$, and $\mathbf{M}^*\boldsymbol{\phi}_i = 0$, for $i = m+1,\ldots,n$. Equations (4.3b) then becomes

$$\ddot{\psi}_i + c_i\dot{\psi}_i + \omega_i^2\psi_i = \boldsymbol{\phi}_i^T\mathbf{F}(t)\,, \quad \text{for } i = 1,\ldots,m\,, \tag{4.4a}$$

$$c_i\dot{\psi}_i + \omega_i^2\psi_i = \boldsymbol{\phi}_i^T\mathbf{F}(t)\,, \quad \text{for } i = m+1,\ldots,n\,, \tag{4.4b}$$

† This ordering is not in increasing magnitude of the eigen-frequencies.

where now $c_i = \boldsymbol{\phi}_i^T \mathbf{C}^* \boldsymbol{\phi}_i$, and $\omega_i^2 = \boldsymbol{\phi}_i^T \mathbf{K}^* \boldsymbol{\phi}_i$. Note, however, that while $\{\omega_1, \ldots, \omega_m\}$ are eigen-frequencies of the eigenvalue problem $[\mathbf{K}^* - \omega_i^2 \mathbf{M}^*]\boldsymbol{\phi}_i = 0$, the remaining values

$$\omega_i^2 = \boldsymbol{\phi}_i^T \mathbf{K}^* \boldsymbol{\phi}_i = \boldsymbol{\phi}_i^T \delta\mathbf{K} \boldsymbol{\phi}_i = O(\epsilon \max_{j=1,\ldots,n} |\widetilde{K}_{(jj)}|), \quad \text{for } i = m+1, \ldots, n, \tag{4.4c}$$

are not (see (3.28)). For a rapid decay of spurious dynamics, from initial conditions $\psi_i(0)$, for $i = m+1, \ldots, n$, it suffices to choose the corresponding damping coefficients c_i such that the ratios ω_i^2/c_i, are large enough. Note that if we set $c_i = 0$, for $i = m+1,\ldots,n$, then $\psi_i = \boldsymbol{\phi}_i^T \mathbf{F}(t)/\omega_i^2$, and thus the amplitude of ψ_i depends on the participation factor of $\mathbf{F}(t)$ with respect to the spurious modes (which is in general small) and on the perturbation factor ϵ through ω_i^2 by (4.4c). To make the integration of system (4.2) stable with any forcing vector $\mathbf{F}$, it is therefore advisable to use non-zero damping coefficients for spurious modes chosen as mentioned.

Remark 4.1. In linear problems where the forcing-function vector $\mathbf{F}(t)$ has low-frequency content with small factors $\boldsymbol{\phi}_i^T \mathbf{F}$ in the high-frequency range, it is more efficient to integrate only a few low-frequency modal equations, instead of integrating the whole system (4.2). In this case, one can select for use the appropriate modes, with *non-zero* frequencies, of the un-perturbed problem $[\widetilde{\mathbf{K}} - \omega^2 \mathbf{M}]\boldsymbol{\phi} = 0$. We note, however, that the perturbed system $(\mathbf{M}^*, \mathbf{K}^*)$ in general yields better eigenvalues and convergence rates with respect to discretization than the un-perturbed system, as will be shown in the examples section. □

4.3. Construction of projected mass matrix $\mathbf{M}^*$ and damping matrix $\mathbf{C}^*$. The method of constructing the matrices $\mathbf{M}^*$ and $\mathbf{C}^*$ discussed here clearly applies to the case where we have to use (implicit) step-by-step integration to solve the semi-discrete equations of motion, which are either linear as in (4.2), or having non-linear internal force in the more general situation.

4.3.1. Global projection using eigenvectors. The projected mass $\mathbf{M}^*$ will be a positive semi-definite matrix whose null space should contain all spurious modes of the

system. Let $\{\boldsymbol{\phi}_1, \ldots, \boldsymbol{\phi}_k\}$, with $k \leq m$, be the chosen (non-spurious) eigenvectors as discussed in Remark 4.1. Then, the required projected mass $\mathbf{M}^*$ can be evaluated as follows

$$\mathbf{M}^* = \sum_{i=1}^{k} (\mathbf{M}\boldsymbol{\phi}_i)(\mathbf{M}\boldsymbol{\phi}_i)^{\mathrm{T}} \in \mathbb{R}^{n\times n} \ . \tag{4.5}$$

Next, once the values of the damping coefficients c_i, for $i = 1,...,n$, are chosen, a diagonalizable damping matrix $\mathbf{C}^*$ can be easily constructed by a direct generalization of (4.5),

$$\mathbf{C}^* = \sum_{i=1}^{n} c_i (\mathbf{M}\boldsymbol{\phi}_i)(\mathbf{M}\boldsymbol{\phi}_i)^{\mathrm{T}} \in \mathbb{R}^{n\times n} \ , \tag{4.6}$$

as proposed in Wilson & Penzien [1972]. Note that in (4.5) and (4.6) one could use the eigenvectors $\boldsymbol{\phi}_i$ of the un-perturbed eigenvalue problem $[\widetilde{\mathbf{K}} - \omega^2\mathbf{M}]\boldsymbol{\phi} = 0$. Also, if needed, the global rigid body modes could be included in the construction of $\mathbf{M}^*$ in (4.5). In practice, the eigenvectors associated with the zero eigenvalue of the problem $[\widetilde{\mathbf{K}} - \omega_i^2\mathbf{M}]\boldsymbol{\phi}_i = 0$ often appear as linear combinations of rigid body modes and spurious modes. A separation of rigid body modes from spurious modes is possible if one consider the eigenvalue problem $[\mathbf{K}^* - \omega^2\mathbf{M}]\boldsymbol{\phi} = 0$; nevertheless, visual selection of spurious modes is not a convenient task. In addition, a recognized disadvantage of this projection method is the fullness of the matrices in (4.5) and (4.6).

One way to retain the bandedness of the mass matrix is to perform the projection similar to (4.5) at the element level. But this approach requires solving an eigenvalue problem $[\widetilde{\mathbf{K}}^e - \omega_i^2\mathbf{M}^e]\boldsymbol{\phi}_i^e = 0$ for each element before the computation of the projected element mass $\mathbf{M}^{e*}$ following (4.5). In the next sub-section, the idea of doing the projection at the element level will be refined to a practical approach that resolves the mentioned shortcomings.

4.3.2. Local projection using spurious modes at element level. By making use of the properties of spurious modes of shell elements as studied in Section 3, we propose — for the filtering of spurious dynamics — an efficient method to construct a

projected mass matrix $\mathbf{M}^{e*}$ and an appropriate damping matrix $\mathbf{C}^{e*}$, and at the element level. The computational advantage here is evident: Unlike in the previous sub-section, one does not need to solve an eigenvalue problem prior to the construction of $\mathbf{M}^*$ and $\mathbf{C}^*$. For the damping matrix, one could simply choose $\mathbf{C}^{e*} = c\,\delta\mathbf{K}^e$, where the constant c has to be chosen with care along the line of the discussions in Section 4.2 for effectiveness in the results. It remains to focus our attention on the projection of the mass matrix.

The proposed construction of the projected element mass matrix $\mathbf{M}^{e*} \in \mathbb{R}^{n^e \times n^e}$ hinges on finding a projection matrix $\mathbf{Q} \in \mathbb{R}^{n^e \times n^e}$ such that

$$\mathbf{M}^{e*} = \mathbf{Q}^{\mathrm{T}}\,\mathbf{M}^e\,\mathbf{Q} =$$

$$\int_{\Omega^e} \underset{\substack{i,j\,\in\,\{1,2,3\}\\ \alpha,\beta\,\in\,\{1,2\}}}{A} \left[\left(\overline{\mathbf{P}}^i_{dis}\right)^{\mathrm{T}} \overline{\mathbf{P}}^j_{dis} \oplus \left(\overline{\mathbf{P}}^\alpha_{rot}\right)^{\mathrm{T}} \overline{\mathbf{P}}^\beta_{rot} \oplus \left(\overline{\mathbf{P}}^i_{dis}\right)^{\mathrm{T}} \overline{\mathbf{P}}^\beta_{rot} \oplus \left(\overline{\mathbf{P}}^\alpha_{rot}\right)^{\mathrm{T}} \overline{\mathbf{P}}^j_{dis} \right] \mathrm{d}\Omega \in \mathbb{R}^{n^e \times n^e} \quad (4.7a)$$

where

$$\overline{\mathbf{P}}^i_{dis} := \mathbf{P}^i_{dis}\mathbf{Q}^i_{dis} \in \mathbb{R}^{3\times N^e}\,, \quad \overline{\mathbf{P}}^\alpha_{rot} := \mathbf{P}^\alpha_{rot}\mathbf{Q}^\alpha_{rot} \in \mathbb{R}^{3\times N^e}\,, \qquad (4.7b)$$

and $\mathbf{Q}^i_{dis} \in \mathbb{R}^{N^e\times N^e}$, and $\mathbf{Q}^\alpha_{rot} \in \mathbb{R}^{N^e\times N^e}$ are sub-matrices of $\mathbf{Q}$. Based on the results in Section 3, since spurious modes have matrix representation with components not simultaneously orthogonal to $\mathbf{z}_j$, for $j = 1,...,4$, we consider enforcing the following conditions

$$\mathbf{Q}^i_{dis}\mathbf{r} = \mathbf{r}\,, \quad \text{and} \quad \mathbf{Q}^i_{dis}\mathbf{z}_1 = \mathbf{Q}^\alpha_{rot}\mathbf{z}_1 = 0\,, \qquad (4.8a)$$

for the 4-node shell element, and

$$\mathbf{Q}^i_{dis}\mathbf{r} = \mathbf{r}\,, \quad \text{and} \quad \mathbf{Q}^i_{dis}\mathbf{z}_j = \mathbf{Q}^\alpha_{rot}\mathbf{z}_j = 0\,, \quad j \in \{1,2,3,4\}\,, \qquad (4.8b)$$

for the 9-node shell element. Thus, spurious modes whose components are linear combinations of the vectors $\mathbf{z}_j$ will have zero generalized masses, and furthermore, the total mass of an element will be preserved in rigid body modes:

$$\mathbf{z}^{\mathrm{T}}\mathbf{M}^{e*}\mathbf{z} = 0\,, \quad \mathbf{r}^{\mathrm{T}}\mathbf{M}^{e*}\mathbf{r} \equiv \mathbf{r}^{\mathrm{T}}\mathbf{M}^e\mathbf{r}\,. \qquad (4.9)$$

Remark 4.2. In (4.7a), suppose $\mathbf{M}^e$ is fully integrated, and therefore is a positive definite matrix. The projected mass matrix $\mathbf{M}^{e*}$ is on the other hand a positive semi-definite matrix. □

For the 9-node element, it is impossible, however, to enforce totally conditions (4.8b) for $\mathbf{z}_4 = \mathbf{r} - 3\mathbf{z}_1$ is a linear combination of $\mathbf{r}$ and $\mathbf{z}_1$. One of the two conditions, $\mathbf{Q}^i_{die}\mathbf{z}_1 = 0$ or $\mathbf{Q}^i_{die}\mathbf{z}_4 = 0$, will have to be relaxed. In fact, as will be seen shortly, the relaxation of conditions (4.8b) is possible in the sense that it is not necessary to force the generalized masses of all spurious modes to zero. It suffices to project certain mode in a way — to be precisely explained below — that it cannot possibly appear as an eigenvector of the perturbed problem $[\mathbf{K}^* - \omega_i^2\mathbf{M}^*]\boldsymbol{\phi}_i = 0$. Also, it should be noted that the generalized mass of a spurious mode whose matrix representation depends on element distortion is not exactly zero, but reduced, since through the projection we have eliminated the contribution to the generalized mass coming from the vectors $\mathbf{z}_j$.

Remark 4.3. If the element dof's are ordered as stated in Remark 3.3, then the projection matrix $\mathbf{Q}$ will have a block diagonal form

$$\mathbf{Q} = \mathit{Diag}\ [\ \mathbf{Q}^1_{die},\ \mathbf{Q}^2_{die},\ \mathbf{Q}^3_{die},\ \mathbf{Q}^1_{rot},\ \mathbf{Q}^2_{rot}\ ] \in \mathbb{R}^{n^e \times n^e}\ , \tag{4.10}$$

similar to the perturbation matrix $\delta\mathbf{K}^e$ in (3.29), but the projection of the mass matrix as proposed in (4.7) does not parallel, in terms of matrix operations, the diagonal perturbation of the stiffness matrix as given in (3.28). □

As a consequence of the analysis in Section 3.2.3, it would be computationally very efficient if we could construct only one projection sub-matrix of $\mathbf{Q}$, and use it for all five dof's, i.e.,

$$\mathbf{Q}^i_{die} \equiv \mathbf{Q}^\alpha_{rot} \equiv \mathbf{Q}_{dr} \in \mathbb{R}^{N^e \times N^e}\ . \tag{4.11}$$

Construction of projection matrix $\mathbf{Q}_{dr}$. For the 4-node shell element (not necessarily a flat one), only the matrix representation $\mathbf{z}_1$ as defined in $(2.7)_1$ needs be considered. Whereas for the 9-node shell element, we have to account for all matrix

representations of spurious mode $\{\mathbf{z}_1, \mathbf{z}_2, \mathbf{z}_3, \mathbf{z}_4\}$. Consider the following expression for $\mathbf{Q}_{dr}$

$$\mathbf{Q}_{dr} = \begin{bmatrix} \hat{\mathbf{q}}_1^{\mathrm{T}} \\ \cdot \\ \cdot \\ \hat{\mathbf{q}}_{N^e}^{\mathrm{T}} \end{bmatrix} \in \mathbb{R}^{N^e \times N^e}, \quad \text{with } \hat{\mathbf{q}}_{\mathrm{I}} := \mathbf{q}_{\mathrm{I}} - \sum_{\mathrm{J}=1}^{\kappa} \beta_{\mathrm{IJ}} \mathbf{b}_{\mathrm{J}}, \tag{4.12a}$$

where the vectors $\mathbf{q}_{\mathrm{I}}$ are the standard unit basis vectors in $\mathbb{R}^{N^e}$,

$$\mathbf{q}_{\mathrm{I}} := \{ \delta_{\mathrm{IJ}} \} = \{ 0,...,1,...,0 \}^{\mathrm{T}} \in \mathbb{R}^{N^e}, \dagger \tag{4.12b}$$

κ the number of spurious modes accounted for in the projection, and $\{\mathbf{b}_1, \ldots, \mathbf{b}_\kappa\}$ a set of independent vectors in $\mathbb{R}^{N^e}$ to be determined shortly. The coefficients β_{IJ} are to be found so that the conditions in (4.8) hold.

Even though, in principle, the independent set of vectors $\{\mathbf{b}_{\mathrm{I}}\}$ appearing in (4.12) could be chosen arbitrarily, it is numerically more efficient to choose $\mathbf{b}_{\mathrm{I}}$ to be the same as the vectors appearing in conditions (4.8). Thus, for $\mathbf{b}_1 = \mathbf{r}$ and $\mathbf{b}_2 = \mathbf{z}_1$, we have

$$\hat{\mathbf{q}}_{\mathrm{I}} = \mathbf{q}_{\mathrm{I}} - \left(\frac{z_{1\mathrm{I}}}{\mathbf{z}_1 \bullet \mathbf{z}_1} \right) \mathbf{z}_1 \in \mathbb{R}^{N^e}, \tag{4.13}$$

which for the 4-node shell element ($N^e = 4$) clearly satisfies the conditions in (4.8a).‡ For a 9-node shell element, the projection (4.13) is clearly insufficient, and a decision is to be made regarding the choice of the set $\{\mathbf{b}_{\mathrm{I}}\}$ as one of the following two sets of independent vectors in $\mathbb{R}^9$: $\{\mathbf{r}, \mathbf{z}_1, \mathbf{z}_2, \mathbf{z}_3\}$ and $\{\mathbf{r}, \mathbf{z}_2, \mathbf{z}_3, \mathbf{z}_4\}$. The first set contains orthogonal vectors, whereas the second set is only partially orthogonal — see Remark 3.2. As noted earlier, $\mathbf{z}_1$ and $\mathbf{z}_4$ are mutually exclusive by conditions (4.8b), i.e., they cannot appear together (with $\mathbf{r}$) in the same set. For the discussion that follows, it is good to keep in mind the case of a square plate with free boundary conditions, and the results of Section 3.1.§

† Recall that δ_{IJ} stands for the Kronecker delta.

‡ Recall that the vector $\mathbf{r}$ is orthogonal to the mode $\mathbf{z}_1$ for both $N^e = 4$ and $N^e = 9$. Also $z_{1\mathrm{I}}$ is the Ith coefficient of the vector $\mathbf{z}_1$.

§ Numerical results of eigenvalue analysis for a square plate with free boundary conditions will be given later in the examples section.

First, we look at the relaxation of conditions (4.8b): specifically, whether to retain $\mathbf{Q}_{dr}\,\mathbf{z}_1 = 0$ or $\mathbf{Q}_{dr}\,\mathbf{z}_4 = 0$. If we opt to retain the condition $\mathbf{Q}_{dr}\,\mathbf{z}_1 = 0$ and work with the first set of orthogonal vectors $\{\mathbf{r},\, \mathbf{z}_1,\, \mathbf{z}_2,\, \mathbf{z}_3\}$, then

$$\hat{\mathbf{q}}_I = \mathbf{q}_I - \frac{z_{1I}}{9}\,\mathbf{z}_1 - \frac{2z_{2I}}{9}\,\mathbf{z}_2 - \frac{2z_{3I}}{9}\,\mathbf{z}_3 \in \mathbb{R}^9\,,\dagger \tag{4.14}$$

for I = 1,...,9. Since $\mathbf{Q}_{dr}\mathbf{r} = \mathbf{r}$ and $\mathbf{z}_4 = \mathbf{r} - 3\mathbf{z}_1$, it follows that $\mathbf{Q}_{dr}\mathbf{z}_4 = \mathbf{r} \neq 0$. As a result, the generalized mass corresponding to the spurious rotation mode $\mathbf{z}_4$ is not zero. Further, having non-zero generalized stiffness by perturbation of the under-integrated stiffness $\widetilde{\mathbf{K}}$ as done in (3.28), this rotation mode may appear in the low-frequency eigenvectors (more so for a moderately thick shell than for a thin one; an example will be given where these spurious rotation modes appear at the very beginning of the eigenspectrum). Thus, apart from the modes $\mathbf{z}_2$ and $\mathbf{z}_3$, while we can filter the mode $\mathbf{z}_1$ with the above choice, we fail at filtering the mode $\mathbf{z}_4$.

Remark 4.4. Using either the projection in (4.13) or (4.14) for the mass matrix of a square plate (see Example 5.1), the *displacement* "bat" mode as depicted in Figure 5.2, in addition to the spurious rotation modes, cannot be filtered out. The persistence of the "bat" mode is due to its matrix representations, given in (5.1), which have non-zero components along the vectors $\{\mathbf{r},\, \mathbf{z}_1,\, \mathbf{z}_2,\, \mathbf{z}_3,\, \mathbf{z}_4\}$. □

Next, we will show that retaining the condition $\mathbf{Q}_{dr}\,\mathbf{z}_4 = 0$ and working with the second set of vectors $\{\mathbf{r},\, \mathbf{z}_2,\, \mathbf{z}_3,\, \mathbf{z}_4\}$ achieves a complete filtering of both modes $\mathbf{z}_1$ and $\mathbf{z}_4$. Instead of (4.14), we now have

$$\hat{\mathbf{q}}_I = \mathbf{q}_I + \frac{z_{4I}}{72}\,\mathbf{r} - \frac{2z_{2I}}{9}\,\mathbf{z}_2 - \frac{2z_{3I}}{9}\,\mathbf{z}_3 - \frac{z_{4I}}{72}\,\mathbf{z}_4 \in \mathbb{R}^9\,, \tag{4.15}$$

for I = 1,...,9. We only need to examine the case of the spurious displacement mode $\mathbf{z}_1$, since the filtering of mode $\mathbf{z}_4$ with the current choice is evident because its generalized

† Recall that z_{jI} is the Ith coefficient of vector $\mathbf{z}_j$.

mass is nullified by the projection. Let $\overset{\mathrm{v}}{\mathbf{z}}_1 \in \mathbb{R}^{n^e}$ denote a vector with zero coefficients except for the displacement component u^i such that $\{u_1^{(i)}\} = \mathbf{z}_1 \in \mathbb{R}^{N^e}$; a similar definition applies to the displacement rigid body mode $\overset{\mathrm{v}}{\mathbf{r}} \in \mathbb{R}^{n^e}$. We can see how the mode $\mathbf{z}_1$ is filtered out by looking at the solution for eigenvalue problem $[\mathbf{K}^{e*} - \omega_i^2 \mathbf{M}^{e*}]\boldsymbol{\phi} = 0$. Since $\mathbf{Q}_{dr}\mathbf{z}_1 = \mathbf{r}/3$, it follows that $\mathbf{M}^{e*}\overset{\mathrm{v}}{\mathbf{z}}_1 \equiv \mathbf{M}^{e*}\overset{\mathrm{v}}{\mathbf{r}}$. Thus, if $\overset{\mathrm{v}}{\mathbf{z}}_1$ is a starting vector for the inverse iteration, it has to converge to a rigid (*displacement*) mode.‡ That is, the spurious displacement mode $\overset{\mathrm{v}}{\mathbf{z}}_1$ cannot appear as an eigenvector. Expression (4.15) therefore constitutes the desired projection matrix $\mathbf{Q}_{dr}$ as given in (4.12a).

Remark 4.5. Consider the subspace orthogonal to the one spanned by $\{\mathbf{r}, \mathbf{z}_1\}$ for $N^e = 4$, or to the one spanned by $\{\mathbf{r}, \mathbf{z}_2, \mathbf{z}_3, \mathbf{z}_4\}$ for $N^e = 9$. The direct sum of this subspace and the rigid body displacement $\mathbf{r}$ forms an invariant subspace with respect to the projection matrix $\mathbf{Q}_{dr}$. □

5. Numerical examples

In this section, several numerical examples are given to assess the performance of the proposed filtering scheme in dynamic analysis using the present 9-node shell element. To this end, it suffices to compare the eigen-spectrum of the unperturbed system $[\widetilde{\mathbf{K}} - \omega_i^2 \mathbf{M}]\boldsymbol{\phi}_i = 0$, where one encounters spurious modes, to the eigen-spectrum of the perturbed system $[\mathbf{K}^* - \omega_i^2 \mathbf{M}^*]\boldsymbol{\phi}_i = 0$,§ where a complete filtering of spurious modes is achieved. Unlike in static analysis, there is no proposed "standard" course of obstacles for dynamic analysis of shells. The reason stems in our interest in the low end of the eigen-spectrum of the free vibration problem where the finite element approximation is most accurate. If a formulation performs well in static analysis, it will do well in dynamic analysis at the low frequency range. The difference between various element

‡ The same is not true with $\mathbf{z}_4$ because while $\mathbf{B}_{dis}^1\mathbf{r} = 0$, we have $\mathbf{B}_{rot}^{\alpha}\mathbf{r} \neq 0$.

§ The projection of the mass matrix is that given in (4.15).

formulations will be more distinctly revealed in the high frequency range.

The effectiveness of our proposed filtering scheme for analysis of general shell structures is illustrated through examples that are particularly chosen where the difficulties encountered with the existence of spurious dynamics are most severe. Of course, these examples must have either analytical or experimental solutions, serving as a norm upon which is measured the accuracy in the numerical results. We will consider the free vibration of a moderately thick square plate and a thin square plate, both with free boundary conditions, a clamped thick circular plate, and a thin cylindrical shell with free ends as well as with rigid diaphragms.

The 9-node Lagrangian shell element with the proposed filtering scheme has been implemented in the research version of FEAP, a Finite Element Analysis Program, developed by R.L. Taylor, and run under the Berkeley Unix 4.3 BSD operating system. The reader is referred to Chapter 24 of Zienkiewicz [1977] for a description of a simplified version of this program. In all examples, element stiffness matrices are under-integrated in the lamina, with three integration points in the thickness direction, and perturbed in the consistent manner discussed in Section 3.3. Throughout all calculation, the perturbation constants in (3.28) are set to $\epsilon_{die} = \epsilon_{rot} = 10^{-6}$, and and the constant k_i in (3.30b) to $k_1 = k_2 = k_3 = 1$.

In addition to results obtained with the projection of the fully-integrated consistent mass matrix (represented by solid lines in the convergence plots of eigen-frequencies), we also present results obtained with the projection of the reduced-integrated consistent mass and the lumped mass matrices (dotted lines in convergence plots of eigen-frequencies). To be established through these numerical results is the superior performance of the use of the projected fully-integrated consistent mass matrix — which will be often referred to shortly as *the* projected mass — over the other two types of projected mass.

5.1. Square plate with free boundary conditions. Since the square plate is similar in both geometry and boundary conditions to the bi-unit square element studied in Section 3, we must be able to observe all possible spurious modes in the eigenvalue problem $[\mathbb{K} - \omega_i^2 \mathbf{M}]\boldsymbol{\phi}_i = 0$. Further, the availability of both analytical and experimental results for many vibrational modes makes it easy to verify the computed results as well as to compare the performance of different types of projected mass matrix. The plate has unit side length ($L = 1$), and lies in the first quadrant of the plane $\{\mathrm{E}_1, \mathrm{E}_2\}$. The local triads are chosen such that $\mathbf{T}_\mathrm{I} \equiv \mathbf{E}_\mathrm{I}$, for I = 1,2,3. Two values of the plate thickness are considered: $h = 0.1$ and $h = 0.001$. The material properties chosen are Young's modulus $E = 1000$, Poisson's ratio $\nu = 0.3$, and mass density $\rho = 0.01$.

Belytschko, Tsay & Liu [1982] used a square plate to establish the order of magnitude of a parameter r characterizing the norm of their perturbation matrix. As this parameter r is increased ($r > 0.03$), the stiffness in the elements increases, and consequently so do the eigen-frequencies. But, by the orthogonality property of the perturbation stiffness matrix $\delta\mathbf{K}$, the eigen-frequencies of the genuine lower modes are only perturbed by a small amount, whereas the eigen-frequencies of the spurious modes increase with r. These authors therefore propose to increase the value of r to remove spurious modes in the low frequency range. But this method requires some trial-and-error runs for general shell structures until spurious modes are pushed out of the bandwidth of the interested low frequencies. In any case, no complete elimination of spurious dynamics can be achieved in this way, and moreover there is a limit to increasing the magnitude of r, lest the stiffness would change significantly.

5.1.1. Moderately thick plate ($h = 0.1$). Both displacement and rotation spurious modes appear at the very beginning of the eigen-spectrum of the un-perturbed problem $[\mathbb{K} - \omega_i^2 \mathbf{M}]\boldsymbol{\phi}_i = 0$, where the projection of the mass matrix is not used. Analysis are made using meshes with 1, 4, and 16 elements. The typical results, using for example the uniform 4-element mesh, are shown in Table 5.1. The *reference* values for the first

Table 5.1. *Moderately thick square plate. Eigen-frequencies using unprojected mass matrix (uniform 4-element mesh).*

Mode	Freq. (rad/s)	Ratio	Description
1	2.6783	—	Spurious transverse (hourglass) mode $\{u_I^3\} = \mathbf{z}_1$ (Figure 5.1a).
2	2.6783	—	Spurious in-plane (hourglass) mode $\{u_I^{\{\alpha\}}\} = \mathbf{z}_1$ (Figure 5.1b).
3	2.6783	—	Spurious in-plane (hourglass) mode $\{u_I^{\{\alpha\}}\} = \mathbf{z}_1$.
4	2.7289	—	Spurious in-plane mode (disp. "bat" mode) (Figure 5.2).
5	92.440	—	Spurious rotation mode $\{\chi_I^1\} = \mathbf{z}_4$.
6	92.440	—	Spurious rotation mode $\{\chi_I^2\} = \mathbf{z}_4$.
7	94.346	—	Spurious rotation mode (rot. "bat" mode).
8	125.13	0.971	First elastic bending mode (Figure 5.3a).
9	188.83	1.007	Second elastic bending mode (Figure 5.4a).
10	238.00	1.025	Third elastic bending mode (Figure 5.5a).

three elastic bending modes are based on the theory of thin plate (Leissa [1969, p.104]): $\omega_1 = 128.93 rad/s$, $\omega_2 = 187.52 rad/s$, and $\omega_3 = 232.25 rad/s$; the ratios of computed frequencies over their reference values are shown in Table 5.1. We note that the displacement and rotation modes with matrix representation $\{\mathbf{z}_2, \mathbf{z}_3\}$ of the one-element (see (3.3)) mesh become the "bat" modes (named after its shape as shown in Figure 5.2) in the refined meshes with matrix representations

$$\begin{aligned} \mathbf{z}_5 &= \{\ 1,\ 0,\ 0,\ 1,\ -\tfrac{1}{4},\ 0,\ -\tfrac{1}{4},\ -\tfrac{1}{2},\ \tfrac{5}{4}\ \}^{\mathrm{T}} \in \mathbb{R}^9\ , \\ \mathbf{z}_6 &= \{\ 1,\ 1,\ 0,\ 0,\ -\tfrac{1}{2},\ -\tfrac{1}{4},\ 0,\ -\tfrac{1}{4},\ \tfrac{5}{4}\ \}^{\mathrm{T}} \in \mathbb{R}^9\ , \end{aligned} \tag{5.1}$$

which as noted in Remark 4.4 are not orthogonal to $\{\mathbf{r}, \mathbf{z}_1, \mathbf{z}_2, \mathbf{z}_3, \mathbf{z}_4\}$. As the mesh is refined, a shift of the spurious eigen-modes to the higher frequencies can be observed from Table 5.2 where the spurious eigen-frequencies roughly double when the element size is halved.† Under mesh distortion, spurious modes such as the "bat" modes, which depends on the Jacobian matrix, may appear at a higher frequency, whereas the invariant spurious modes $\mathbf{z}_1$ and $\mathbf{z}_4$ remain practically unchanged. Also note that, for the same

† The typical upward shift of spurious eigen-frequencies is demonstrated using for example only two spurious modes: the displacement hourglass mode and the displacement "bat" mode.

Table 5.2 *Moderately thick plate. Shift of spurious frequencies with mesh refinement.*

No. of Elements	Hourglass mode		Disp. "bat" mode	
	Frequency (rad/s)	Ratio	Frequency (rad/s)	Ratio
1	1.3538	1.00	1.3834	1.00
4	2.6783	1.98	2.7289	1.97
16	5.3419	3.95	5.3853	3.89

mesh, decreasing the plate thickness will push the spurious rotation modes to the higher frequency range in the spectrum; the spurious displacement modes on the other hand remain at low frequency (see next example). All of the above spurious modes are completely filtered out of the spectrum when using the projected mass.‡ Further, exactly the same results as above are obtained for the square plate arbitrarily rotated in space. With this example, we have therefore exhibited all properties of the spurious eigenmodes, and shown that the proposed filtering scheme works for arbitrarily oriented elements. It remains to look at its effects on the accuracy of the computed frequencies of the genuine mode shapes.

5.1.2. Thin plate ($h = 0.001$). An advantage here is that we have analytical solution, complemented with experimental measures, of the vibrational frequencies and mode shapes. Parallel to Table 5.1 is Table 5.3 where as noted the rotation spurious modes have been shifted well beyond the 24th mode due to thickness decrease.

Figures 5.3b to 5.7b show the convergence results, with respect to mesh size, for the first six eigen-frequencies§ whose reference values are obtained from Leissa [1969, pp.104-111]: $\omega_1 = 1.2893 rad/s$, $\omega_2 = 1.8752 rad/s$, $\omega_3 = 2.3225 rad/s$, $\omega_4 = \omega_5 = 3.3643 rad/s$, and $\omega_6 = 6.0946 rad/s$. In these convergence plots, results obtained with four different types of mass matrix are displayed: the unprojected consistent mass† and three

‡ 30 eigenvectors, including the six first rigid body modes, were checked.

§ Note that the fourth and the fifth modes are just symmetric counterpart of each other, and have exactly the same eigen-frequency.

† Full integration is implied when we refer to a consistent mass. When uniformly reduced integration is used to

Table 5.3. *Thin square plate. Eigen-frequencies using unprojected mass matrix (uniform 4-element mesh).*

Mode	Freq. (rad/s)	Ratio	Description
1	1.3030	1.011	First elastic bending mode (Figure 5.3a).
2	1.9540	1.042	Second elastic bending mode (Figure 5.4a).
3	2.4730	1.065	Third elastic bending mode (Figure 5.5a).
4	2.6685	—	Spurious transverse (hourglass) mode $\{u_I^3\} = \mathbf{z}_1$ (Figure 5.1a).
5	2.6685	—	Spurious in-plane (hourglass) mode $\{u_I^{\{\alpha\}}\} = \mathbf{z}_1$ (Figure 5.1b).
6	2.6685	—	Spurious in-plane (hourglass) mode $\{u_I^{\{\alpha\}}\} = \mathbf{z}_1$.
7	2.7235	—	Spurious in-plane mode (disp. "bat" mode) (Figure 5.2).
8	3.4030	1.011	Fourth elastic bending mode (Figure 5.6a).
9	3.4030	1.011	Fifth elastic bending mode (Figure 5.6a).
10	6.3577	1.043	Sixth elastic bending mode (Figure 5.7a).

types of projected masses (using fully-integrated consistent mass matrix, under-integrated consistent mass matrix, and lumped mass matrix). Again, spurious modes are completely filtered from the perturbed eigen-system $[\mathbf{K}^* - \omega_i^2 \mathbf{M}^*]\boldsymbol{\phi}_i = 0$.‡

Consistently in all of the first six modes, the projected mass yields better computed values of the eigen-frequencies than with other types of mass matrix. Starting already from the 4-element mesh, these computed frequencies — bracketed by those of the unprojected consistent mass (from above) and by those of the projected lumped mass (from below) — are on the low side of the reference values.§ All results show convergence of eigen-frequencies with respect to mesh refinement.

Figure 5.8 reports the percentage error of the first 20 eigenvalues obtained using the projected mass matrix with the uniform 64-element mesh and the uniform 256-element mesh. The reference frequencies for these modes, given in Leissa [1969, pp.104-111] and gathered in Table 5.4, are obtained by series solution, except for modes 7, 8, 17,

evaluate the consistent mass, the result is always explicitly referred to as *under-integrated* consistent mass.

‡ The first 40 modes of the 4-element mesh, and the first 20 modes of the 64-element and of 256-element meshes were examined.

§ In the fourth and fifth modes, the computed frequency from both the projected mass and the unprojected consistent mass are about 1.5% lower than the reference value for the 64-element mesh. On the other hand, the computed frequency with the one-element mesh is surprisingly good.

18, and 19 where experimental values are used. This explains the larger error in frequencies when we compared computed values with experimental measures. For the remaining modes, the relative error for the 256-element mesh falls within 2% — on the low side — of the theoretical values. Note that unlike in the reference solution of Table 5.4, the computed modes 7 and 8 appear before mode 6, whose computed frequency is slightly higher.

Table 5.4. *Thin free square plate. Reference frequencies for the first 20 eigenvectors.*

Mode	Frequency (rad/s)	Mode	Frequency (rad/s)
1	1.2893	11	10.093
2	1.8752	12	10.093
3	2.3225	13	11.207
4	3.3643	14	11.712
5	3.3643	15	12.581
6*	6.0946	16	12.581
7* †	6.2555	17 †	14.956
8* †	6.2555	18 †	16.123
9	6.6511	19 †	16.620
10	7.4251	20	20.379

* The order of these modes changes in computed results.
† Experimental values are used for these modes.

It is seen in the above two examples that the proposed perturbation method achieves in a very efficient manner a complete filtering of undesirable spurious modes polluting the dynamic response. Further, the use of the projected (fully-integrated consistent) mass matrix yields reliable and accurate results, even for coarse meshes. The superiority of this type of mass matrix over the others is consistently established for all the eigenmodes considered above. The projected under-integrated consistent mass and lumped mass, in addition to being less accurate, yield unpredictable results for coarse meshes; they are not recommended for use in general analysis. In the following examples, only results obtained with the (fully-integrated) consistent mass matrix are presented.

5.2. Simply-supported thick circular plate. In many cases, boundary conditions alone are not sufficient to prevent the appearance of spurious modes; the reliability and effectiveness of the proposed perturbation method is again demonstrated in this example. Consider a circular plate, with radius $R = 5$ and thickness $h = 1$, simply supported on its circumference. The material properties used are $E = 1000$ and $\nu = 0.3$. Only a quarter of the plate is modeled. We consider only those modes that are symmetric with respect to the planes $\{\mathbf{E}_1, \mathbf{E}_3\}$ and $\{\mathbf{E}_2, \mathbf{E}_3\}$. Using the unprojected mass, a spurious transverse displacement mode of the type $\mathbf{z}_1$ appears in a 3-element mesh (Figure 5.9) as the ninth mode with frequency $290.72 rad/s$, in a 12-element mesh as the 16th mode with frequency $378.26 rad/s$, and in a 48-element mesh as the 20th mode with frequency $398.66 rad/s$. This spurious mode disappears when the projected mass is used.

The computed frequencies of the first three modes normalized with respect to the value obtained with the 48-element mesh, are presented in Figure 5.10. These reference numerical values are: $\omega_1 = 34.112 rad/s$, $\omega_2 = 131.21 rad/s$, and $\omega_3 = 149.26 rad/s$. Fast convergence is obtained with both the unprojected consistent mass and the projected consistent mass, with results from the latter on the lower side as in the case of the square plate above.

5.3. Thin cylindrical shell. We now apply the perturbation method to the important case of cylindrical shells. Consider a cylinder with thickness $h = 15$, radius $R = 300$ and length $L = 1200$. The material properties are $E = 3 \times 10^6$ and $\nu = 0.3$. Two types of end conditions are considered: (i) the free ends, and (ii) the rigid diaphragms.

5.3.1. Cylinder with free ends. The unrestrained ends of the cylinder allows appearance of spurious modes because the under-integrated stiffness matrix is here rank deficient. This example therefore provides a test for the proposed perturbation scheme in eliminating spurious modes. We study only eigenmodes with three planes of symmetry, which then require modeling over only 1/8th of the cylinder.† The eigenfunctions

† Note that by modeling only 1/8th of the cylinder, and by imposing symmetric boundary conditions in the plane of symmetry, we already prevent some of the spurious modes to appear.

of a cylinder are characterized by a doublet (m, n), where m designates the number of half-waves along the longitudinal direction, and n the number of full-waves along the circumferential direction.

Since no reference solution is available, we present in Table 5.5 only results obtained using a 4-element mesh. The order of the frequencies reported corresponds to the eigenvalue analysis using the unprojected consistent mass matrix. The ratio of these frequencies with those of the projected consistent mass matrix indicates that in general the projected mass yields lower computed frequencies.

Table 5.5. *Thin cylinder with free ends. 4-element mesh. Numerical results for the first twelve frequencies*

Mode	Frequency (rad/s) Unprojected Mass	Frequency (rad/s) Projected Mass	Ratio of freq. Unproj./Proj.	m	n
1	2.3745	2.3666	1.0033	0	2
2*	14.8454	—	—	—	—
3	14.9697	14.8183	1.0102	1	2
4	15.2580	14.7466	1.0347	0	4
5	17.3628	16.9320	1.0254	1	4
6	29.1246	29.5928	0.9842	3	4
7	39.8828	39.4061	1.0121	3	2
8	43.0092	42.9038	1.0025	1	0
9	45.5208	—	—	5	0
10	45.7791	44.6116	1.0262	5	4
11*	45.7942	—	—	—	—
12	46.8714	47.8572	0.9794	5	2

* These modes are spurious.

Modes 2 and 11, plotted in Figures 5.11a and 5.11b, are spurious modes obtained when using the unprojected mass matrix. The ninth mode with nodal pattern $(m,n) = (5,0)$ does not appear in the analysis using the projected mass matrix. However, a characteristic of the vibrational frequencies of a cylinder is to be noted: A finer mesh will reveal more lower-frequency modes with higher values of wave numbers (m, n); the mode $(m, n) = (5,0)$ can be recovered using a finer mesh.

5.3.2. Cylinder with rigid diaphragms. The ends of the cylinder are restrained by rigid diaphragms. These boundary conditions have received particular attention in the literature because they can be exactly satisfied by simple trigonometric functions leading to analytical results, and thereby allowing an assessment on the accuracy of the proposed perturbation method.

In shell theory, for given values of m and n, the vibrational frequencies are solutions of a third degree polynomial — we refer to Leissa [1973, pp.43-83]. Thus, a cylinder with finite length may vibrate in any three different modes, corresponding to three different frequencies, with the same number of longitudinal and circumferential waves (m, n). The modes are classified as primarily flexural, extensional or torsional, according to the type of strain energy stored in the motion. In general, the lowest frequency is primarily flexural. Determining the fundamental frequency of a finite cylinder is not an easy task: Eigenfunctions obtained for larger values of m and n may have lower frequencies than those obtained for smaller values of m and n. Therefore, as mentioned earlier, by refining the mesh — thus allowing the appearance of modes with higher number of waves — one sees the emergence of yet more modes with lower frequencies.

Only eigenmodes with a single longitudinal half-wave ($m = 1$) are considered in this study. Modeling only an eighth of the cylinder and using three different sets of boundary conditions allows one to obtain the different circumferential patterns. The eigenmodes for the first five circumferential modes ($n = 0,...,4$) are shown in Figures 5.12a to 5.12e, and the convergence of eigen-frequencies in Figures 5.13a and 5.13b. Results for $n = 0,1,2$ are obtained using meshes with 1, 4, and 16 elements; those for $n = 3,4$ are obtained using meshes with 4, 16, and 64 elements. The reference solution of this example, based on a three-dimensional theory, is presented in Leissa [1973, p.55]. These reference frequencies for the above mentioned five modes are: $\omega_0 = 43.0021 rad/s$, $\omega_1 = 15.5550 rad/s$, $\omega_2 = 7.3383 rad/s$, $\omega_3 = 7.8608 rad/s$ and $\omega_4 = 13.2604 rad/s$, where the

subscripts designate the wave number n, and not the customary order in magnitude of the frequencies. The mode $(m, n) = (1, 0)$ is a primarily extensional mode, whereas others are primarily flexural modes. Similar to the results in the previous examples, the frequencies obtained using the projected mass matrix are generally lower and more accurate than those obtained without employing the proposed projection.

Closure

We have presented a perturbation method for dynamic analysis using under-integrated shell elements, which achieves a complete filtering of all spurious modes from the eigen-spectrum. The present approach not only retains all of the previously obtained properties of the 9-node shell element, but extends its capability to dynamic analysis. Based on a careful examination of the 9-node element in various geometrical shapes, we propose highly efficient (i) perturbation method for the stiffness matrix and (ii) projection method for the mass matrix, with both methods performed directly in the global coordinate system. The efficiency of the method therefore lies in (a) the complete absence of local-global coordinate transformation of element matrices, (b) that the perturbation factor for the stiffness does not involve terms requiring full integration over the element, but in fact requires no additional computing effort, (c) that the projection operator for the mass matrix is known a-priori in algebraic form, (d) that these operations are carried out only once for each element, and not at each integration point. It can be seen from all the above examples that the proposed perturbation method offers a reliable, effective, and accurate method for dynamic analysis of general shell structures using under-integrated elements.

Acknowledgements

The coding of the dynamic procedure and the running of test examples presented above were done with the assistance of J.A. Mora. This assistance is appreciated. The encouragement from Prof. R.L. Taylor and Dr. J.E. Higgins throughout this research is gratefully acknowledged.

References

Belytschko, T., Ong, J.S.J., and Liu, W.K. [1984], "A consistent control of spurious singular modes in the 9-node Lagrangian element for the Laplace and Mindlin plate equations," *Comp. Meth. Appl. Mech. Engng.*, Vol. 44, pp. 269-295.

Belytschko, T., Liu, W.K., Ong, J.S.J., and Lam, D. [1985], "Implementation and application of a 9-node Lagrange shell element with spurious mode control," *Computer & Structures*, Vol. 20, pp. 121-128.

Belytschko, T., Tsay, C.S., and Liu, W.K. [1981], "A stabilization matrix for the bilinear Mindlin plate element," *Comp. Meth. Appl. Mech. Engng.*, Vol. 29, pp. 303-327.

Flanagan, D.P., and Belytschko, T. [1981], "A uniform strain hexahedron and quadrilateral with orthogonal hourglass control," *Int. J. Numer. Meth. Engng.*, Vol. 17, pp. 679-706.

Hughes, T.J.R. [1983], "Analysis of transient algorithms with particular reference to stability behavior," in *Computational Methods for Transient Analysis* edited by T. Belytschko and T.J.R. Hughes, North Holland Elsevier Science Publishers, Amsterdam.

Leissa, A.W. [1969], *Vibrations of Plates*, NASA Technical Report SP-160, Washington, D.C.

Leissa, A.W. [1973], *Vibrations of Shells*, NASA Technical Report SP-288, Washington, D.C.

Malkus, D.S., and Hughes, T.J.R. [1978], "Mixed finite element — reduced and selective integration techniques: A unification of concepts," *Comp. Meth. Appl. Mech. Engng.*, Vol. 15, pp. 63-81.

Parisch, H. [1979], "A critical survey of the 9-node degenerated shell element with special emphasis on thin shell applications and reduced integration," *Comp. Meth. Appl. Mech. Engng.*, Vol. 20, pp. 323-350.

Pawsey, S.F., and Clough, R.W. [1971], "Improved numerical integration for thick slab finite elements," *Int. J. Num. Meth. Engng.*, Vol. 3, pp. 575-586.

Taylor, R.L., Simo, J.C., Zienkiewicz, O.C., and Chan, A.C.H. [1986], "The patch tests — A condition for assessing FEM convergence," *Int. J. Num. Meth. Engng.*, Vol. 22, pp. 39-62.

Vu-Quoc, L. [1986], *Dynamics of Flexible Structures Performing Large Overall Motions: A Geometrically-Nonlinear Approach*, Doctoral Dissertation, Electronics Research Laboratory Memorandum UCB/ERL M86/36, University of California, Berkeley.

Vu-Quoc, L., and Mora, J.A. [1987], "A class of simple and efficient degenerated shell elements," Structural Engineering, Mechanics, and Materials, report no. UCB/SEMM-87/05, Nisee Center, University of California, Berkeley, July. (Submitted for publication.)

Wilson, E.L., and Penzien, J. [1972], "Evaluation of orthogonal damping matrices," *Int. J. Num. Meth. Engng.*, Vol. 4, No. 1, pp. 5-10.

Zienkiewicz, O.C., Taylor, R.L., and Too, J.M. [1971], "Reduced integration techniques in general analysis of plates and shells," *Int. J. Num. Meth. Engng.*, Vol. 3, pp. 275-290.

Zienkiewicz, O.C. [1978], *The Finite Element Method*, third edition, McGraw-Hill, London.

Appendix

We summarized here details of the vectors $\mathbf{w}_i \in \mathbb{R}^{N^e}$ employed in the construction of the perturbation matrix as discussed in Section 3.3. For a 4-node ($N^e = 4$) shell element or for a curved 9-node ($N^e = 9$) shell element, the perturbation is required to be orthogonal to a displacement field that is linear in the coordinates; thus, in the expression for vectors $\bar{\mathbf{b}}_i$ in (3.30a), we have $m = 3$, and

$$[\,\mathbf{w}_1, \mathbf{w}_2, \mathbf{w}_3\,] = \begin{bmatrix} 1 & X_1^1 & X_1^2 \\ . & . & . \\ . & . & . \\ . & . & . \\ 1 & X_{N^e}^1 & X_{N^e}^2 \end{bmatrix} \in \mathbb{R}^{N^e \times 3}\,. \tag{A.1}$$

Note that $\mathbf{w}_1 = \mathbf{r}$. For a flat 9-node element, the perturbation is further required to be orthogonal to a displacement field that is quadratic in the coordinates; thus, to the above vectors $\mathbf{w}_i$ we append ($N^e = 9$)

$$[\,\mathbf{w}_4\,, \ldots,\, \mathbf{w}_9\,] = \begin{bmatrix} (X_1^1)^2 & (X_1^2)^2 & (X_1^3)^2 & (X_1^1X_1^2) & (X_1^2X_1^3) & (X_1^3X_1^1) \\ . & . & . & . & . & . \\ . & . & . & . & . & . \\ . & . & . & . & . & . \\ (X_9^1)^2 & (X_9^2)^2 & (X_9^3)^2 & (X_9^1X_9^2) & (X_9^2X_9^3) & (X_9^3X_9^1) \end{bmatrix} \in \mathbb{R}^{9\times 6}\,. \tag{A.2}$$

□

Figure captions

Figure 3.1. *Parallelogrammic 9-node shell element.* Geometry.

Figure 3.2a. *Cylindrical 9-node shell element.* Geometry.

Figure 3.2b. *Cylindrical 9-node shell element.* Constant director field $\mathbf{A}_3 \equiv \mathbf{E}_3$.

Figure 3.2c. *Cylindrical 9-node shell element.* Radial director field.

Figure 3.3a. *Patch test for 9-node shell element.* A 5-element patch.

Figure 3.3b. *Patch test for 9-node shell element.* Twisting of a Reisner-Mindlin plate. Boundary conditions, and nodal values of distributed moment on a one-element patch.

Figure 3.3c. *Patch test for 9-node shell element.* Twisting of a Kirchhoff-Love plate. Boundary conditions, and nodal values of distributed moment on a one-element patch.

Figure 5.1a. *Free square plate.* 4-element mesh. Spurious transverse displacement (hourglass) mode.

Figure 5.1b. *Free square plate.* 4-element mesh. Spurious in-plane displacement (hourglass) mode.

Figure 5.2. *Free square plate.* The "bat" mode: in-plane spurious mode. (a) in 4-element mesh. (b) in 16-element mesh.

Figure 5.3a. *Free square plate.* First eigen-mode (for both values of thickness).

Figure 5.3b. *Thin free square plate.* First eigen-frequency. Convergence plot. Solid line: Projected mass. C: Unprojected consistent mass. R: Projected under-integrated consistent mass. L: Projected lumped mass.

Figure 5.4a. *Free square plate.* Second eigen-mode (for both values of thickness).

Figure 5.4b. *Thin free square plate.* Second eigen-frequency. Convergence plot. Solid line: Projected mass. C: Unprojected consistent mass. R: Projected under-integrated consistent mass. L: Projected lumped mass.

Figure 5.5a. *Free square plate.* Third eigen-mode (for both values of thickness).

Figure 5.5b. *Thin free square plate.* Third eigen-frequency. Convergence plot. Solid line: Projected mass. C: Unprojected consistent mass. R: Projected under-integrated consistent mass. L: Projected lumped mass.

Figure 5.6a. *Free square plate.* Fourth and fifth eigen-mode (for both values of thickness).

Figure 5.6b. *Thin free square plate.* Fourth and fifth eigen-frequency. Convergence plot. Solid line: Projected mass. C: Unprojected consistent mass. R: Projected under-integrated consistent mass. L: Projected lumped mass.

Figure 5.7a. *Free square plate.* Sixth eigen-mode (for both values of thickness).

Figure 5.7b. *Thin free square plate.* Sixth eigen-frequency. Convergence plot. Solid line: Projected mass. C: Unprojected consistent mass. R: Projected under-integrated consistent mass. L: Projected lumped mass.

Figure 5.8. *Thin free square plate.* Relative error of the first 20 eigen-frequencies using 64-element (dotted line) and 256-element (solid line) meshes.

Figure 5.9. *Simply-supported thick circular plate.* Ninth mode: Spurious transverse displacement mode of type $\mathbf{z}_1$.

Figure 5.10. *Simply-supported thick circular plate.* Convergence of the first three eigen-frequencies. Solid line: Projected mass. Dotted line: Unprojected mass.

Figure 5.11a. *Cylindrical shell with free ends.* Mode 2: First spurious mode.

Figure 5.11b. *Cylindrical shell with free ends.* Mode 11: Second spurious mode.

Figure 5.12a. *Cylindrical shell with rigid diaphragms.* Mode $(m, n) = (1,0)$.

Figure 5.12b. *Cylindrical shell with rigid diaphragms.* Mode $(m, n) = (1,1)$.

Figure 5.12c. *Cylindrical shell with rigid diaphragms.* Mode $(m, n) = (1,2)$.

Figure 5.12d. *Cylindrical shell with rigid diaphragms.* Mode $(m, n) = (1,3)$.

Figure 5.12e. *Cylindrical shell with rigid diaphragms.* Mode $(m, n) = (1,4)$.

Figure 5.13a. *Cylindrical shell with rigid diaphragms.* Convergence of frequencies for modes $(m, n) = (1,0), (1,1), (1,2)$. Solid line: Projected mass. Dotted line: Unprojected mass.

Figure 5.13b. *Cylindrical shell with rigid diaphragms.* Convergence of frequencies for modes $(m, n) = (1,3), (1,4)$. Solid line: Projected mass. Dotted line: Unprojected mass.

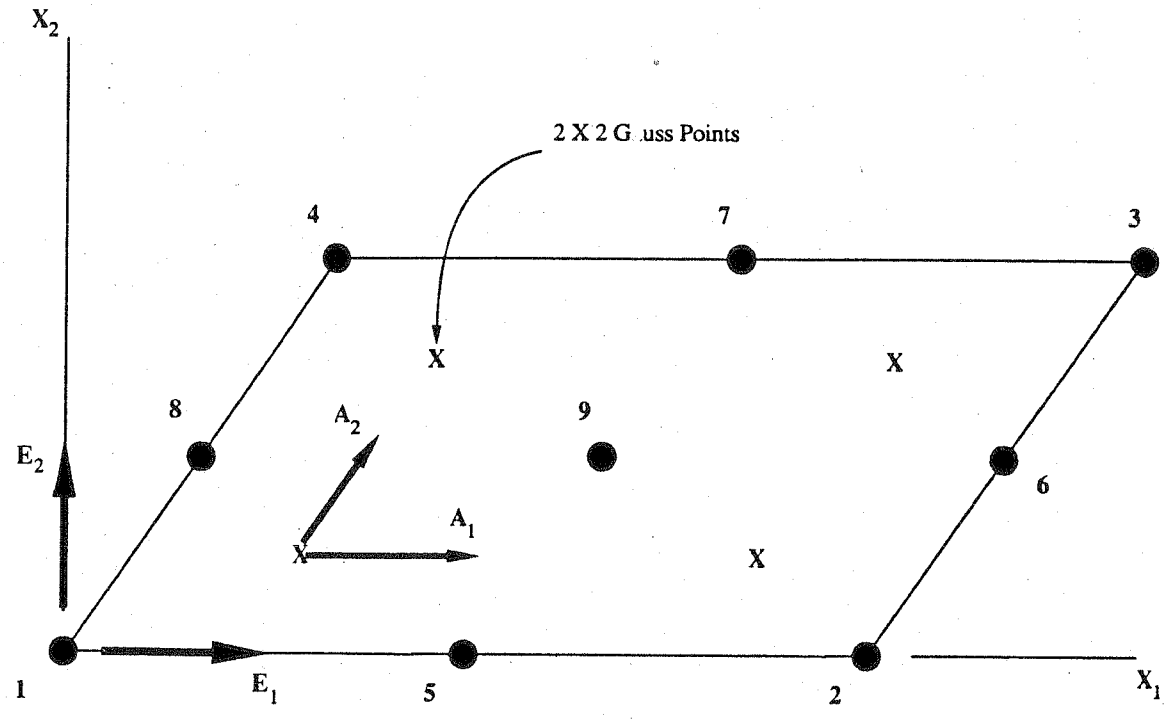

Figure 3.1. *Parallelogrammic 9-node shell element.* Geometry.

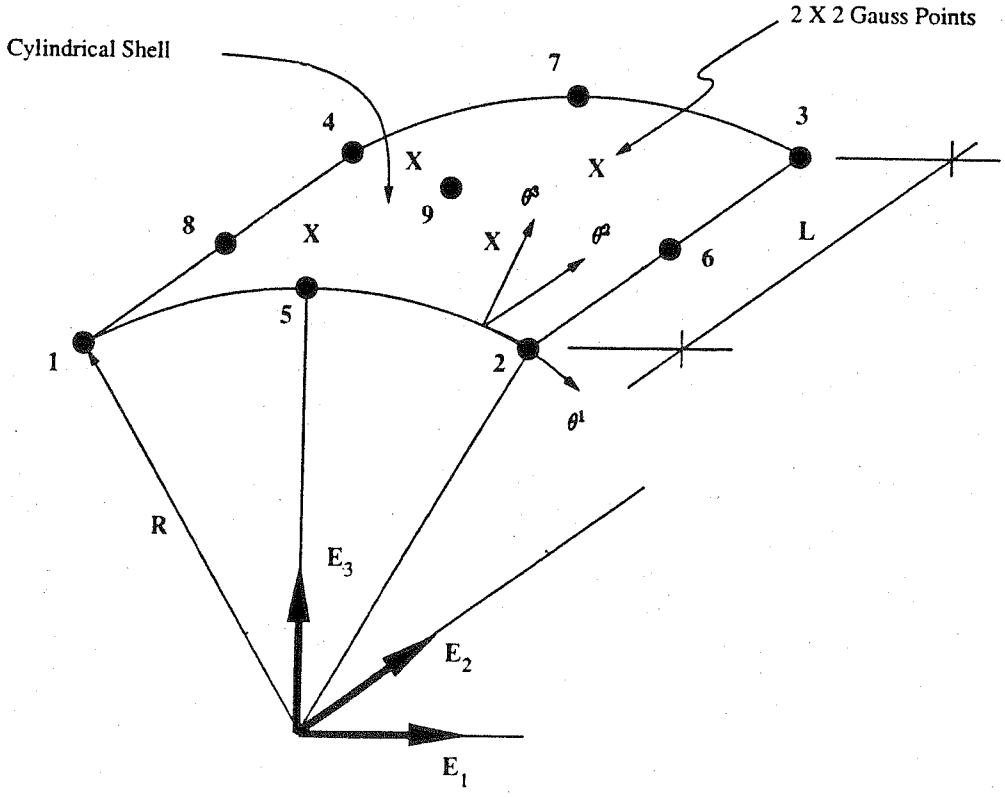

Figure 3.2a. *Cylindrical 9-node shell element.* Geometry.

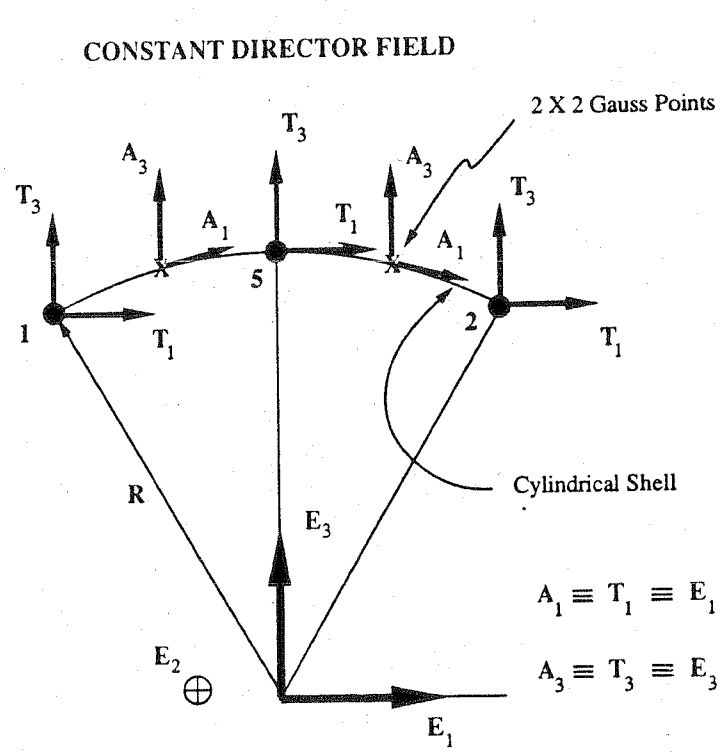

Figure 3.2b. *Cylindrical 9-node shell element.* Constant director field $\mathbf{A}_3 \equiv \mathbf{E}_3$.

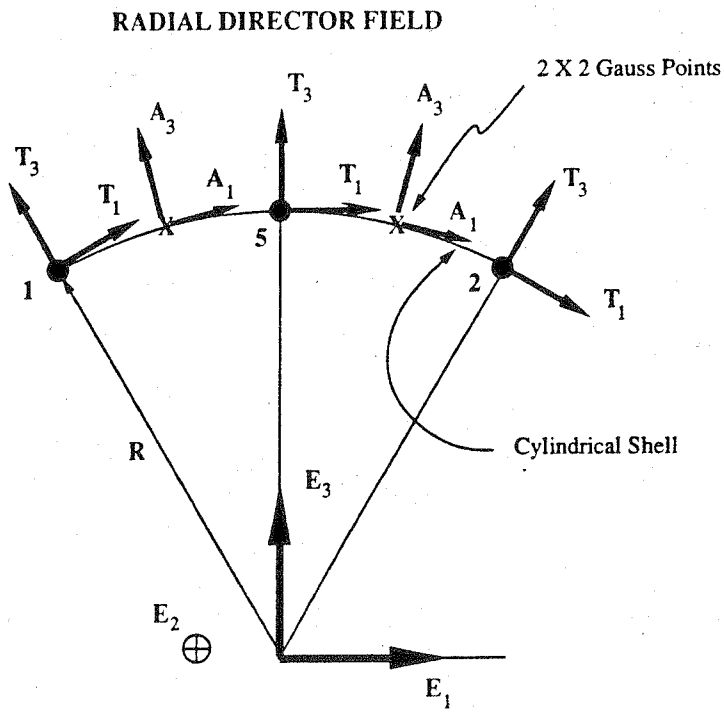

Figure 3.2c. *Cylindrical 9-node shell element.* Radial director field.

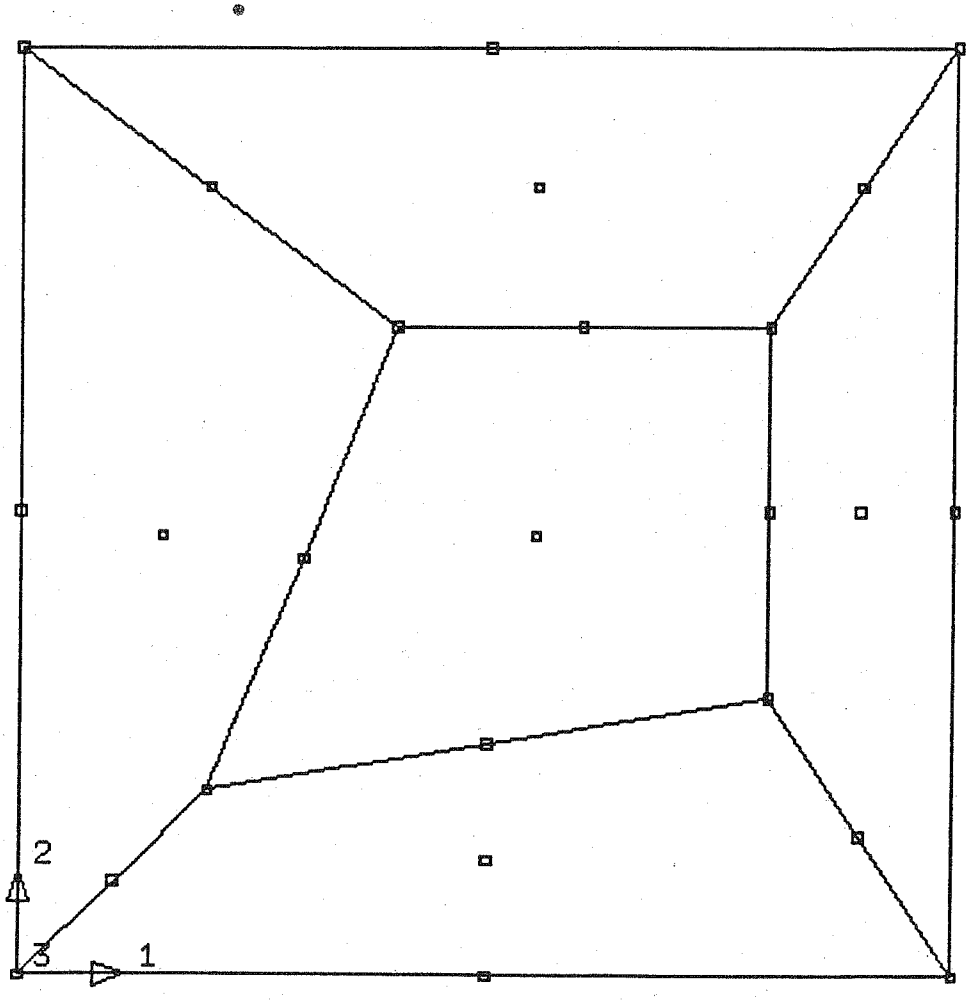

FEAP

Figure 3.3a. *Patch test for 9-node shell element.* A 5-element patch.

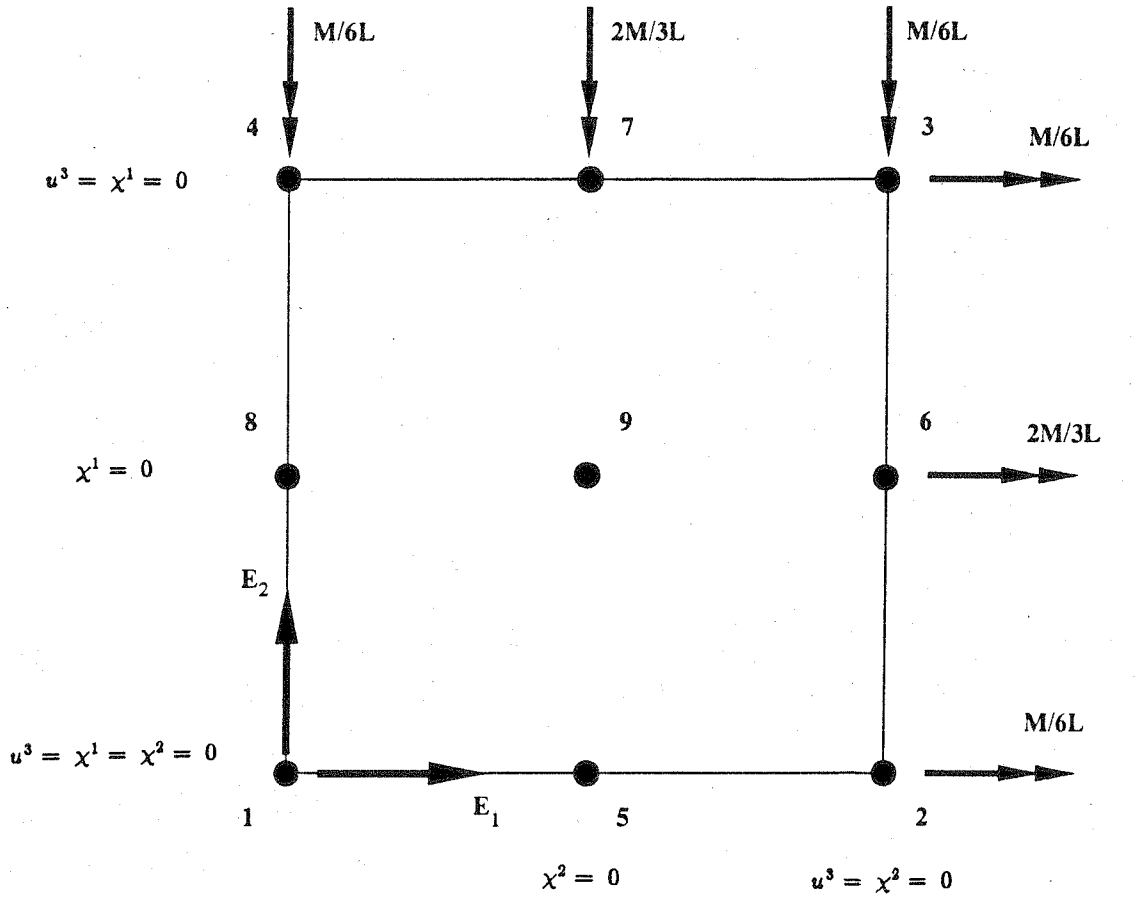

Figure 3.3b. *Patch test for 9-node shell element.* Twisting of a Reisner-Mindlin plate. Boundary conditions, and nodal values of distributed moment on a one-element patch.

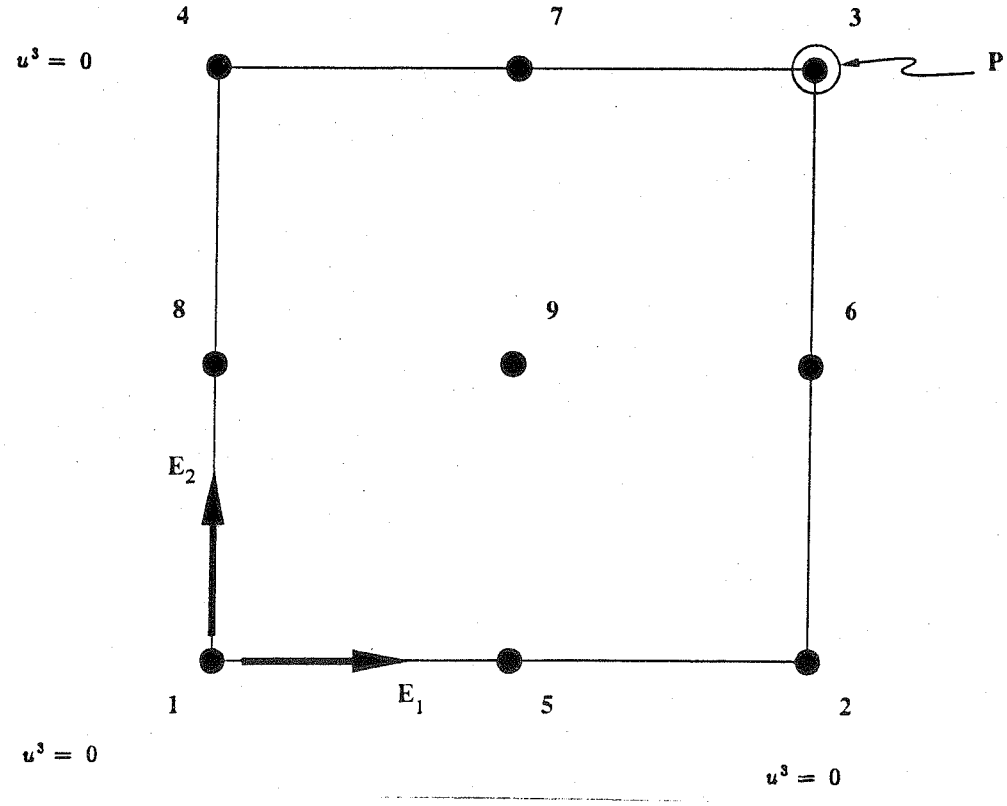

Figure 3.3c. *Patch test for 9-node shell element.* Twisting of a Kirchhoff-Love plate. Boundary conditions, and nodal values of distributed moment on a one-element patch.

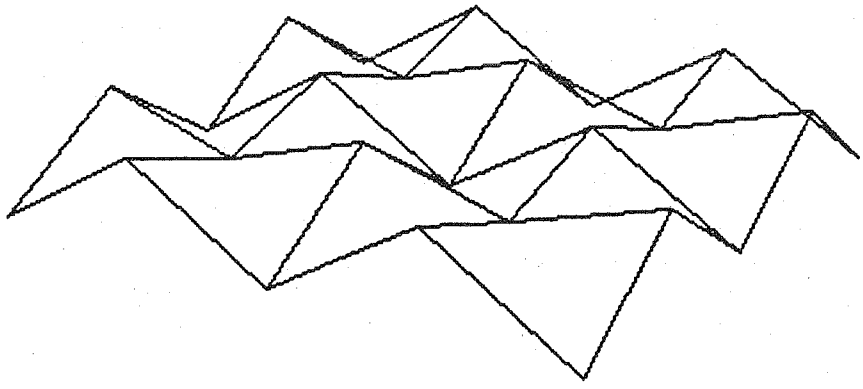

Figure 5.1a. *Free square plate.* 4-element mesh. Spurious transverse displacement (hourglass) mode.

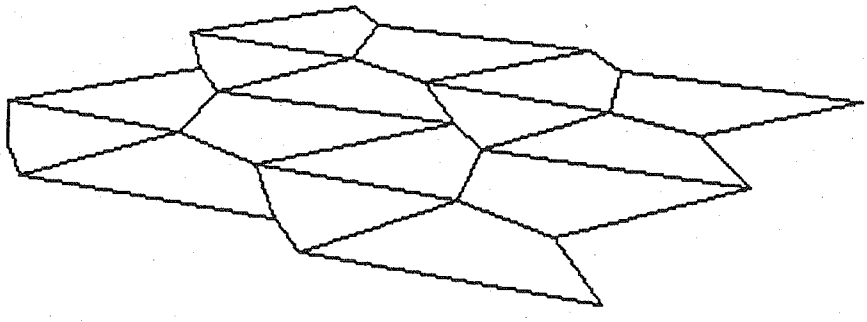

Figure 5.1b. *Free square plate.* 4-element mesh. Spurious in-plane displacement (hourglass) mode.

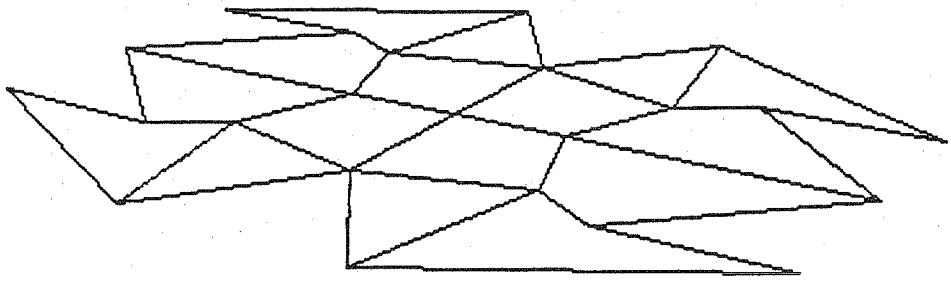

(a) 4-element mesh with lines connecting mid-side nodes to interior nodes drawn.

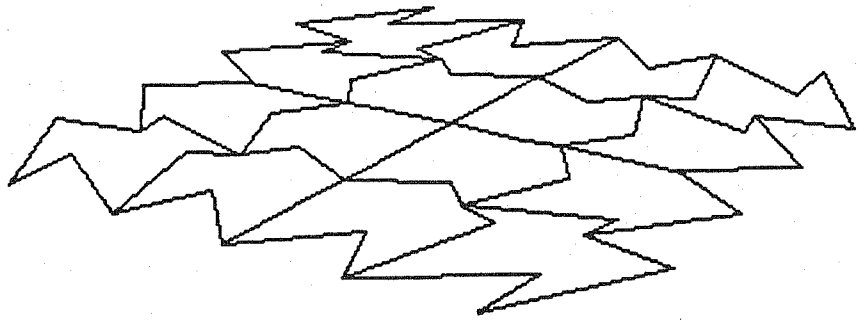

(b) 16-element mesh

Figure 5.2. *Free square plate.* The "bat" mode: in-plane spurious mode. (a) in 4-element mesh. (b) in 16-element mesh.

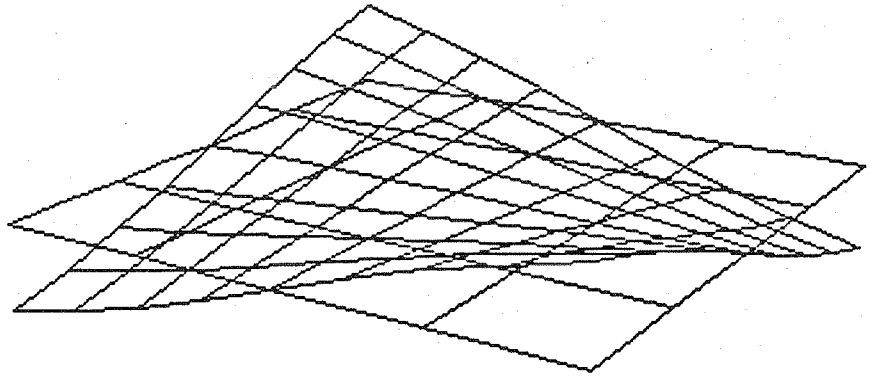

Figure 5.3a. *Free square plate.* First eigen-mode (for both values of thickness).

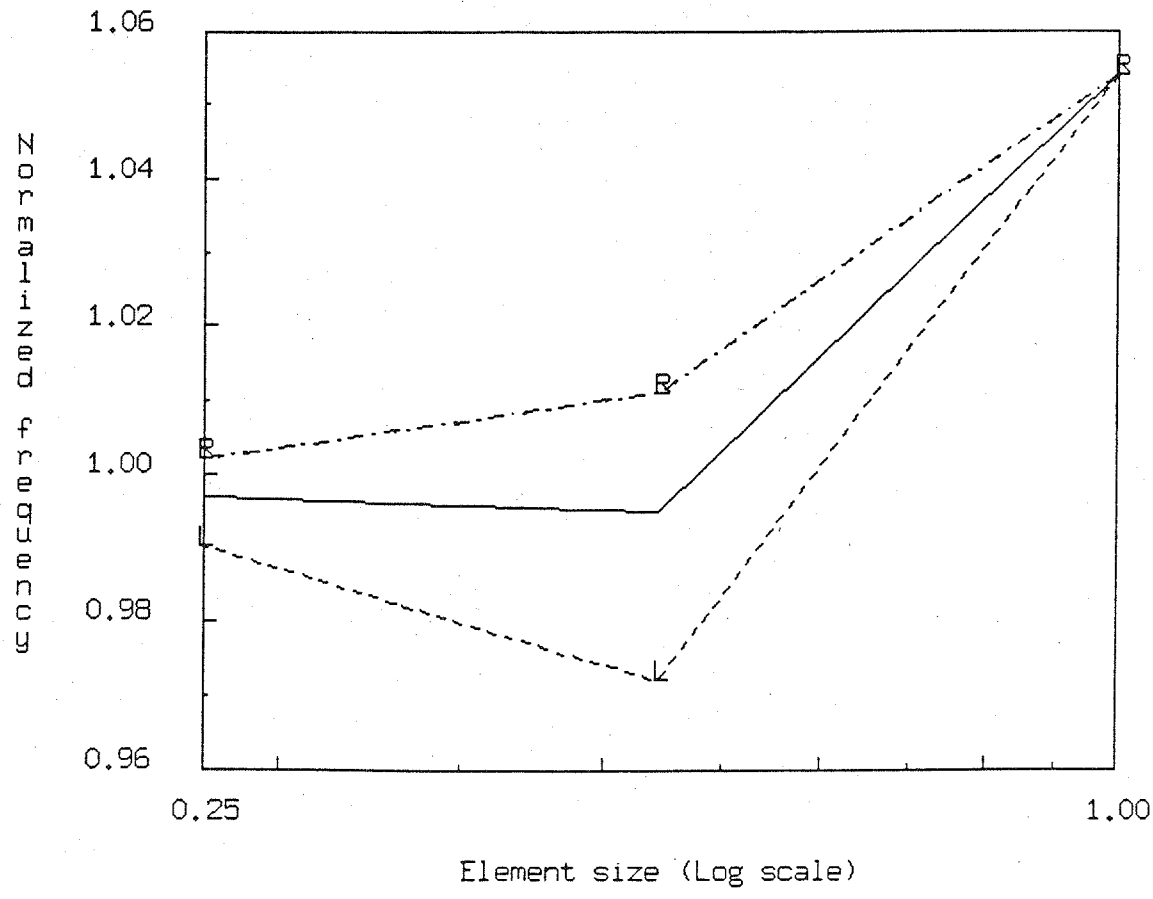

Figure 5.3b. *Thin free square plate.* First eigen-frequency. Convergence plot. Solid line: Projected mass. C: Unprojected consistent mass. R: Projected under-integrated consistent mass. L: Projected lumped mass.

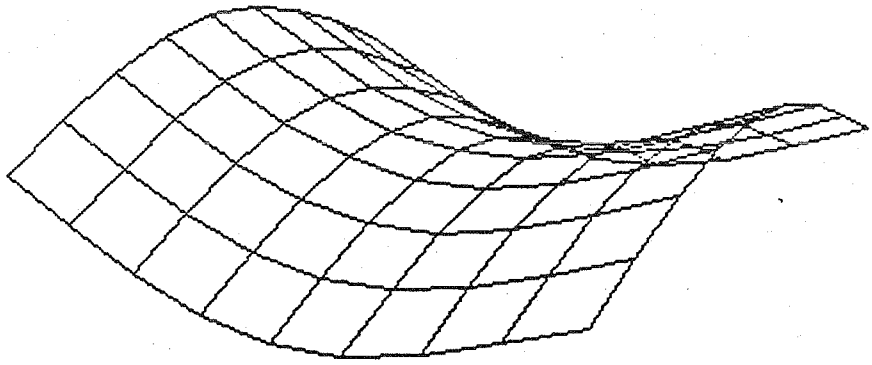

Figure 5.4a. *Free square plate.* Second eigen-mode (for both values of thickness).

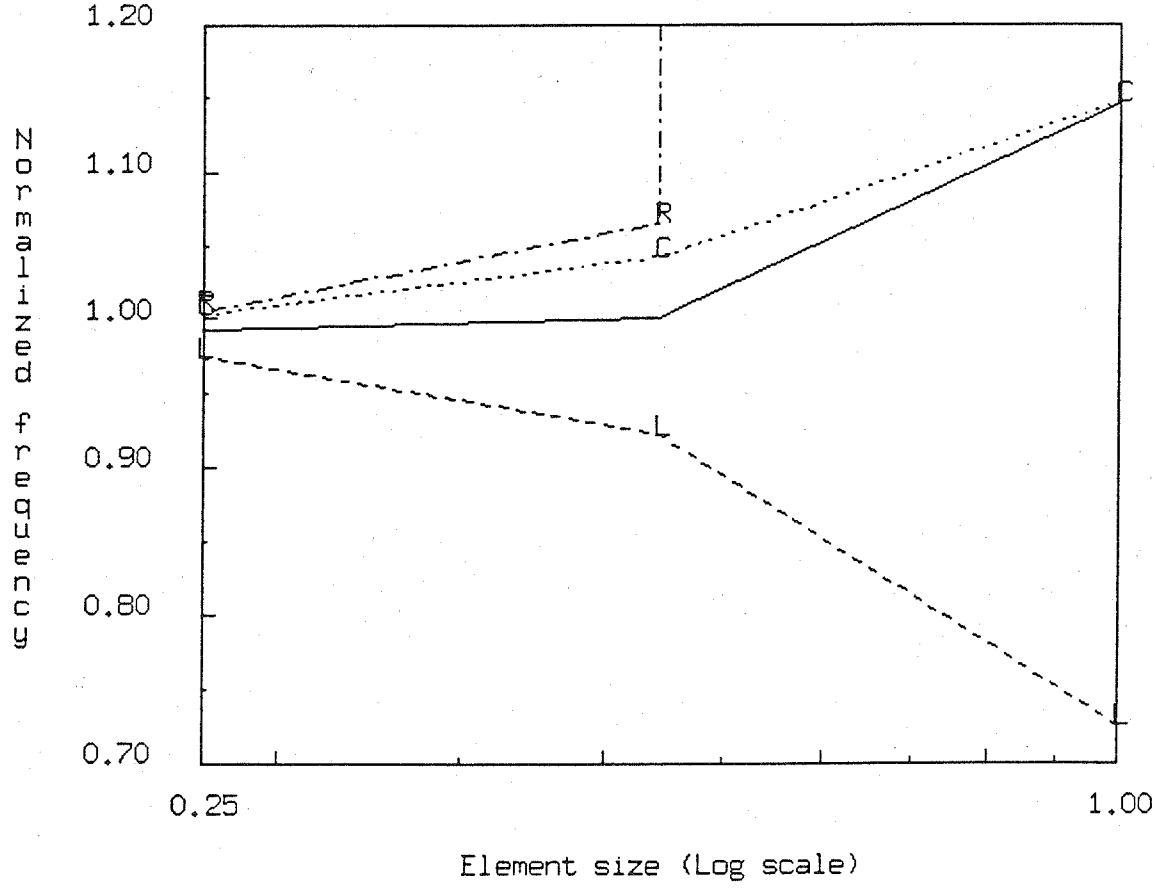

Figure 5.4b. *Thin free square plate.* Second eigen-frequency. Convergence plot. Solid line: Projected mass. C: Unprojected consistent mass. R: Projected under-integrated consistent mass. L: Projected lumped mass.

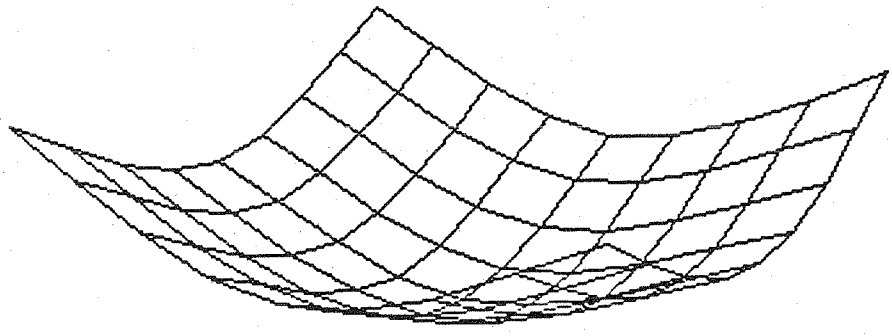

Figure 5.5a. *Free square plate.* Third eigen-mode (for both values of thickness).

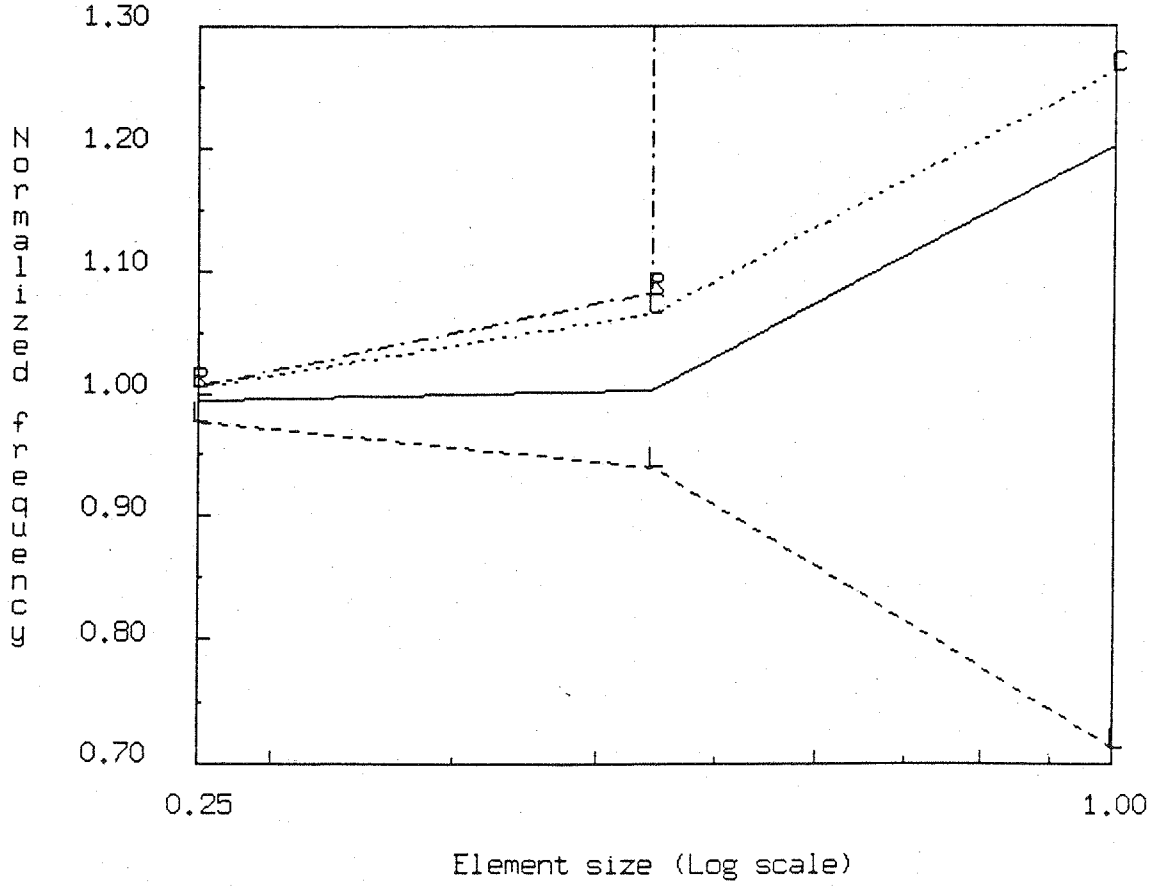

Figure 5.5b. *Thin free square plate.* Third eigen-frequency. Convergence plot. Solid line: Projected mass. C: Unprojected consistent mass. R: Projected under-integrated consistent mass. L: Projected lumped mass.

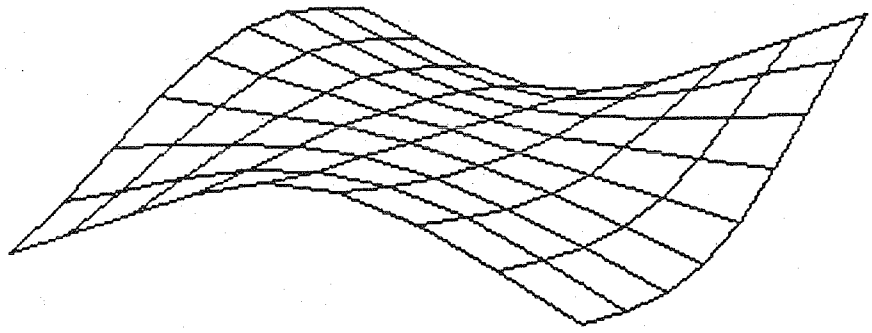

Figure 5.6a. *Free square plate.* Fourth and fifth eigen-mode (for both values of thickness).

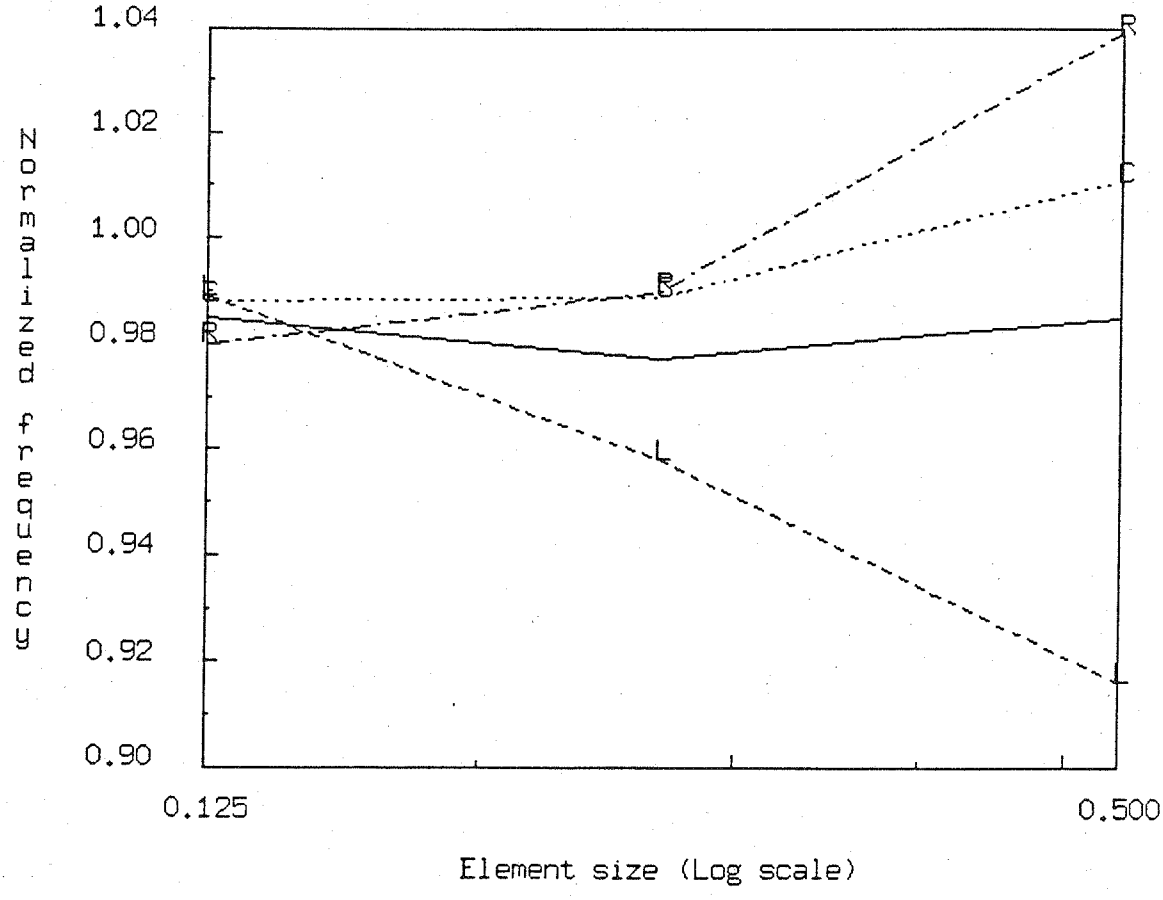

Figure 5.6b. *Thin free square plate.* Fourth and fifth eigen-frequency. Convergence plot. Solid line: Projected mass. C: Unprojected consistent mass. R: Projected under-integrated consistent mass. L: Projected lumped mass.

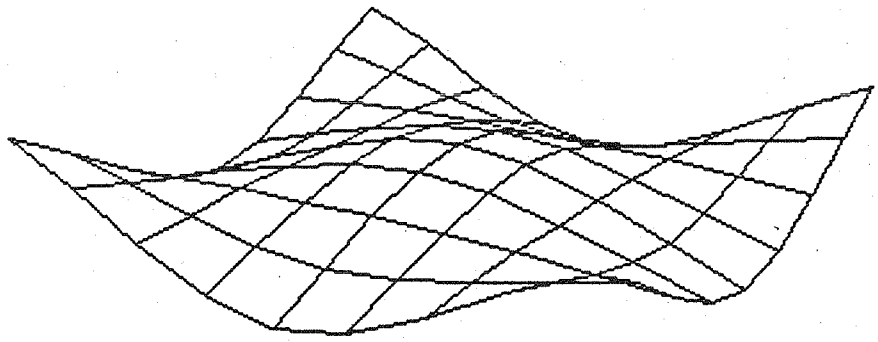

Figure 5.7a. *Free square plate.* Sixth eigen-mode (for both values of thickness).

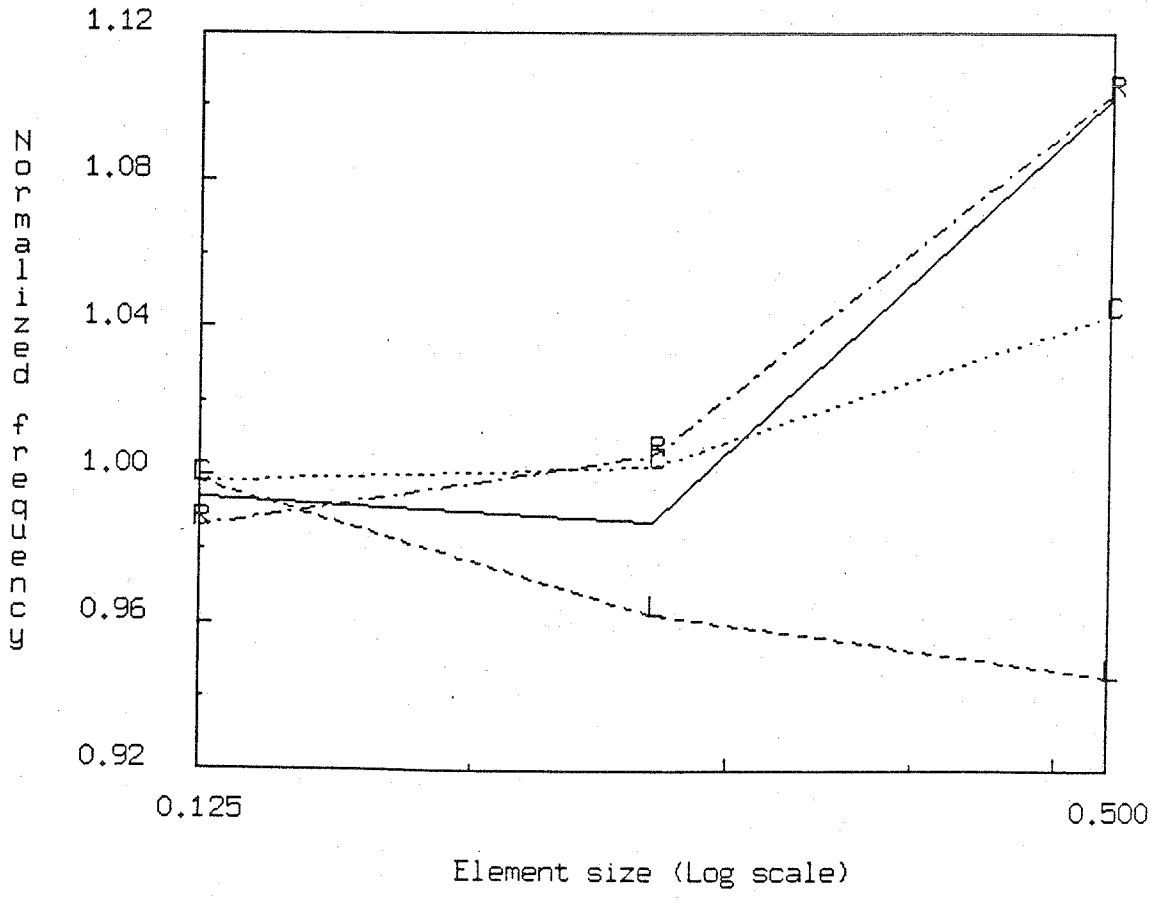

Figure 5.7b. *Thin free square plate.* Sixth eigen-frequency. Convergence plot. Solid line: Projected mass. C: Unprojected consistent mass. R: Projected under-integrated consistent mass. L: Projected lumped mass.

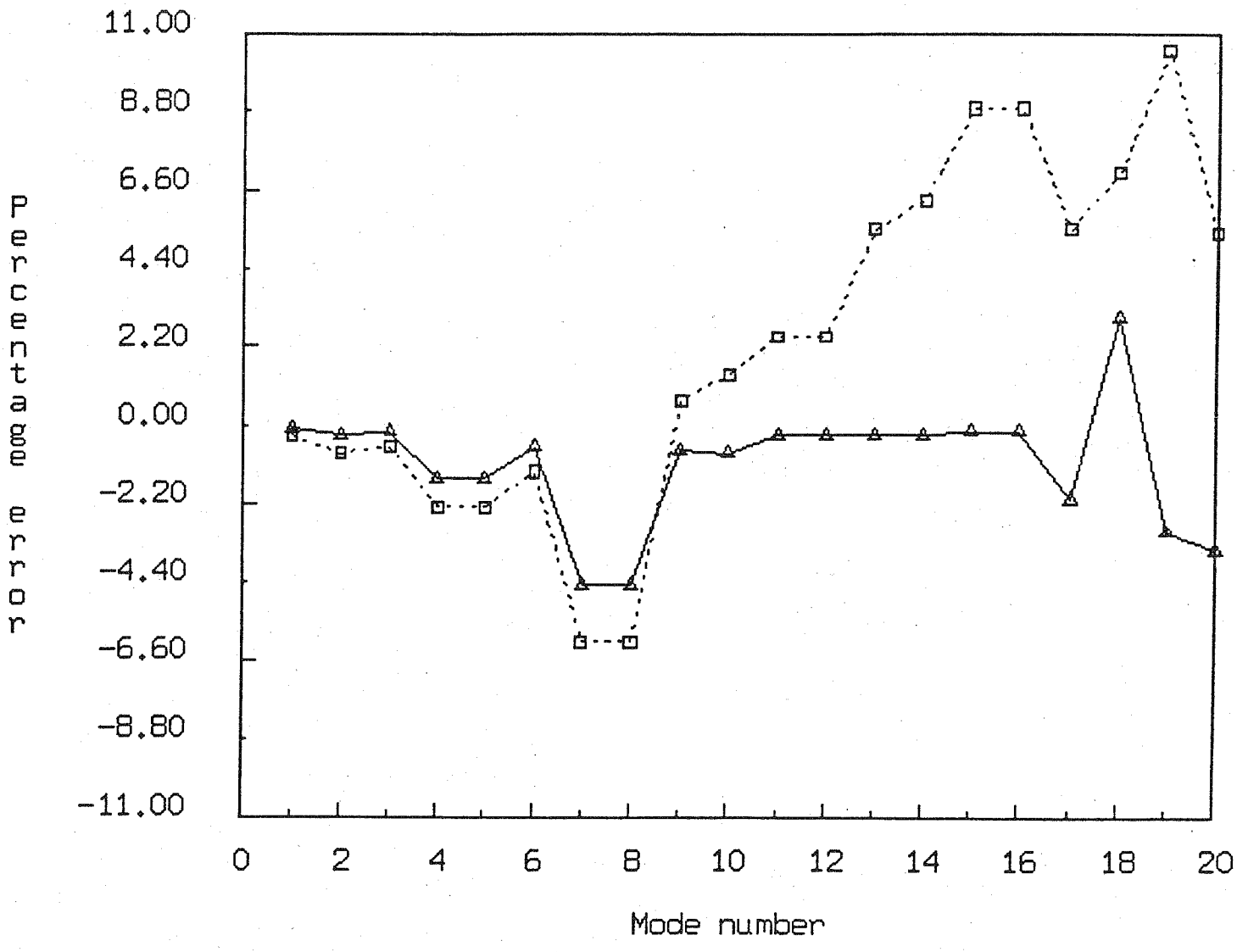

Figure 5.8. *Thin free square plate.* Relative error of the first 20 eigen-frequencies using 64-element (dotted line) and 256-element (solid line) meshes.

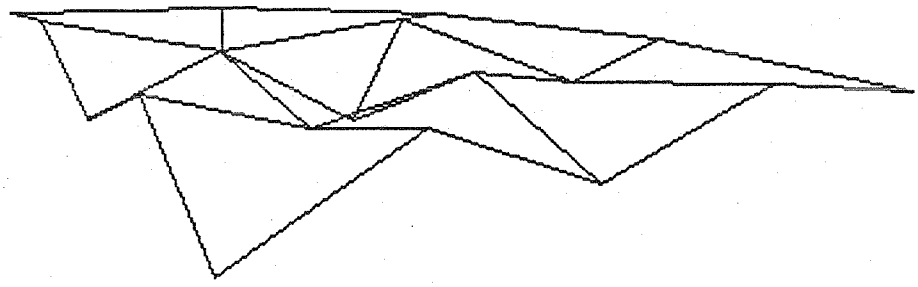

Figure 5.9. *Simply-supported thick circular plate.* Ninth mode: Spurious transverse displacement mode of type $\mathbf{z}_1$.

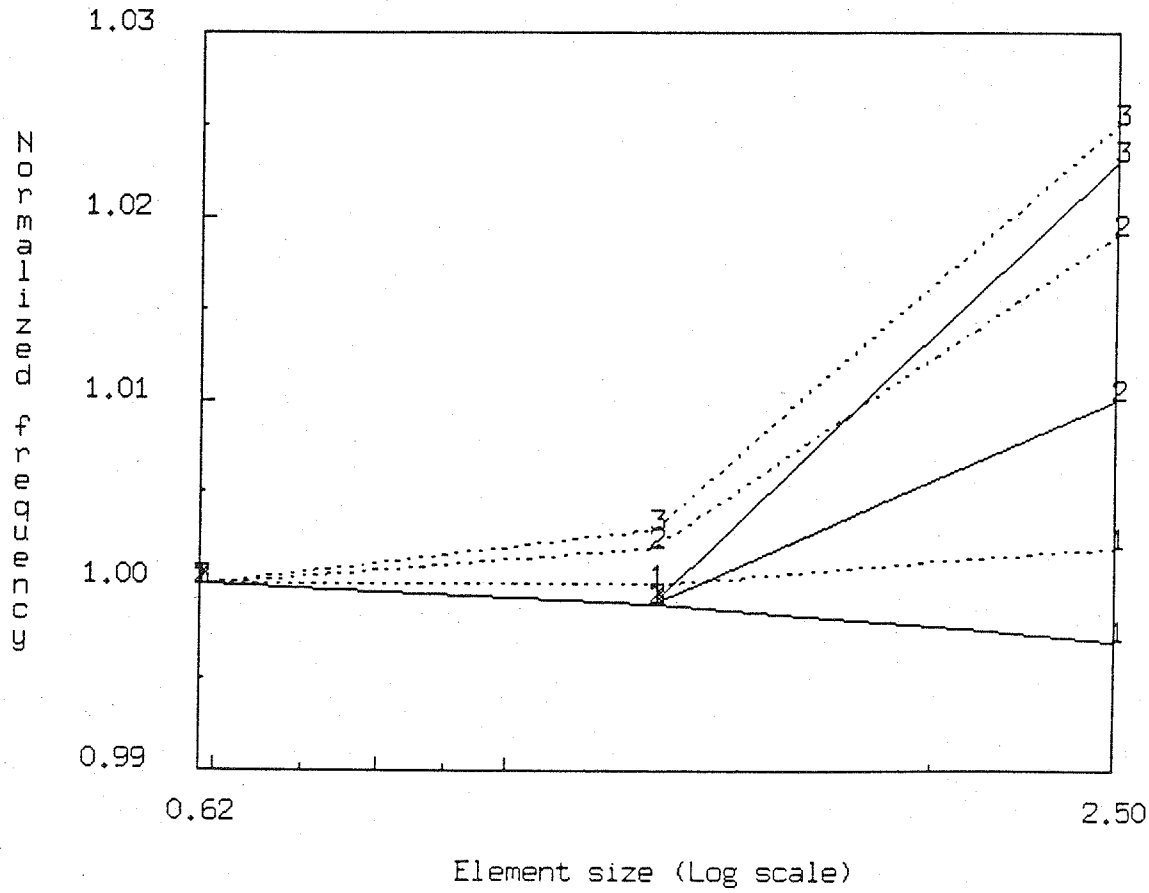

Figure 5.10. *Simply-supported thick circular plate.* Convergence of the first three eigen-frequencies. Solid line: Projected mass. Dotted line: Unprojected mass.

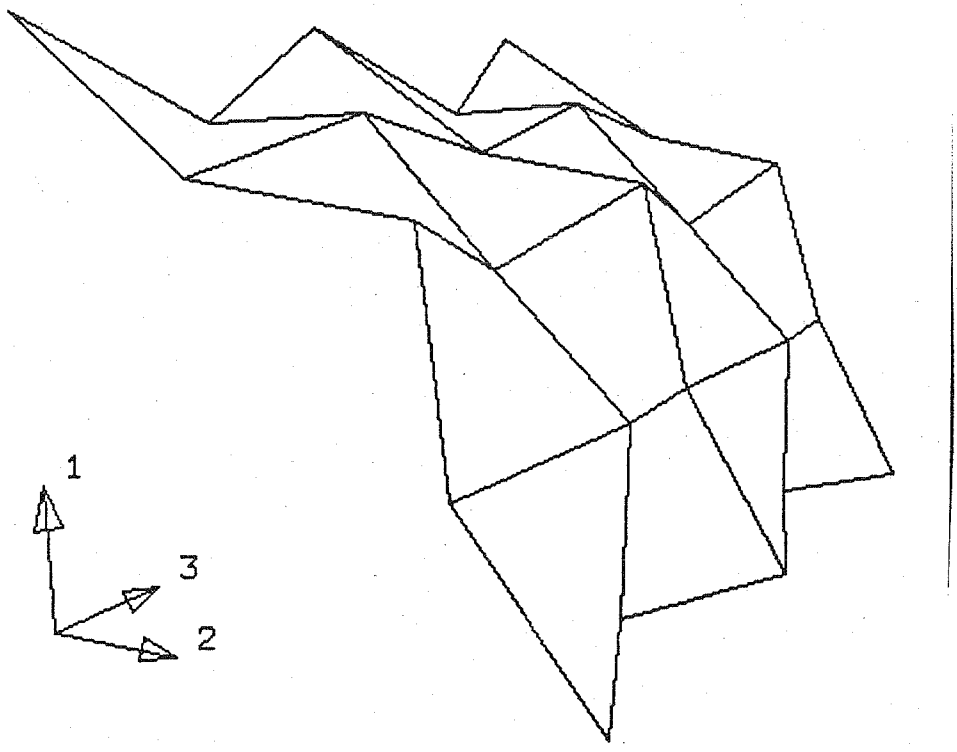

Figure 5.11a. *Cylindrical shell with free ends.* Mode 2: First spurious mode.

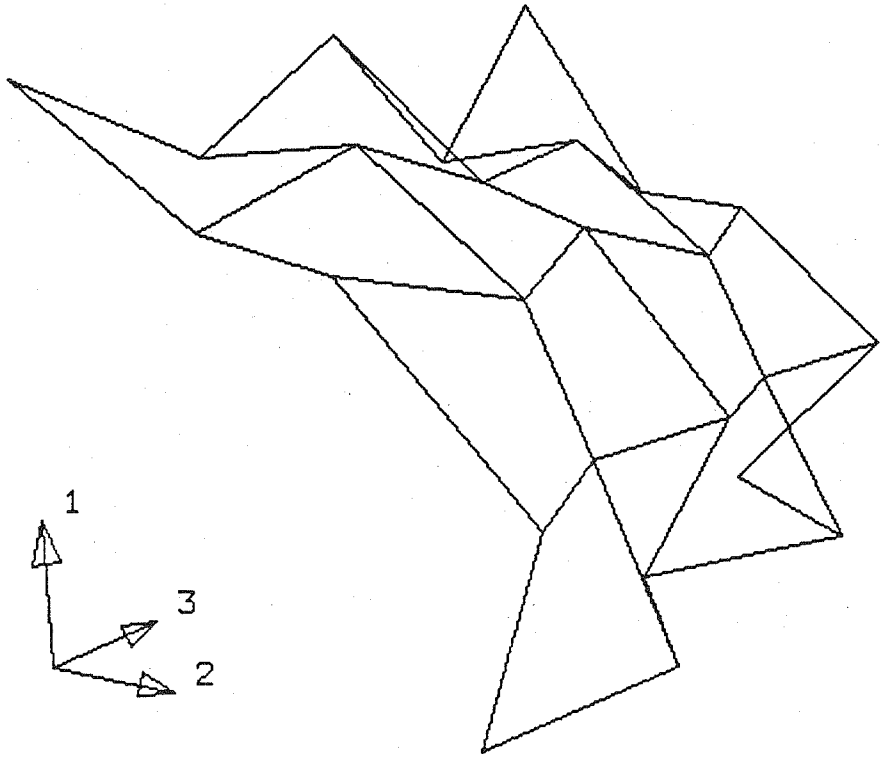

Figure 5.11b. *Cylindrical shell with free ends.* Mode 11: Second spurious mode.

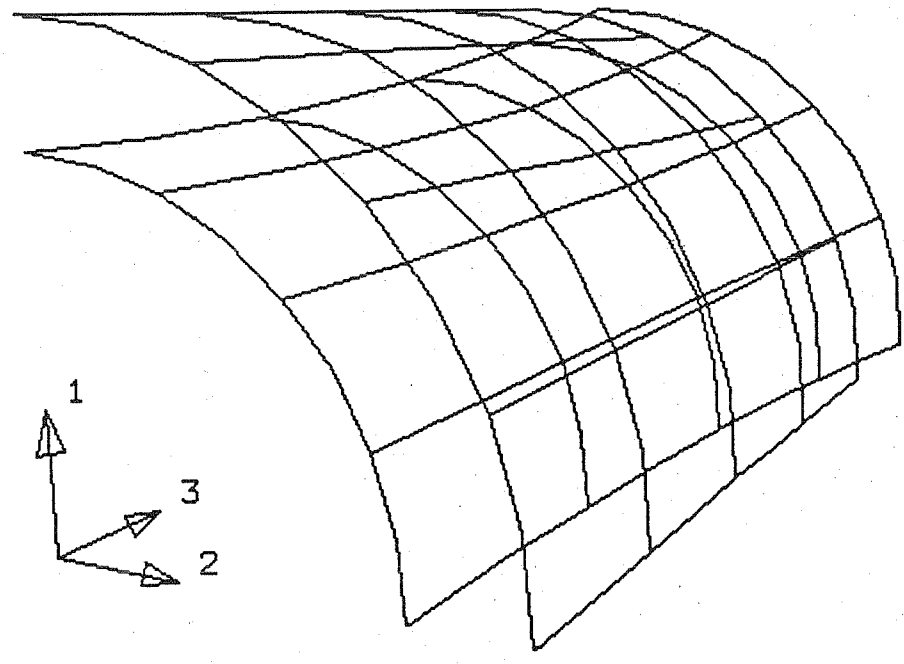

Figure 5.12a. *Cylindrical shell with rigid diaphragms.* Mode $(m, n) = (1,0)$.

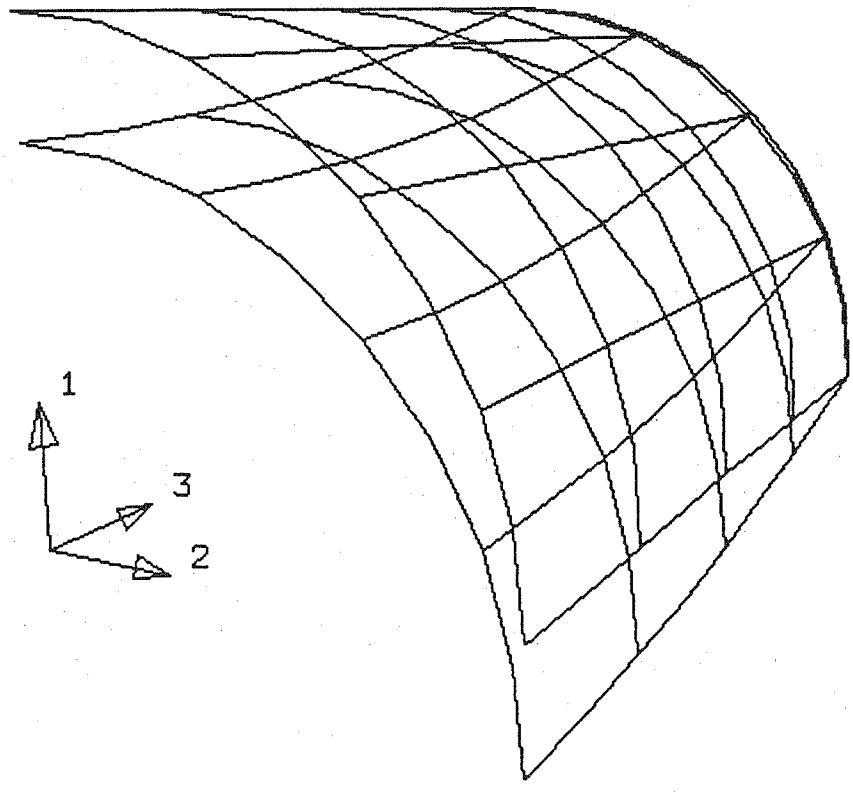

Figure 5.12b. *Cylindrical shell with rigid diaphragms.* Mode $(m, n) = (1,1)$.

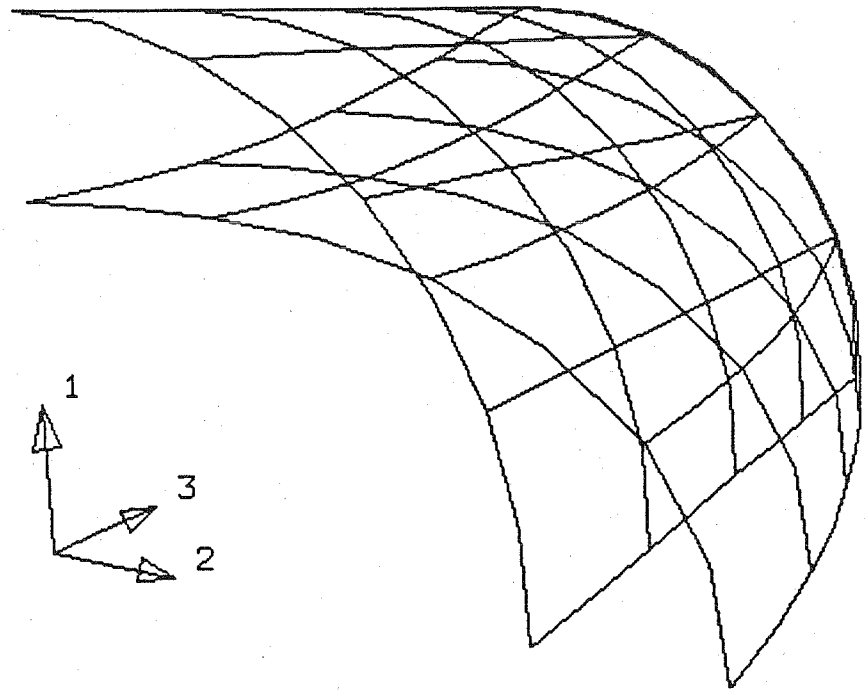

Figure 5.12c. *Cylindrical shell with rigid diaphragms.* Mode $(m, n) = (1,2)$.

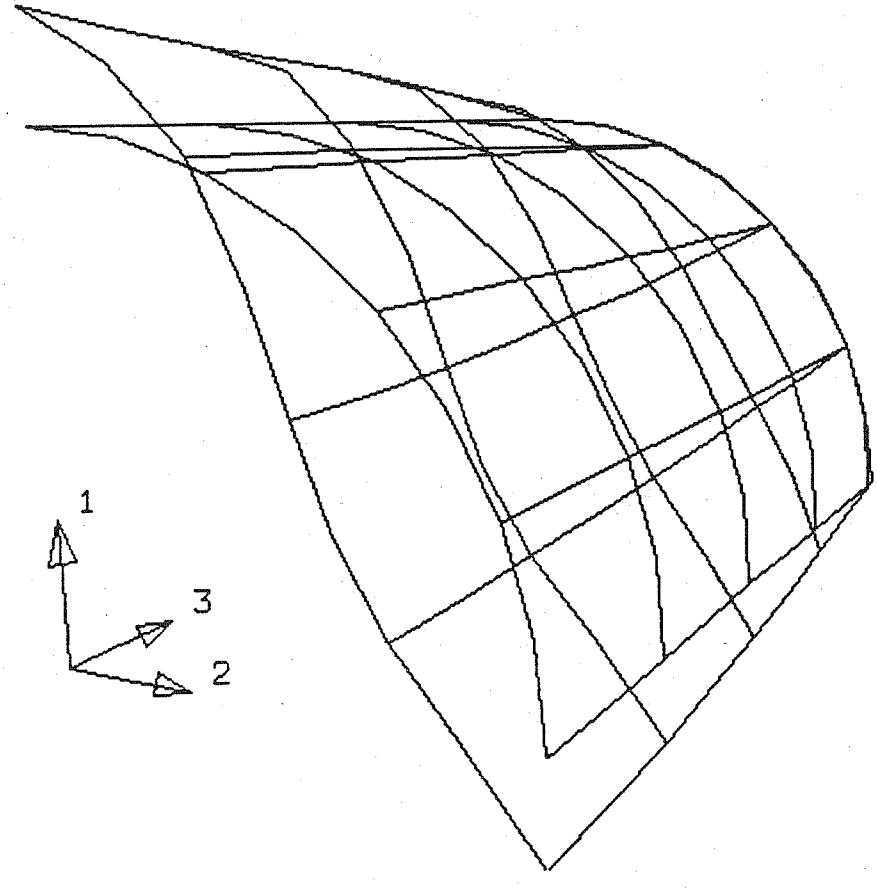

Figure 5.12d. *Cylindrical shell with rigid diaphragms.* Mode $(m, n) = (1,3)$.

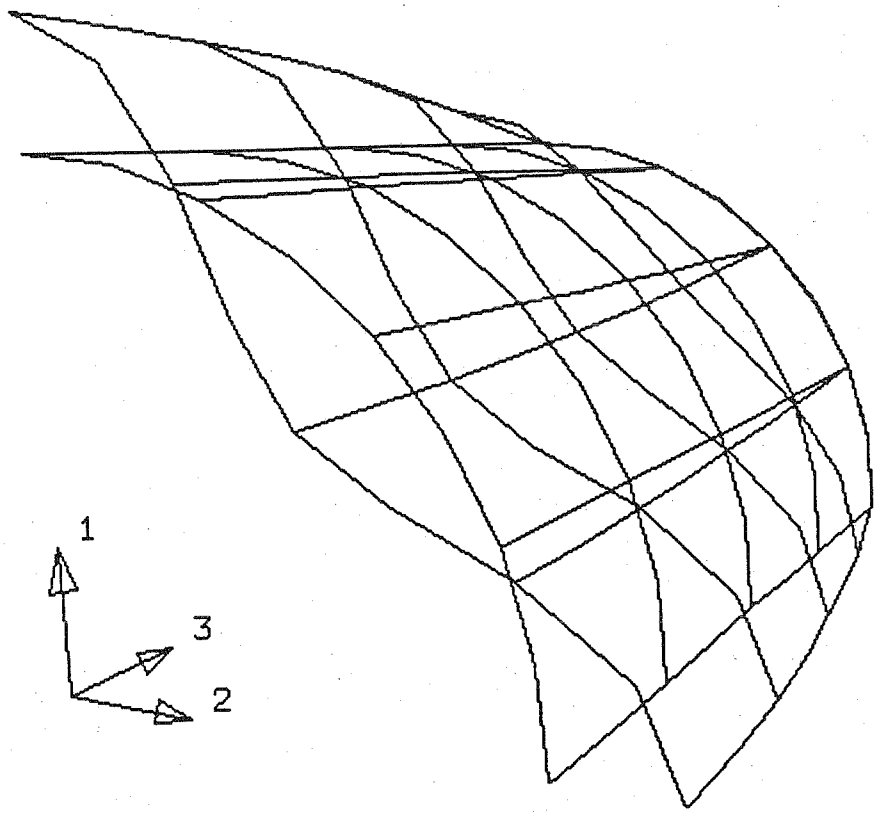

Figure 5.12e. *Cylindrical shell with rigid diaphragms.* Mode $(m, n) = (1,4)$.

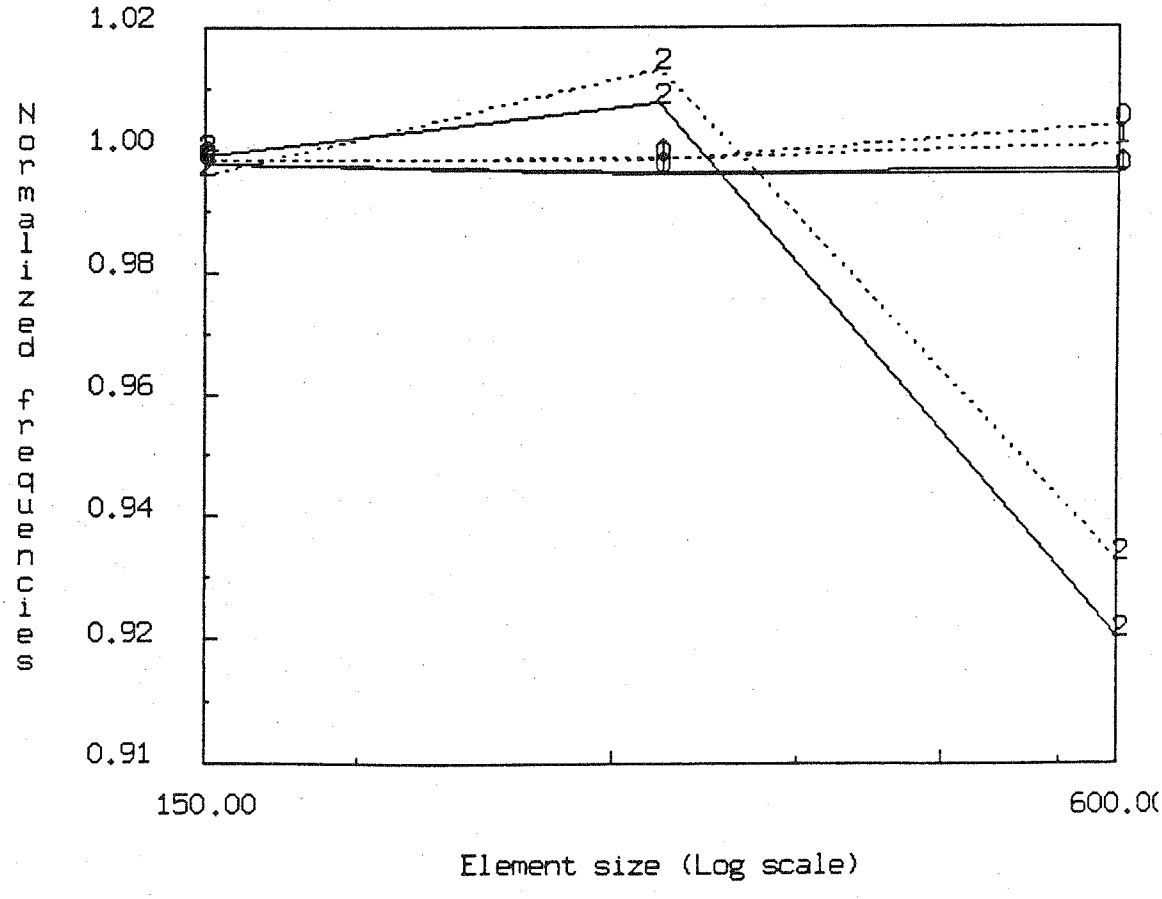

Figure 5.13a. *Cylindrical shell with rigid diaphragms.* Convergence of frequencies for modes $(m, n) = (1,0), (1,1), (1,2)$. Solid line: Projected mass. Dotted line: Unprojected mass.

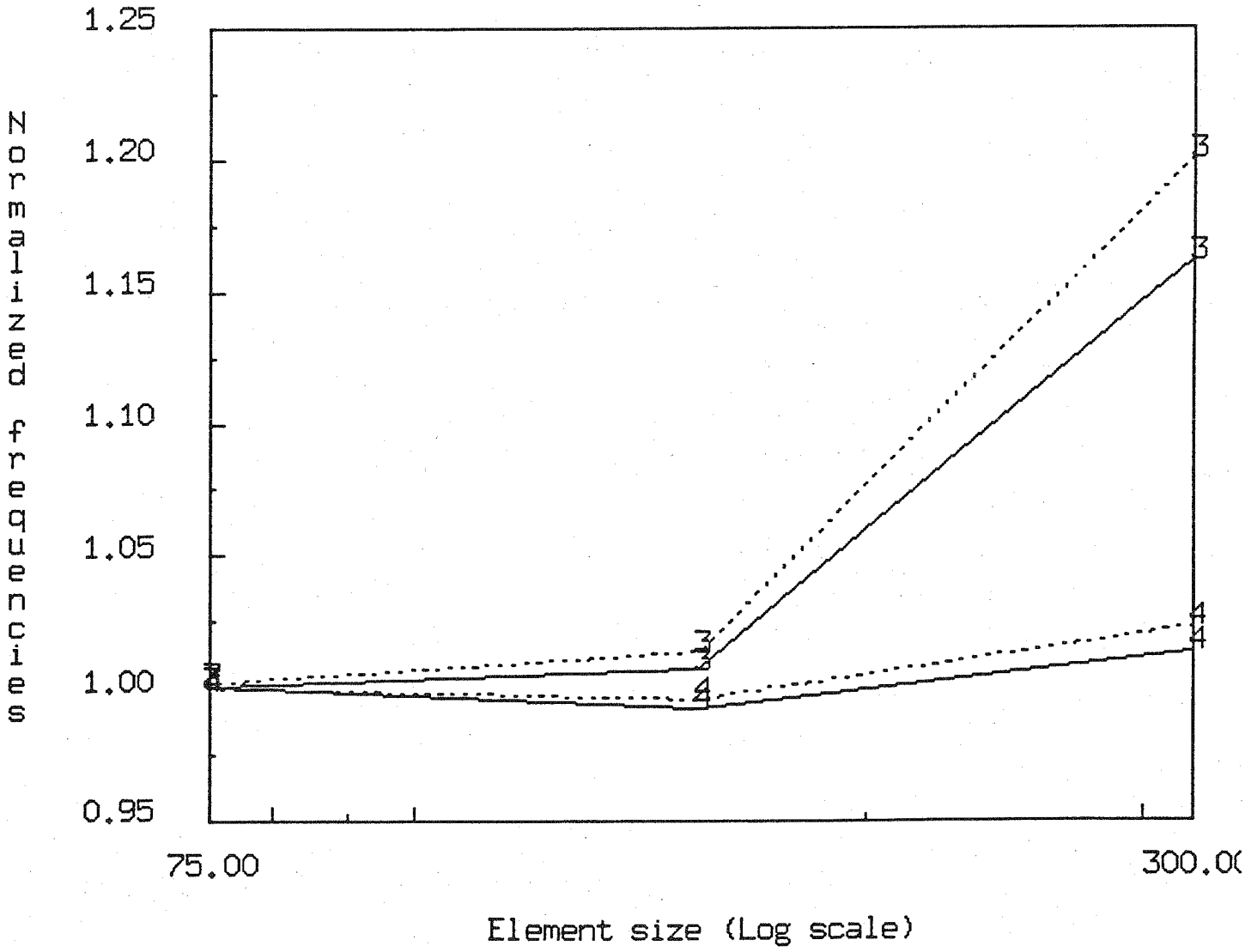

Figure 5.13b. *Cylindrical shell with rigid diaphragms.* Convergence of frequencies for modes $(m, n) = (1,3), (1,4)$. Solid line: Projected mass. Dotted line: Unprojected mass.